Mechanistic modeling for semi-solid redox flow batteries

Garima Shukla

Thèse de Doctorat

Mention Chimie
Spécialité Chimie Informatique et Théorique

présentée à *l'Ecole Doctorale en Sciences en Science Technologie et Santé (ED 585)*

de l'Université de Picardie Jules Verne

par

Garima SHUKLA

pour obtenir le grade de Docteur de l'Université de Picardie Jules Verne

Mechanistic Modeling for Semi-Solid Redox Flow Batteries

Soutenue le 10 Janvier 2020, après avis des rapporteurs, devant le jury d'examen :

M. Miran GABERSCEK, Professeur, NIC, Ljubljana	**Rapporteur**
M. Juraj KOSEK, Professeur, UCT, Prague	**Rapporteur**
M. Piotr DE SILVA, Assistant Professor, DTU, Lyngby	**Examinateur**
M. Emmanuel BAUDRIN, Professeur, UPJV, Amiens	**Examinateur**
M. Youcef MAMMERI, MCF, HDR, UPJV, Amiens	**Examinateur**
M^{me} Anne-Virginie SALSAC, DR CNRS, UTC Compiègne	**Co-directrice de thèse**
M. Alejandro A. FRANCO, Professeur, UPJV, Amiens	**Directeur de thèse**

à l'esprit d'examen,
prôné par les philosophes des Lumières

Publications

1. **Exploring Conductive Networks in Semi-Solid Redox Flow Batteries**, *Batteries Supercaps*, G. Shukla, O. X. Guerrero, A. A. Franco. (in preparation).

2. **Interphases in Electroactive Suspension Systems: Where Chemistry meets Mesoscale Physics**, *Batteries Supercaps*, 2019, *2* (7), 579–590. G. Shukla, A. A. Franco *(Invited Journal Cover)*.

3. **Handling Complexity of Semi-Solid Redox Flow Battery Operation Principles through Mechanistic Simulations**, *J. Phys. Chem. C*, 2018, 122(42), 23867. G. Shukla, A. A. Franco.

4. **Self-Organization of Electroactive Suspensions in Discharging Slurry Batteries: A Mesoscale Modeling Investigation**, *ACS Appl. Mater. Interfaces*, 2017, 9(21), 17882. G. Shukla, D. del Olmo Diaz, V. Thangavel, & A. A. Franco.

5. **Multiscale Simulation Platform Linking Lithium Ion Battery Electrode Fabrication Process with Performance at the Cell Level**, *J. Phys. Chem. Lett.*, 2017, 8(23), 5966. A. C. Ngandjong, A. Rucci, M. Maiza, G. Shukla, J. Vazquez-Arenas, & A. A. Franco.

Conferences

1. **A Kinetic Monte Carlo Framework for a Discrete Multiphysics description of Semi-Solid Redox Flow Batteries**. *15th Symposium on Modeling and Experimental Validation of Electrochemical Energy Devices (ModVal 2018), Aarau, Switzerland.* In Meeting Abstracts (pp 42). 12-13 April **2018**. G. Shukla, O. X. Guerrero-Gutierrez, M. H., Y. Mammeri, A. Salsac, A. A. Franco.

2. **Modeling Slurry Electrodes for Redox Flow Batteries Using Kinetic Monte Carlo**. *The 231st Electrochemical Society Meeting, New Orleans, United States.* In Meeting Abstracts (No. 2, pp. 173). 28 May-1 June **2017**. G. Shukla, A. A. Franco, D. del Olmo Diaz, V. Thangavel.

3. **Multiscale Computation Approaches for the Simulation of Battery Electrodes Fabrication**. *The 229nd Electrochemical Society Meeting, San Diego, United States.* In Meeting Abstracts (No. 4, pp. 414). 29 May-2 June **2016**. A. A. Franco, G. Shukla, M. Morcrette, S. Cavalaglio.

BATTERIES & SUPERCAPS

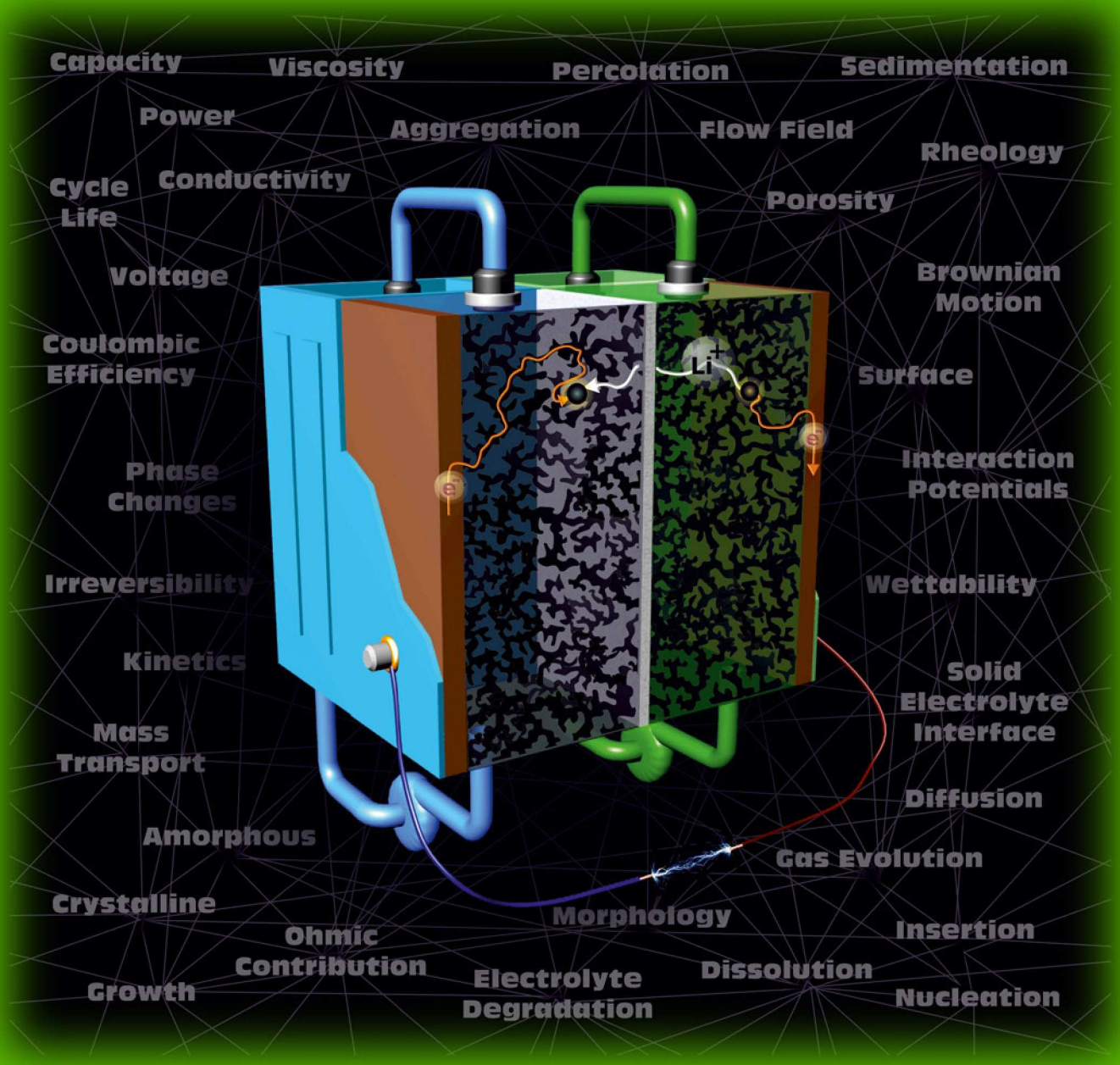

7/2019

The journal for ELECTROCHEMICAL ENERGY STORAGE

Front Cover:
G. Shukla and A. A. Franco
Interphases in Electroactive Suspension Systems: Where Chemistry Meets Mesoscale Physics

A Journal of ChemPubSoc Europe

WILEY-VCH www.batteries-supercaps.org

Acknowledgements

The most marvelous discovery I made during my PhD was how the personal experiences from my past shaped the lens through which I saw the scientific world and how learning to conduct scientific research changed me into the person I most wanted to become. This research work took many unconventional turns, crossed several disciplinary boundaries, and when I felt truly lost, an anecdote from P. Frank's book on Einstein's Philosophy of Science, came to the rescue: *"Another day we spoke about a certain physicist who had very little success in his research work. Mostly he attacked problems which offered tremendous difficulties. He applied penetrating analysis and succeeded only in discovering more and more difficulties. By most of his colleagues he was not very highly rated. Einstein, however, said about him, 'I admire this type of man. I have little patience with scientists who take a board of wood, look for its thinnest part and drill a great number of holes where drilling is easy.' Through all his life as a physicist Einstein has regarded his own work as a search for the general laws of nature and as closely related to the work of the philosopher."*

Prof. Alejandro A. Franco, for teaching us to dream in science, supporting our new ideas, and for being both mentor and trusted friend.

Prof. Anne-Virginie Salsac, for the encouragement, guidance, and for being an inspiring female scientist role model.

To the Region Hauts-de-France and FEDER for the financial support to the Project WONDERFUL (Wise OptimizatioN and Deep Enhancement of Redox Flow batteries through ULtimate modeling).

Dr. Matias Quiroga, Diego del Olmo Diaz, Oscar Xavier Guerrero, and Vigneshwaran Thangavel for helping build a marvelous Python code from scratch. Kush Chadha and Marouan Handa for joining the adventure to explore new avenues.

Various members of LRCS who helped with performing experiments: Dr. Emiliano Primo, Dr. Arnaud Demortiere, Prof. Dominique Larcher, Yih Chyng, and Christine Surcin. Several other who contributed through many useful discussions: Dr. Charles Delacourt, Dr. Emmanuel Baudrin, Dr. Gregory Gachot, Theodosios Famprikis, Dr. Alain Ngandjong, Ulas Kudu, Teo Lombardo, and Dr. Amina Touidjine. To the administrative staff who made everything possible: Carine Lenfant, Nathalie Saulnier, Anne Charbonnier, Daphné Boursier, and Audrey Lecompte. To Prof. Christian Masquelier and Dr. Mathieu Morcrette, without whom I would not have been a part of the LRCS family.

To those who offered emotional support, my darling Shekhar Mishra, Iryna Sagaidak, Mukta Shukla, Rakesh Shukla, Udit Shukla, Kusum Shukla, Lata Mishra, Atul Mishra, Dr. Yinghui Yin, Dr. Amangeldi Torayev, Nour Daher, Ana-Cristina Martinez Maciel, Laura Cristina Loaiza Rodriguez, Zeliang Su, Tristan Lombard, Francois Rabuel, Mariana Gutierrez, Chance Norris, Waad Naim, Noura Rahbani, and most importantly, Jacquie Dorn.

Overview

Table of Contents

Introductory Summary

This thesis study is based on the recently developed semi-solid redox flow battery (SSRFB). It can simultaneously interest researchers in the field of redox flow batteries (RFBs) as well as lithium ion batteries (LIBs), since the SSRFBs represent a union of RFBs and LIBs. The SSRFB can be visualized as essentially a flowable LIB electrode within the architecture of a RFB.

The model proposed studies particle suspension dynamics undergoing electrochemical phenomena from a mechanistic perspective. It was developed in-house in Python from scratch and it is described in Chapter 3. Insights on the method are provided in Chapter 4 and a case study to show it capabilities in providing physically relevant insight is provided in Chapter 5.

The methodology proposed herein incorporates a wide variety of modeling tools from various disciplines. It is an agent-based model with a kinetic Monte Carlo engine, in a three-dimensional discrete space. The physics simulated has a significantly well-defined causal flow, which can further be elaborated upon using graph theory. Object oriented programming helps simulate evolution of properties of individual particles as they interact with one another during electrochemical discharge.

The highly interconnected causal flow provides a holistic picture of the SSRFB, which comes with many checks and balances to handle differences in assumptions of various empirical equations used. Thus, this self-correcting and adaptive approach provides a systematic means to test a variety of hypotheses in a rigorous way.

A large amount of data is generated to perform local and global parameter sensitivity analyses, to identity parameters that are sensitive and important. This helps to standardize the model, a step which is known to be very challenging for all mechanistic models. It also helps perform studies where multiple parameters are simultaneously varied, something that is essential but very difficult to achieve experimentally. Simulating at the mesoscopic scale

further provides insights that are experimental difficult to capture and that traditional continuum models tend to miss. It provides a means to identify new kinds of metrics which can be instrumental in directing research to obtain optimization faster.

Furthermore, this study provides quantitative means to demonstrate how SSRFBs are a complex system. In parallel, this work elaborates the nature of complexity itself in the context of materials for energy storage. Further discussions place existing modeling and experimental tools in the perspective of how they can aid or hinder the study of complexity of the SSRFB.

A description of the context (Chapter 1), state of the art (Chapter 2) and complexity (Chapter 6) demonstrates how the journey to commercialization of the SSRFB will require significant collaborative effort from not only the RFB and LIB communities, but will also need the involvement of experts of rheology, particle level mechanics. The SSRFB demands a new approach to experimental studies, since traditional studies used for LIBs, RFBs, rheology or imaging, do not provide enough information. New methods that simultaneously measure multiple types of outputs are essential, however a huge challenge lies in establishing such methods because their optimization is further based on such complex systems which are difficult to study.

In conclusion, this work provides proof of concept of a work-flow for new genre of methodologies that are focused on integrating complex system intricacies with maximum transparency. The novelty of this work lies in viewing electrochemical systems through the lens of complex system studies. This helps provide exhaustive justifications for why systematic research and advancement in disciplines like SSRFBs and LIBs is incredibly challenging. It also aims to provide a perspective with which conflicting scientific discoveries and long standing debates can be resolved and put to rest.

Chapter 1

Introduction

1.1. Need for Battery Innovation

Any technological change in society is contingent on short term economic advantages which tend to dictate market trends, and inevitably have political and social impacts. A 2019 global risk report by the world economic forum provides a thoroughly comprehensive look at critical forces that will influence the human race in the years to come.[1] The study includes economic, technological, societal, geopolitical, and environmental risks which are highlighted in Figure 1.1. The interconnectedness of factors and interactions between forces in this schematic makes it difficult to collect data to provide predictions for clear decision making. Most technological changes in such an interdependent system have a potential to become *disruptive* for society, for better or for worse, and the energy sector would be no exception. With climate change mitigation policies demanding cleaner energy sources; renewable energy storage coupled with tailor-made energy storage devices are expected to cater to the market needs as fast as possible. The Kyoto Protocol of 2005, targeted to counter climate change causing emissions, was unable to bring about significant transformation in industry.[2] Consequent climate talks have not been particularly successful in reaching global consensus, *i.e.* the 15th COP (Conference of Parties) in Copenhagen in 2009 was a significant failure, the effects of which spilled over to COPs in Cancun in 2010 and Durban in 2011.[3] Consequently, there has been a call for a more stringent and integrated approach to climate change policies and the introduction of *polycentric climate governance* so that local factors can be taken into account, building solutions that may be more complex but significantly more beneficial.[4,5]

To make policy implementation easier, the technology transition has to be made smooth at multiple levels and requires coordinated efforts for innovation, planning, and deployment.[4] Innovation, in terms of an invention or discovery that can be turned into a marketable prototype, is most relevant for laboratory scale research and will be addressed in this work. It can thus be very useful to look into the dynamics of innovation. *Patent citation networks*, for instance, can show how a collection of different inventions can lead to new ideas and patents.[6]

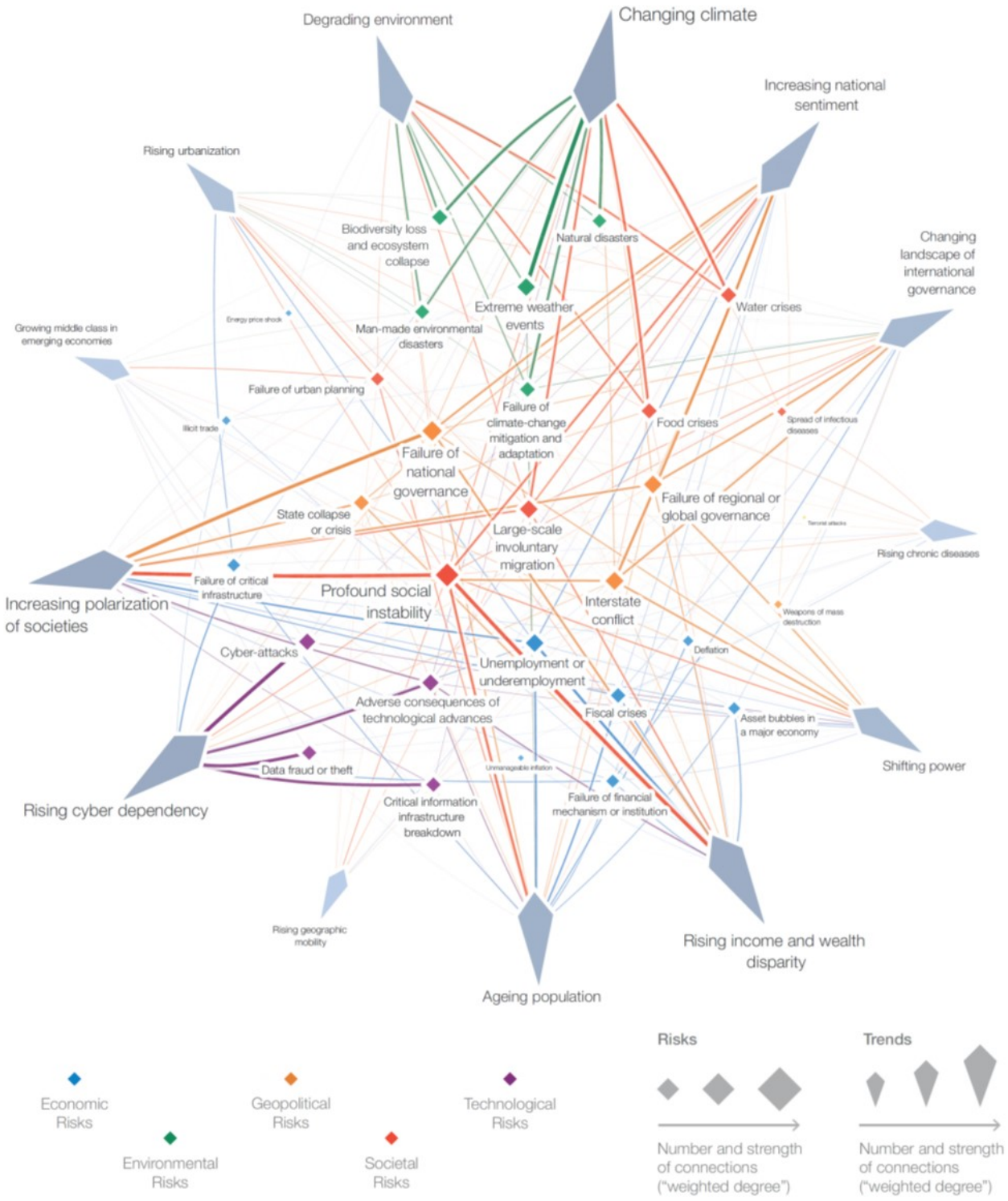

Figure 1.1: Global risk report for 2019 by World Economic Forum showing importance of various risks and their dependence on each other.[1]

It has been reported that an important driver of innovation is *technological diversification* and in turn innovation produces more diversification.[7–9] The United Nation Framework Convention on Climate Change reports that technological diversification is even expected to build resilience in terms of both energy and economy.[10] However, when a new technology interacts with industry, the changes tend to lead to technological turbulence.[11] This phenomenon has been recently studied in the context of photovoltaic technology. It was demonstrated that in research and development (R&D), both collaboration and technological diversity can combat the negative impacts of technological turbulence.[12] Under the right conditions, collaborative R&D that promotes exchange of knowledge and understanding of diverse technologies stimulates innovation for both applied industrial and fundamental public research.[8,13,14] This shows how intra-disciplinary and cross-disciplinary knowledge and knowhow are a critical aid for innovation and commercialization of a new technology. A big challenge, however, lies in creating and managing cross-disciplinary information exchange and is thus the general context for the thesis.

1.2. Technological Diversification in Battery Technology

The first battery was put together by Volta two centuries ago,[15] and large scale initiatives such as the Materials Project have predicted chemistry of 4401 intercalation electrodes and 16128 conversion electrodes.[16] Yet less than two dozen batteries are commercially available today, including both primary and secondary type. Even though intuitively expected, diversification at a lower level, *i.e.* the material level, does not automatically produce a diversity of usable battery systems. Thus a bottom-up approach to build a battery with certain *target characteristics*, like energy density and power, may not be practical. However, once a combination of electrode materials shows some potential to form a new type of battery, finding the right application for it is essential in determining whether it will be optimized as a device and reach commercialization.

RFBs, which were described has suitably generic systems to study in the previous section, generally cater to grid support to manage load shifting and to buffer intermittency of solar energy. A device for such an application

should typically provide 100 kW-10 MW. Other types of devices, as shown in Figure 1.2, can be classified into applications based on discharge time at rated power as follows:

(i) Discharge times of seconds is offered by devices like high power flywheels, high power supercapacitors, and superconducting magnetic energy storage.

(ii) Discharge time of minutes is provided by a majority of batteries, for instance, lithium ion batteries (LIBs), lead acid batteries, and high energy supercapacitors.

(iii) Discharge time of hours can be achieved with molten salt or redox flow batteries (RFBs)[17]. While pumped hydro and compressed air energy storage represent a substantial capital investment, they are used primarily for bulk power management.

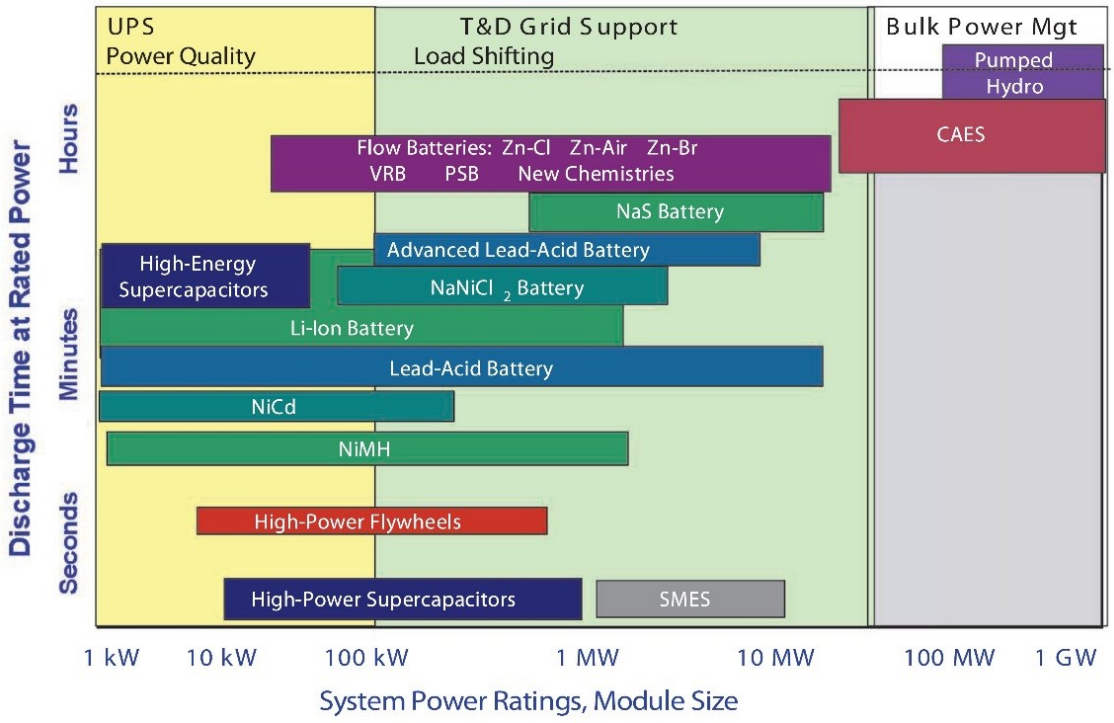

Figure 1.2. Power and energy ratings of various technologies for different applications.[18]

From a general perspective, electrochemical devices offer significant potential for diversification in terms of functionality, redox chemistry, and physical properties of materials used. Additionally, as highlighted in

Figure 1.3,[19] RFBs can offer high functional diversity amidst electrochemical devices because they can potentially revert to other devices under reduced conditions. Therefore, studying and understanding phenomena in RFBs can provide fundamental insight for its optimization and also give relevant guidelines for studying related devices.

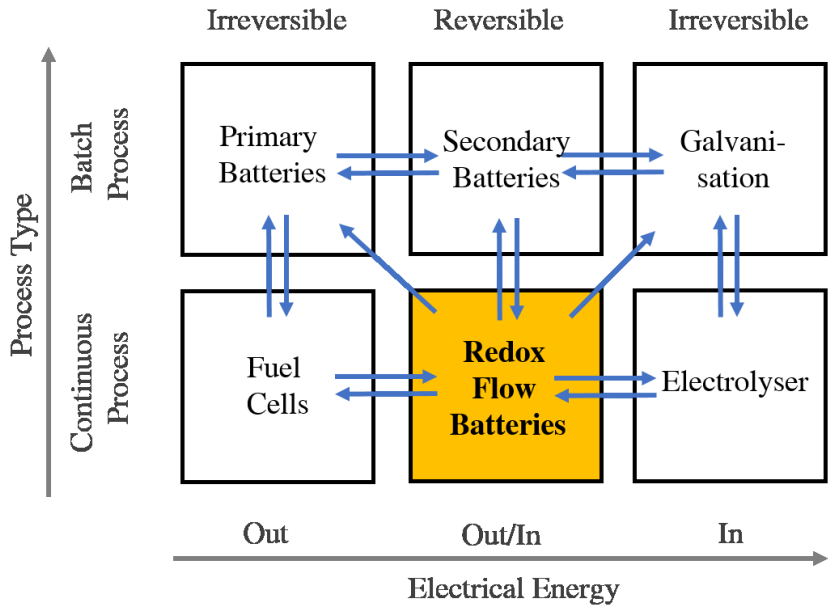

Figure 1.3. Functional adaptability of diverse electrochemical devices.[19]

RFBs advantageously allow a flowable liquid containing active material and electrolyte, much like a fuel, can be stored in a large, external tank and pumped into the discharging battery unit when needed. The size of the tank determines the energy density and the architecture of the battery unit defines the power density the device can deliver. This makes RFBs ideal for building highly customizable grid storage solutions. This work is focused on a new family of RFBs, namely, semi-solid redox flow batteries (SSRFBs). The novelty of the SSRFBs lies in the multiphase electrode, wherein an electrolyte acts as a medium in which two kinds of solid particles are suspended, namely (i) electron conducting material and (ii) lithium storing electroactive material.[20] Since SSRFB technology is derived from a combination of both LIBs and RFBs, it represents a perfect example of how innovation can result from technological diversification (Figure 1.4).

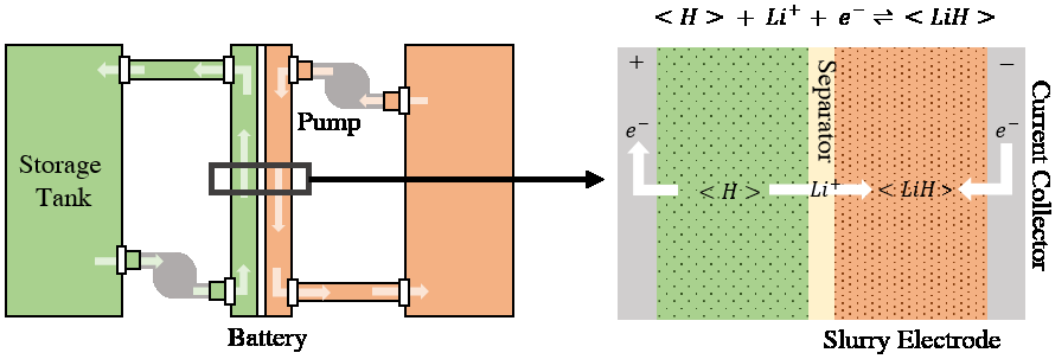

Figure 1.4. Schematic showing set-up of the flow system (left) with the battery unit (right)

The concept of SSRFBs opened doors for a bounty of design possibilities at the level of redox chemistry, multiphase electrode, and cell architecture. This subject has been addressed in some reviews[21–23] and the last ten years show diverse upcoming technologies like flow capacitors,[24–33] water desalination,[24,34–36] incorporation of redox mediators,[37–45] carbon-free suspensions,[46,47] polysulfide or metal-ion based carbon suspensions,[48–58] and semi-solid metal-air flow batteries.[59–61] The birth of the SSRFB and its interaction with other technologies, as reported in literature, at varying levels of system development, are represented pictorially as a *technological trajectory* in Figure 1.5. The red arrows point to *emergent technologies* that are said to *emerge* from interactions between two technologies. This schematic highlights the impact that technological diversification has on innovation and how inventions can be advantageous regardless of their developmental status.

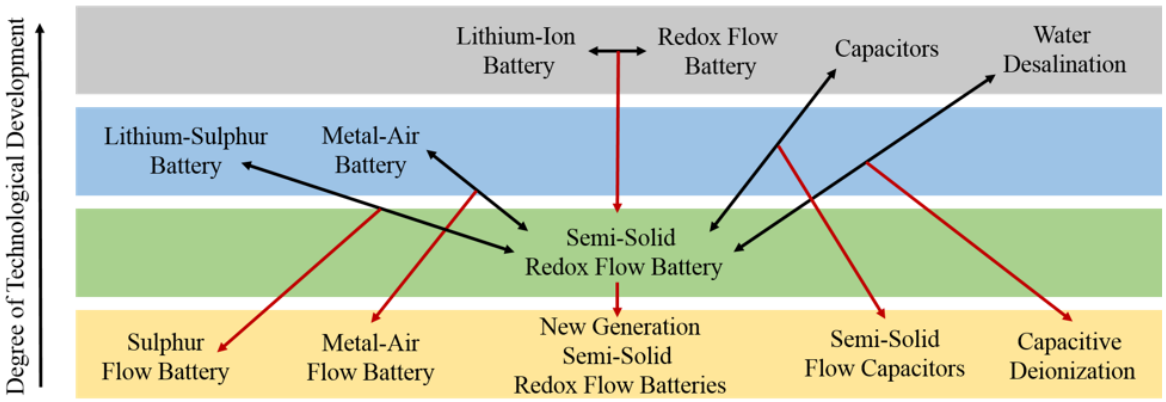

Figure 1.5. Schematic representation of technological trajectory of SSRFBs.

While moving from one breakthrough to another may be beneficial to acquire research grants, leaving questions unanswered along such a trajectory eventually becomes a hurdle for commercializing any emergent technology. For instance, within 10 years of the introduction of SSRFBs, its commercial value already appears to be dwindling and only in the last few months has there has been one report of a market-ready prototype by 24M in Cambridge.

Historically, new electrochemical technologies have taken up to half a century to reach commercialization. For instance, optimizing the process for electrolysis of salt water took 60 years' worth of intuition and trial-and-error, along with knowhow accumulated from similar studies in other equally developed fields like electrolysis and metallurgy.[62] This was achieved without any deep understanding of fundamental phenomena that drive performance.[62] Since the electrochemistry in the SSRFB is derived from batteries, a brief look at their development is worthwhile. Between invention and commercialization, lead acid batteries took up to 70 years and Nickel-Cadmium (Ni-Cd) batteries needed 60 years.[63] Around the time the latter was commercialized, metal alloys that could absorb hydrogen were being studied and it took another 40 years for a Nickel Metal Hydride battery to appear on the market.[64] High reversibility of these devices was easier to achieve since the dominant mechanisms and phenomena involved ion migration and electrodeposition. In hindsight, this appears less complex when compared to the interfacial phenomena that takes place in LIBs. Since none of the older battery technologies come close to the tailoring potential and diverse applicability that LIBs offer, LIBs occupy a huge research interest.

The capability to have more parameters to tune, however, brings a high degree of complexity to LIBs and this is best shown by the history of this technology. The discovery of lithium metal in 1817 was immediately associated with electrochemical activity, however its high electromotive force was noticed only a 100 years later.[15] The discipline of electrodeposition, used to obtain pure lithium, was instrumental for research behind finding suitable electrolytes for LIBs, however after the first studies in 1897,[65] the method took 60 years to perfect.[66] Another big hurdle was finding a suitable anode, because even though the first evidence of intercalation of cations into graphite was obtained in 1904,[67] it was only 86 years later, in 1990, that electrolyte degradation could passivate

the graphite surface to form a solid electrolyte interface (SEI) and intercalation could proceed without gassing and exfoliation.[68] It is fascinating to note that companies looking to manufacture batteries were searching for new types of carbons, while the solution lay in simply fine tuning electrochemical phenomena at the electrolyte-graphite interface. It is claimed that scientists continued to use propylene carbonate for decades based on the assumption that ethylene carbonate would behave similarly; this simple misconception is known to have delayed the successful intercalation of graphite by lithium ion and consequently commercialization of the LIB by about a staggering 20 years.[15] Today, while the types of materials and battery architectures under research have exploded in number, a new working battery is still referred to as an accidental or serendipitous discovery because phenomena inside a battery can still emerge unexpectedly.[15]

1.3. Conclusions

This chapter highlights the need for technological diversification as a means to ensure an economically and energetically stable future. SSRFBs, invented in the last decade, provide an excellent study of how diversification results in emergent technologies. SSRFBs not only provide a basis for the invention of newer technologies, they also show how the nature of parent technologies, RFBs and LIBs, manifest. This can provide new insight not only for RFBs and LIBs, but for all devices related to both the parent devices and the emergent device. The high potential for fundamental insight however is marred by the lack of a unifying platform on which to place existing state of the art to reveal gaps in knowledge so that there is context for any new information. As reflected in the history of the LIB, if the future lies in building technologies with high potential for adaptability and tailoring, the challenge is to find the optimal conditions for sustained functioning; this can be like looking for a needle in a haystack since such devices tend to show strong parallels to complex systems. The following chapters are aimed at discovering and elaborating the nature of this complexity and what kind of tools can be helpful.

Chapter 2

State of the Art

2.1. Invention of the SSRFB

The semi-solid redox flow battery (SSRFB) is essentially a flowable lithium-ion battery. It was first patented in 2009 by Chiang *et al*.[69] As previously mentioned, it is a combination of the Redox Flow Battery (RFB) technology and Lithium Ion Battery (LIB). RFBs typically have ionic solutions soaked carbon foams as electrodes, these solutions can be stored in external tanks, thus enabling grid scale energy storage. LIBs have solid electrodes soaked in electrolyte and are typically used for portable applications. Although it is possible to use numerous LIB units for create large scale stationary applications. The SSRFB basically contains the same material as the LIB but with modified composition so as to function like a RFB. The mechanism of electrochemical reactions in the slurry electrode of the SSRFB is depicted in Figure 2.1.

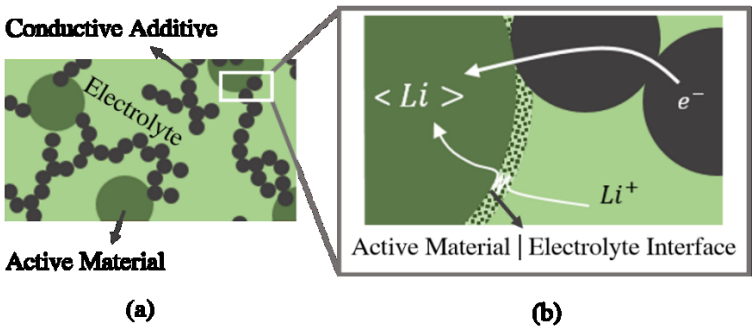

Figure 2.1. (a) Mesoscopic picture of particle suspension (b) Phenomena occurring during discharge..

As previously mentioned, the multiphase electrode contains two types of solid particles suspended in electrolyte: (i) an electron conductive additive, and (ii) active material responsible for storing energy.[20] When compared to ionic solutions of RFBs, SSRFBs can accommodate a higher concentration of solid active material in the same volume, resulting in potentially 5-20 times greater volumetric energy density.[20] Since the materials used for SSRFBs are taken from LIBs that are already known to function well, the main challenges lie with tuning phenomena to obtain a well-functioning SSRFB. Discussions linked to thermodynamic capabilities of materials used are, therefore, out of context of this work but the proposed paradigm is expected to take them into account in the future.

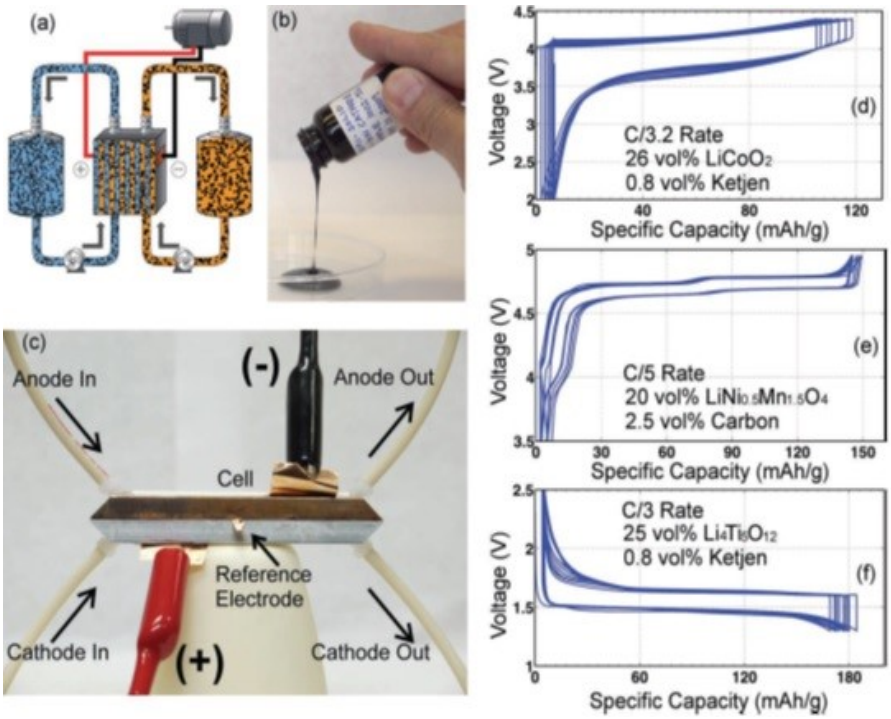

Figure 2.2. Taken from Duduta et al.[20] (a) Schematic of flow cell (b) Typical viscosity of slurry, (c) Flow cell with lithium metal as reference electrode, (d–f) Galvanostatic charge/discharge curves.

The first publication on SSRFBs in 2011[69] was based on the patent by Chiang *et al.*[20] in 2009 and contained sufficiently generalized observations from an industrial point of view. This study reports slurries based on: (i) different alkyl carbonate solvents containing $LiPF_6$ salt, (ii) active materials like $LiCoO_2$, $LiFePO_4$, $LiNi_{0.5}Mn_{1.5}O_4$, and graphite, and (iii) carbon-based conductive additives like Ketjen Black (KB). The electrochemical tendencies of these slurry electrodes have much in common with LIB electrodes fabricated with the same materials. Electronic conductivity of the conductive additive was shown to be a limiting factor. Further rheological investigation showed presence of shear thinning behavior and this suggested that electronic conductivity arises from networks of conductive additive particles and could thus be tailored (Figure 2.3). Additionally, different flow conditions like continuous and intermittent (*i.e.* stop-discharge-and-go) flows were studied. Intermittent flow showed less parasitic losses and it was suggested that round trip efficiencies could be improved by tuning flow rates.[20]

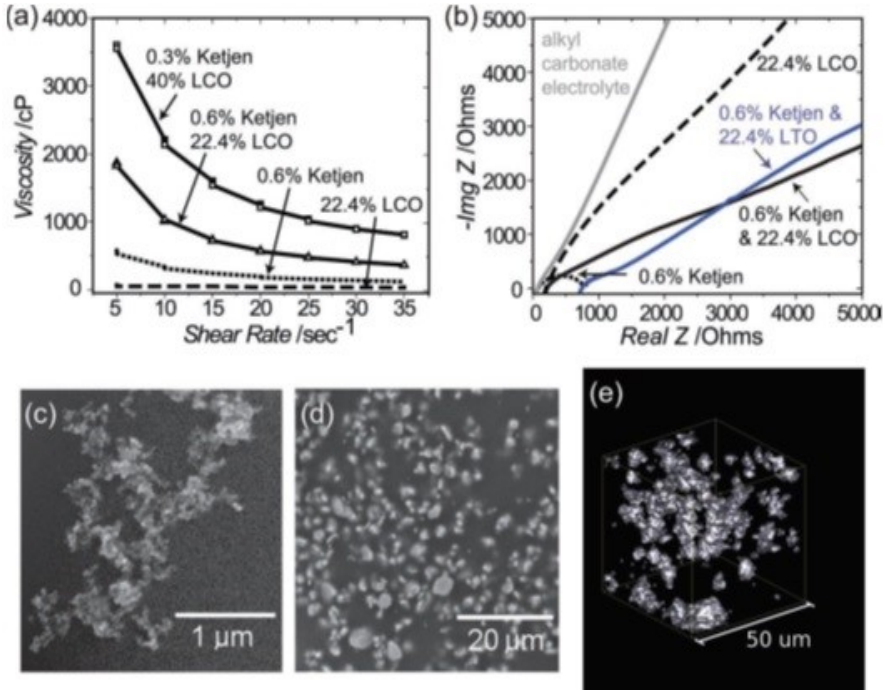

Figure 2.3. Taken from Duduta et al.[20] (a) Viscosity versus shear rate for suspensions for Ketjen black and $LiCoO_2$ (LCO) in alkyl carbonate electrolyte. (b) Nyquist plots for the different suspensions and their components (c) Wet-cell SEM images of Ketjen black in alkyl carbonate electrolyte, (d) a suspension of 22.4 vol% LCO and 0.6 vol% Ketjen in electrolyte (e) a 3D reconstruction of a 10 vol% LCO and 0.6 vol% Ketjen suspension obtained using X-ray tomography.

2.2. State of the Art of Experimental Developments

Following the first publication, SSRFBs with different materials were demonstrated by various research groups: (i) a full-cell based on carbon coated $LiTi_2(PO_4)_3$ and $LiFePO_4$ with KB in aqueous electrolyte[70]; (ii) a half-cell with $LiFePO_4$ with KB in commercial LP30 (EC:DMC:$LiPF_6$) electrolyte[71]; (iii) a half-cell with silicon with KB in LP30[72] and EC:DEC;[73] (iv) a full-cell with P2-type $Na_xNi_{0.22}Co_{0.11}Mn_{0.66}O_2$ and $NaTi_2(PO_4)_3$ in EC:DMC:$NaPF_6$ (0.5 M)[74] and (v) half cells with $LiTi_2(PO_4)_3$ or $LiNi_{1/3}Co_{1/3}Mn_{1/3}O_2$ with KB in LP30.[75] These studies provide the proof of the great potential that SSRFBs have in terms of utilizing a variety of active materials, conductive additives, and electrolytes. However, as the following chapters will elaborate, these studies also

demonstrate that traditional electrochemical techniques that are used to study LIBs fail to provide systematic and quantitative explanations of trends observed for SSRFBs.

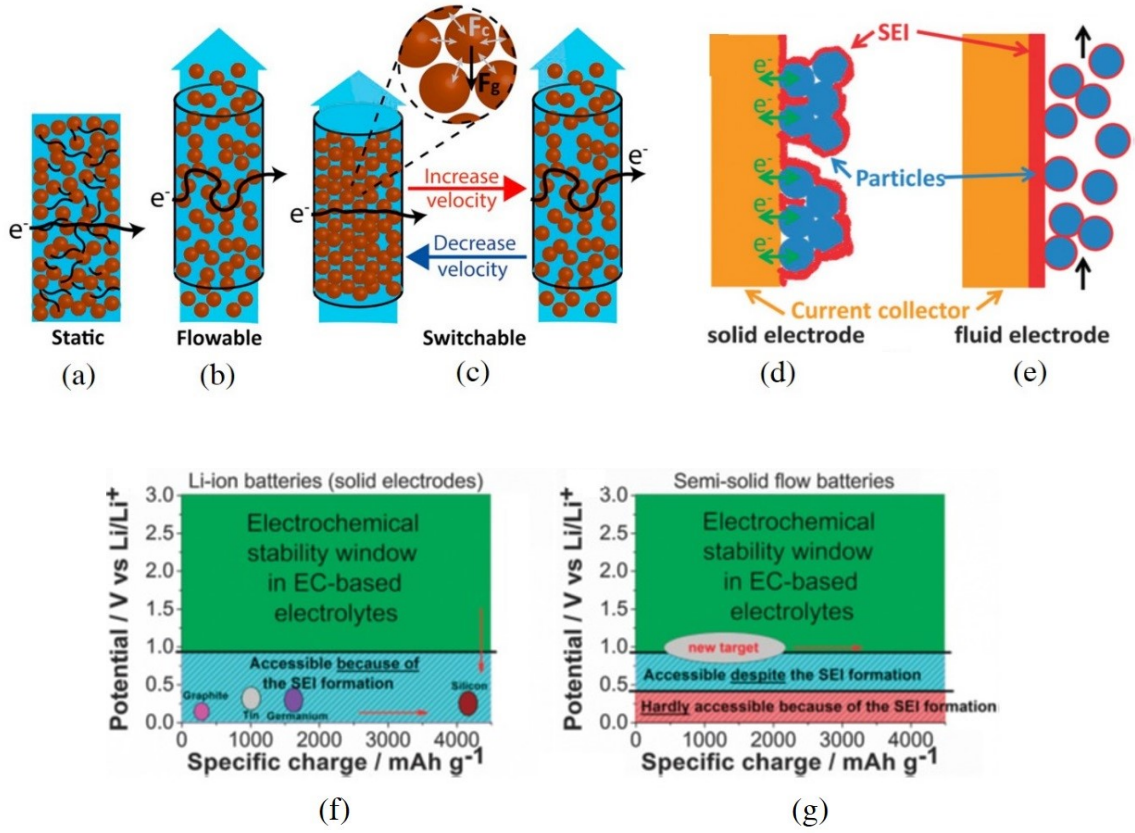

Figure 2.4. (a) Standard solid electrode with particles held with binder, (b) slurry electrode under flow, (c) Proposed mechanism of switchable electrode.[76] Extent of SEI formation on particle surface for a (d) standard solid electrode and (e) slurry electrode. The potential window available for (f) standard LIBs and (g) SSRFBs.[77]

In addition to the studies mentioned above, engineering based and phenomenological studies are also found in literature. For instance, in a very recent study, an electrode capable of switching between flow and static modes *in operando* has been proposed; offering greater technical and operational flexibility.[76] Transition velocities required to switch between modes are shown to be strongly influenced by aggregation and interaction forces between particles.[76] Another study illustrates the deleterious impact of solid electrolyte interface (SEI).[77] The SEI is an electronically insulating thin film formed when the active material is electroactive outside the stability

window of the electrolyte. When the SEI deposits on the entire surface area of the suspended active material particles, it can result in complete electrical insulation of a given particle and a consequent loss of capacity.[77] Evidently, as the SEI modifies the surface of active material particles, it may potentially impact aggregation and flow behavior as well. Given the various kinds of studies, two main approaches have been found in literature for SSRFBs; (i) the use of more sophisticated experimental tools to enhance fundamental understanding of mechanisms and (ii) the study of the response of SSRFBs to modifications induced by additives and different material combinations.

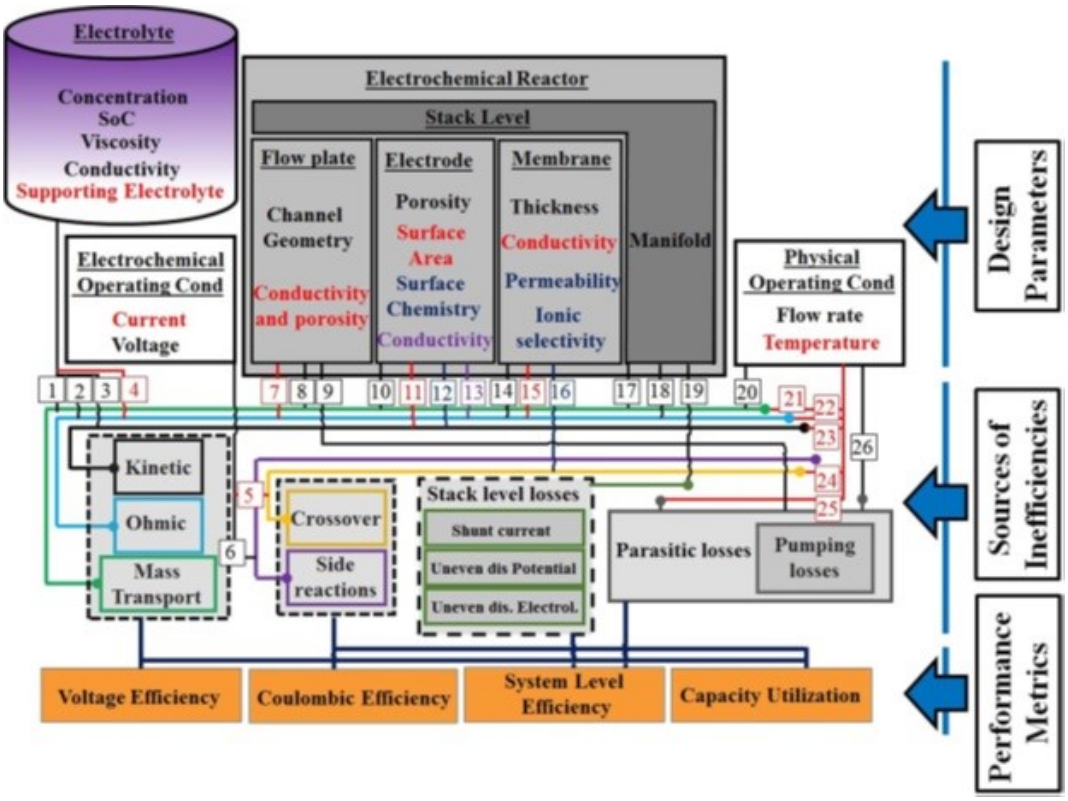

Figure 2.5. Schematic proposing how the stages of the design process can be correlated to inefficiencies and visually mapping them to the various sources of losses for RFBs. This provides a bridge between diagnostic techniques and performance metrics.[21]

A recent review by Gandomi *et al.*[21] on diagnostic and characterization tools for RFBs provides a comprehensive picture of important research goals. At the material chemistry level it is essential to decrease material cost while simultaneously improving power and energy density so that system cost consequently falls. For SSRFBs, this implies the added goal of optimizing material performance and reversibility specifically for multiphase electrodes. To ensure battery durability, capacity decay and parasitic losses need to be mitigated with appropriate system design. Furthermore, implementation of battery management systems on commercialization requires the development of rigorous mathematical models. In their review, Gandomi *et al.*[21] show that optimized battery architecture is chemistry-dependent and that loss mechanisms can only be dealt with when the complexity of (i) electron and charge transfer on the surface and (ii) electrode reaction mechanisms, are fully understood.[21] Thus, the need to probe mechanistic details of electrochemical phenomena in suspension electrodes is critical if SSRFBs are to be optimized.

Simultaneous rheo-electrical studies by Lestriez et al.[78] provide a much needed window into the complexity of SSRFBs.[78] Slurries with conductive additives, C45 and KB, in organic electrolyte propylene carbonate (PC) show that on increasing the concentration of the additive, three distinct regimes emerge: weak rheological gel, strong rheological gel, and electrical percolation (Figure 2.6). The viscoelastic nature of the suspension reveals a transition from shear thinning to a brief shear thickening regime, followed by shear thinning again. While electronic conductivity is shown to depend on the existence of particle networks, this is true only below percolation threshold. Above the threshold, it is suggested that conductivity follows a bell-shaped curve. It is reported that initially, on increasing shear rate, conductivity decreases because three-dimensional networks break down, but afterwards, conductivity increases due to probable electron tunneling mechanisms between particle aggregates. In terms of conductivity and viscosity, KB is shown to be superior to C45, owing to significantly higher surface area.[78]

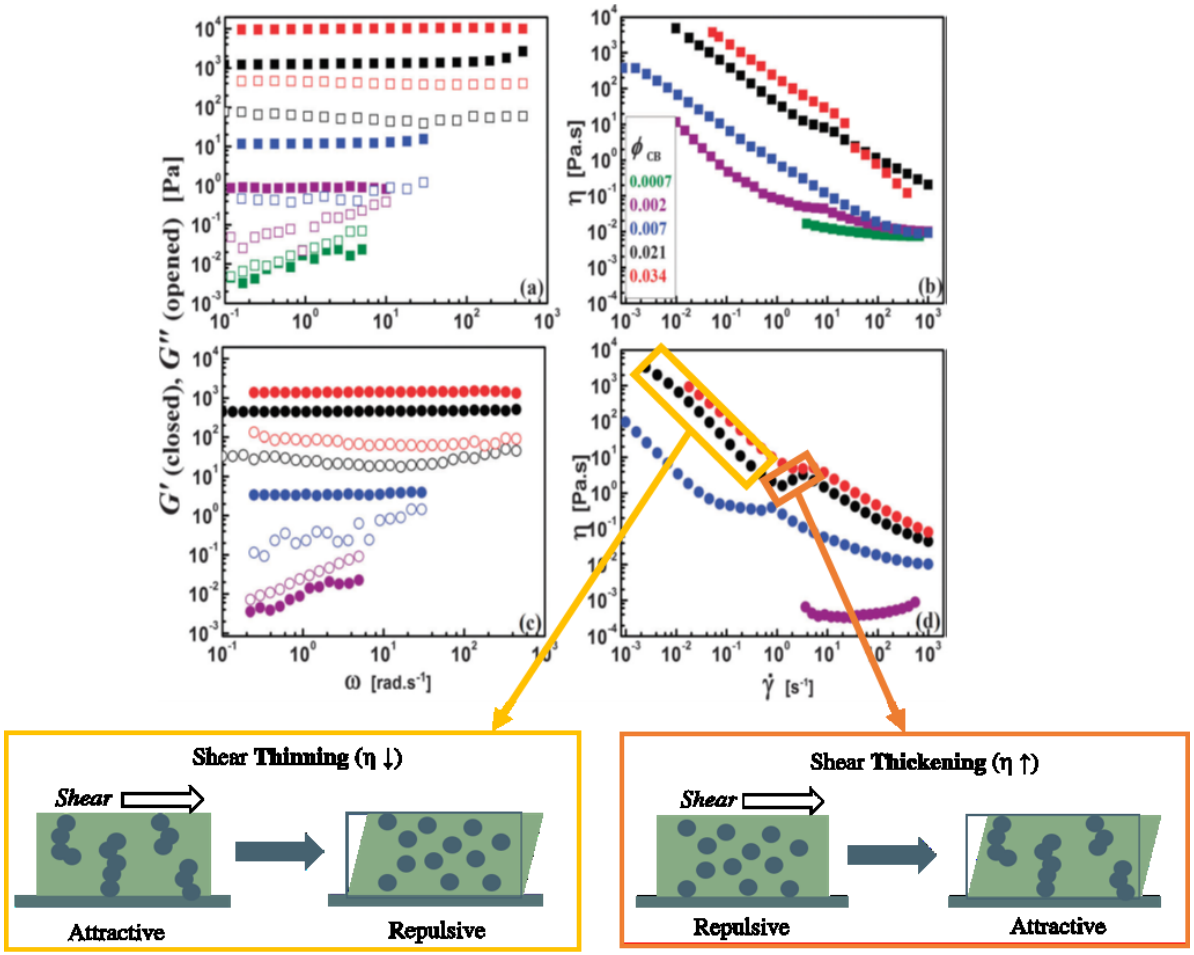

Figure 2.6. Oscillatory frequency sweep (a and c) and steady shear rheology (b and d) at different carbon volume fractions for KB (squares) and C45 (circles) carbon black suspensions in 1 M LiTFSI in PC. The viscoelastic behavior is captured here by G' (elastic/solid part, describing energy storage modulus) and G" (viscous/liquid part, providing energy dissipation modulus). For G' > G" gel-like behavior is seen, while for G'< G", liquid-like behavior dominates.[78]

To the above data from literature, schematics for mechanistic details of shear thinning and shear thickening are provided at the bottom to explain the variation of viscosity (η) with increasing shear rate.

Parameter sensitivity analysis with multiple parameters are reported for studies based on $Li_4Ti_5O_{12}$ (LTO) and KB in PC; it shows the impact of channel depth, active material concentration, and C-rate on discharge capacity.[79] Interestingly, increasing LTO negatively influences both rheology and conductivity of the slurry in this study.[79] When comparing suspensions of carbon black in aqueous and organic media, despite a higher percolation threshold seen in the former, its plateau modulus is lower and electrical conductivity is higher.[80] Another study shows that the addition of non-ionic surfactant to slurries of LTO and KB in PC works to increase the inter-particle repulsion. This possibly stabilizes the slurry to promote good electronic connectivity even at large channel depths which would otherwise show poorer capacity.[81] Carbon nanofibers (CNFs) as additives to suspensions containing carbon black have shown to provide additional elasticity and rigidity to the particle networks while maintaining conductivity.[82]

A significant step towards tailoring interactions between particles was the creation of *biphasic* suspension, *i.e.* a mixture of attractive and repulsive particles, such an electrode showed high energy density and fast charge transport at low-dissipation flow.[83] The interactions between LFP particles and those between KB-LFP are made repulsive by addition of non-ionic dispersant, to maintain good dispersion. On the other hand, interactions between KB particles are made attractive to enable formation of percolation networks. From shear viscosimetry and oscillatory measurements, it is evident that the addition of dispersant lowers stiffness of the percolating network, thereby offering a means to tune flow behavior, thus greatly reducing time-averaged pumping rate.[83]

The use of Arabic gum as emulsifier and alginate as Newtonian viscosifier has been reported by Parant *et al.*[84] to delay sedimentation by increasing viscosity of carbon suspensions in water; their impact has been studied with Zeta potential and XPS measurements. The same study reports a comparison between three types of carbons, namely compressed carbon acetylene black, ENSACO, and KB. These suspensions show good electronic conductivity even under flow conditions and this observation is attributed to formation of networks below percolation threshold.[84]

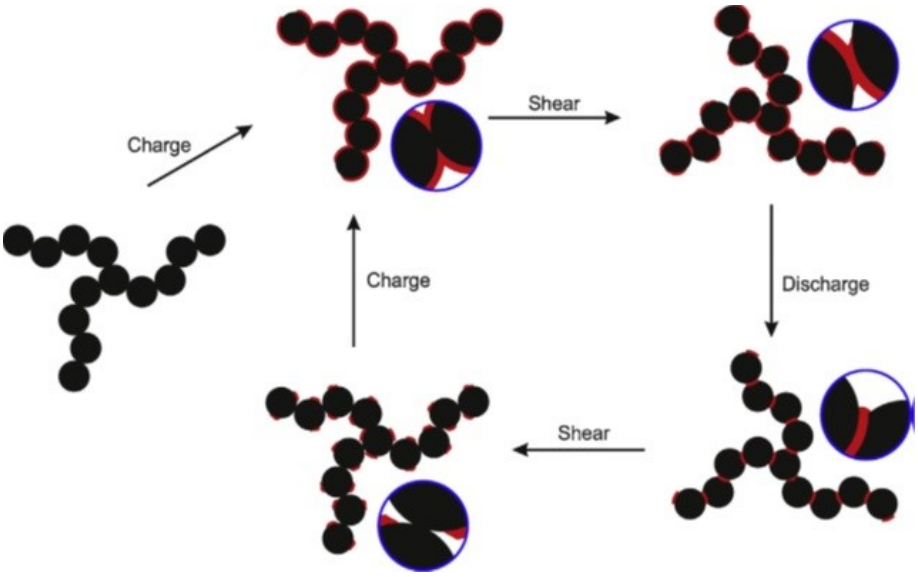

Figure 2.7. Proposed mechanism to explain the observed combined effect of (dis)charging to higher potentials and subsequent mechanical rejuvenation on the LFRI (Low frequency real impedance from the conductivity of the KB network). Red color indicates (in an exaggerated way) the presence of an SEI layer, which grows during charging, and shrinks during discharging. Particle contacts are less strongly affected by layer deposition or dissolution.[85]

Duits *et al*.[85] report a wide spectrum of information by coupling rheology and electrochemical impedance spectroscopy, where measurements are made alternatively between both techniques. Studies on suspensions of LTO and KB in LP30 suggest that electronic resistance and yield stress are a function of lithiation.[85] A mechanistic picture based on temporally evolving SEI is provided to explain the changing nature of KB particle interactions that impact rheology (Figure 2.7). Other studies suggest that at higher voltages, SEI layer is sparse, less insulating, prone to dissolution, and predominantly organic; while SEI at lower potentials is thicker, denser, less soluble, more insulating, and comprised of inorganic compounds.[85] To simplify the SSRFB system, choosing materials that do not form dynamic SEIs is highly recommended.

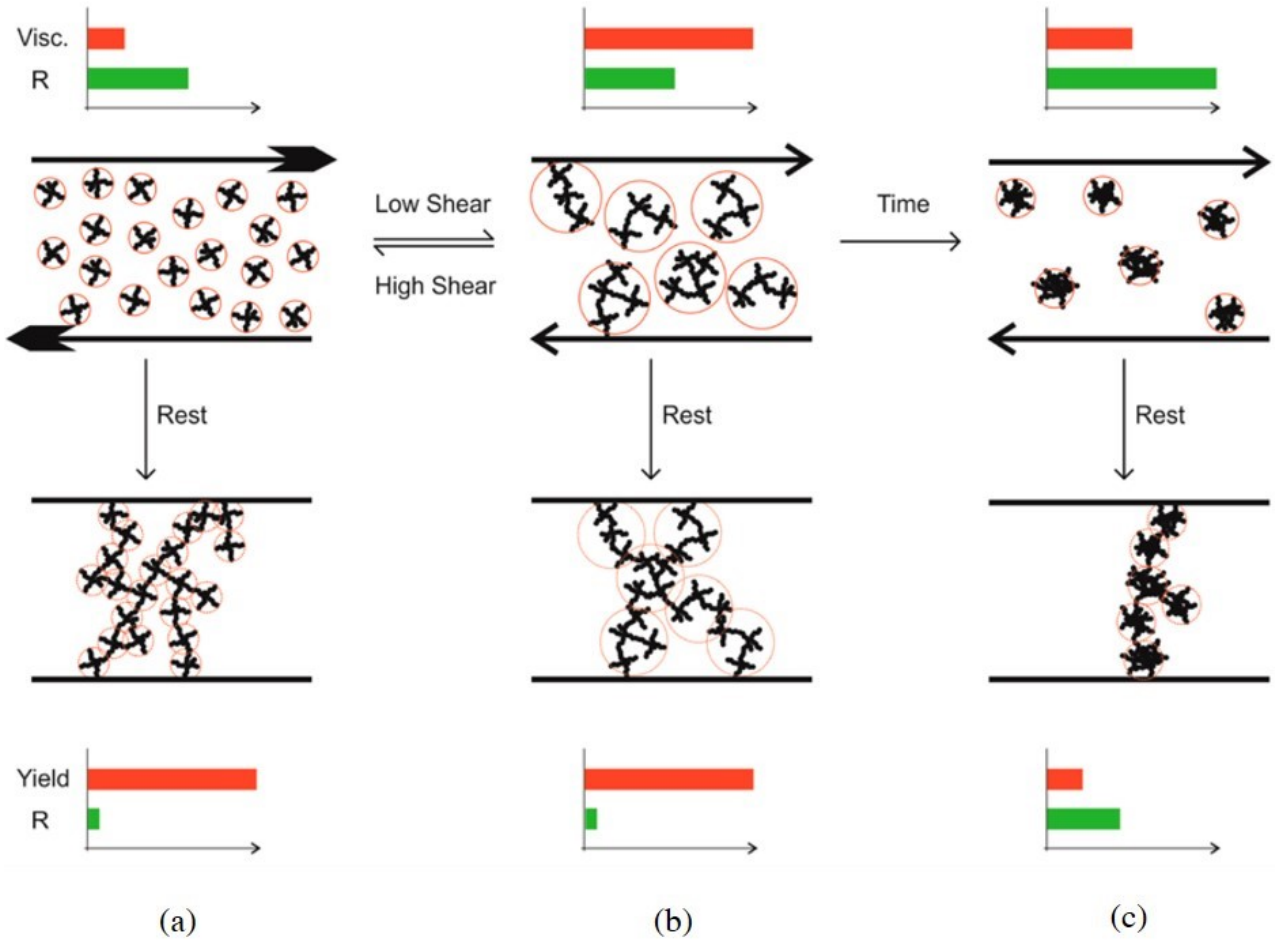

Figure 2.8. Proposed mechanism to justify viscosity and resistance trends of flowing slurries at different shear rates for long and short term shearing, in addition to impact of rest on resistance and yield stress.[86]

Another study by the same group showed low frequency real impedance and viscosity responses to change in shear rate. It demonstrated that shearing history has an impact on rheo-impedance measurements and must be taken into account for all research conducted with viscoelastic suspension.[86] The mechanistic description proposed suggests that a fast or immediate response arises from open agglomeration and that a slow response arises from densification of aggregates (Figure 2.8). The fast response exists under low shear rates and provides higher electronic conductivity and higher viscosity. The slow response emerges at high shear rates, resulting in lower hydrodynamic volume fraction, reduced viscosity, and also reduced electronic conductivity, due to less number of available pathways. These observations have been verified by a model based on the Krieger-Dougherty equation

to capture the hydrodynamic volume and the Potanin model to capture a relationship between agglomerate radius and fractal dimension.[86] In a more recent publication, Duits *et al.*[87] reported a rheometer capable of *in situ* impedance measurements. Significant correlations between low frequency real impedance and yield stress were observed for both half-cell and full-cell configurations.[87]

In two recent studies, the combined use of small angle neutron scattering (SANS), ultra-small angle neutron scattering (USANS), dynamic light scattering (DLS), oscillatory rheology, and impedance spectroscopy offers the most elaborate synergistic experimental effort to connect structural, mechanical, and electrical behavior of carbon black suspensions.[88,89] The most significant finding of the first study is that electron hopping is seen to be the dominant charge transport mechanism both below and above gel transitions; as opposed to particle networks or stress bearing chains which are generally regarded as the reason for electronic conductivity. It is shown that gelation does not arise from strong attractive forces between primary aggregates, but rather, a clustered fluid phase is created that forms system-spanning particle network when further concentrated. The means through which shearing impacts electronic conductivity is not by breaking up particle networks but rather by impacting cluster size that consequently affects the dominant hopping mechanism.[88] While the exact nature of electron hopping mechanism in suspensions is worth further study, this clearly demonstrates how preconceived notions of the correlation between electronic conductivity and spatial arrangement of particles, as adopted from LIB field, led to the belief that particle networks are an important qualitative explanation of trends observed in SSRFBs.

The second study uses the inverse Bingham number, which is a ratio of measured or applied shear stress to the yield stress, to distinguish between two distinctive flow regimes (Figure 2.9): (a) Open networks with relatively small agglomerates at $Bi^{-1} > 1$, and (b) shear driven, loosely connected, denser agglomerates which accompany steep decrease in both apparent viscosity and conductivity with shear time eventually leading to sedimentation at $Bi^{-1} < 1$.[89] Such multipronged experimental studies are expected to provide groundbreaking discoveries of hidden mechanisms that govern electrochemical systems and may transform the black box of batteries into a system that can be tailored and optimized more effectively.

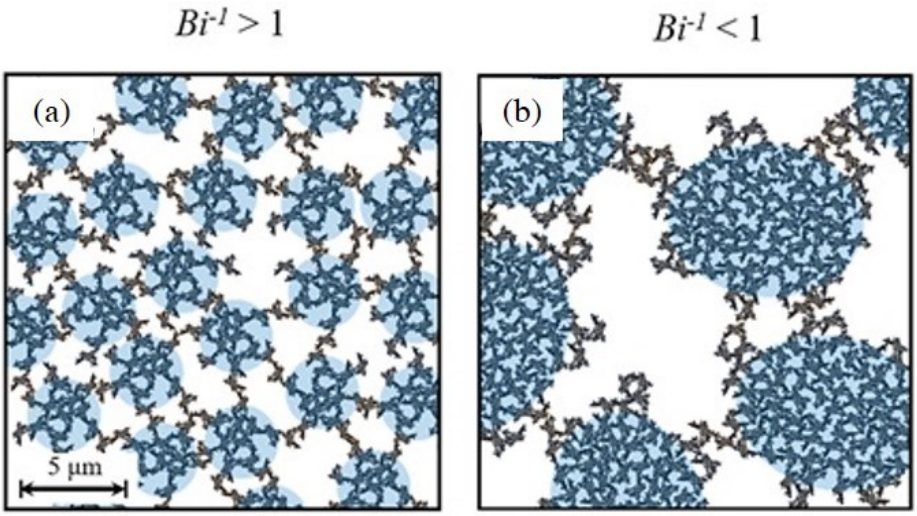

Figure 2.9: (a) Small, loosely held agglomerates forming electronically well connected, open aggregates at high inverse Bingham numbers and (b) small agglomerates densifying under shear to form aggregates with poorer electronic conductivity.[89]

2.3. State of the Art of Models and Theory

Along with experimental studies on SSRFBs, the first continuum models came out after 2012; these involve incorporation of fluid convection terms to Newman's porous electrode model along with power law based hydrodynamic flow to capture non-Newtonian behavior of the suspension.[90–93] The model first described by Brunini *et al.*[90] assumes constant lithium concentration within the solid particles to circumvent solid state diffusion limitations and simplify the challenges of multiscale modeling, while ion diffusion in liquid is taken into consideration using a simple 3D diffusion model. Furthermore, the assumption of constant current density boundary conditions, which is typical in solid electrodes, is lifted.[90] The main conclusions of these modeling studies (Figure 2.10) are that: (i) spatial uniformity of current extraction and stoichiometric flow depend on the voltage profile;[90] (ii) intermittent or plug flow mode is beneficial for extracting maximum capacity from the slurry electrode;[20,91] (iii) extended electroactive zones can exist, *i.e.* electrochemical activity can be observed in pipes

just outside the cell, and their impact can be minimized through appropriate design and operating conditions.[92] In order to distinguish between flow batteries and flow capacitors, a capacitive Damköhler number has been introduced.[93] This number is essentially a ratio between exchange current density and Peclet number, which in turn is the ratio of advection to diffusion. Based on the assumption that infinitely fast pulses during intermittent flow can help isolate electrochemical phenomena from fluid flow phenomena, the use of a discretized model using finite volume method is possible.[91] Even without considering an explicit correlation between fluid and electrochemical behavior, this study shows that electrochemical efficiency can be improved through better flow volume control, tailored suspension rheology, and resistance to flow can be reduced by enhancing slip. However, these indications are qualitative guidelines and don't necessarily provide specific information for more efficient experimental optimization of the system.

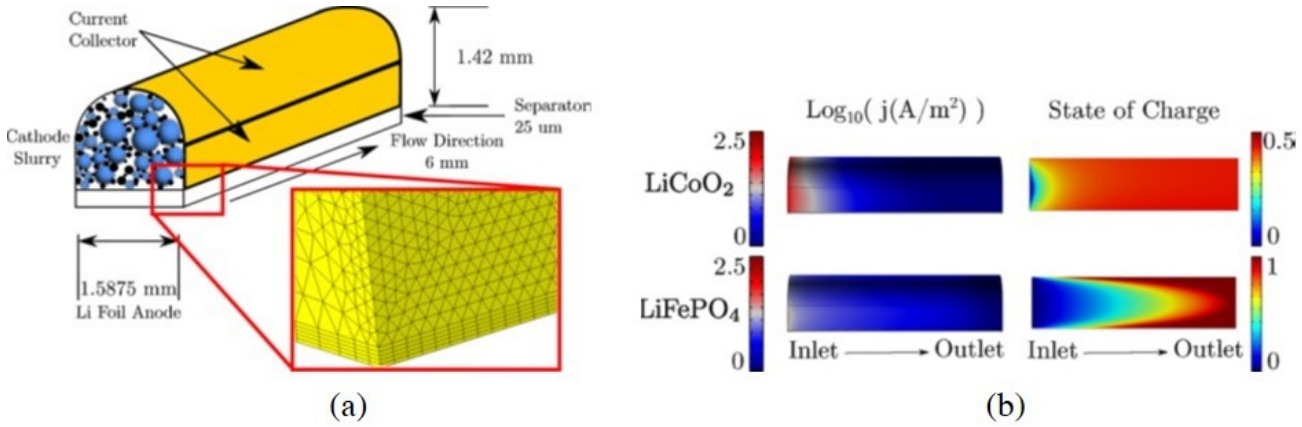

Figure 2.10. (a) Inset showing the mesh used in the model (b) Comparison of the steady state current density and state of charge distributions along a flow channel, in stoichiometric flow mode at C/20 rate.[90]

Models used for RFBs and SSRFBs have a basic structure in common, it is addressed in a review article by Xu *et al*.,[52] summarized by Lacroix *et al*.[75] and will be briefly mentioned here. Fluid flow is captured by Darcy's law, which represents an empirical relationship between dynamic viscosity, porous electrode permeability, and fluid velocity to express fluid pressure. Navier Stokes equation is used to model the non-Newtonian fluid with a power law viscosity. Mass conservation equations are used to estimate ion transport and heat generation from flow

is also taken into account. Potential and current distribution in solid phase is governed by Ohm's law, potential in electrolyte phase and salt concentration in liquid phase are also calculated.

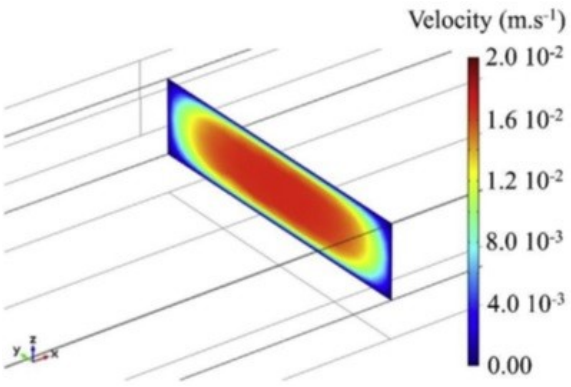

Figure 2.11. Velocity profile of LTO suspension in the channel where pressure drop can be noticed on the sides and corners and velocity is relatively homogenous in 80% of the channel.[75]

Lacroix *et al.*[75] used this modeling scheme to capture the behavior of two half-cells under flow; unlike the model by Brunini *et al.*,[90] ionic transport in liquid phase was ignored. The model was developed to handle lithium concentration gradients in solid for intercalation type compounds, it was reported that it could, in the future, take into account other mechanisms of lithiation as well. Experiment and model showed consistency in rheological behavior of suspensions under flow. The overall pressure drop is low, low pressure is observed at the channel walls and corners (Figure 2.11), and changing flow rate shows little or no effect on pressure drop. Electrochemical behavior of the model shows correlation with experiment but with some significant deviations that are said to arise from inhomogeneity in potential due to rising internal cell resistance. Since the model does not take into account electro-rheological effects as a function of time under flowing conditions, the explicit impact of shearing at mesoscale cannot be captured, especially the way morphology of conductive particle agglomerates and clusters impact conductivity.[75]

By expanding the number of phenomena taken into consideration, such studies can potentially unearth a multitude of emergent phenomena, making SSRFBs more intuitive to study. Recent theoretical developments

relevant for SSRFBs also lean towards taking greater phenomenological intricacies into account. Advancement in theory for electrochemical impedance spectroscopy for *in situ* characterization has been proposed by Hoyt *et al.*[94] and it incorporates current induced by convection of surface charge on particles under flow. An impedance element that accounts for oscillatory behavior of surface charge boundary layers is added in series with contact resistance in the equivalent circuit. This study, performed in context to flow capacitors, provides a quantitative means to capture electronic diffusivity, slurry conductivity, and contact resistance as a function of flow rate.[94]

Another study addresses how diffusion is hindered in confined spaces and while this effect is significant in some fields, like zeolites[95] or drug delivery,[96] it has only recently been applied to electrochemical particle systems.[97] The theoretical framework proposed by Chan *et al.*,[98] incorporates Nernst-Planck equation to capture mass transport by diffusion and migration, the Gouy-Chapman model for electrode-electrolyte interface, and a hindered diffusion model[99] that takes into account modification of Brownian motion due to presence of the interface. Migration and hindered diffusion are shown to compete with one another and this competition determines the tendency of particles to accumulate at the interface; thus providing a means to tune mass transport.[98]

Electronic percolation, vital for the functioning of SSRFBs, has also been elaborated theoretically. A recent study by Golovnev *et al.*[101] proposes an analytical probabilistic framework, for particles with high aspect ratio which are expected to provide higher conductivity and better flowability at lower solid concentrations.[84] It predicts percolation threshold more accurately than excluded volume theory and can provide a detailed mesoscale picture of particle networks above the threshold; it thus creates a basis for structure-property relationships. This generalized framework offers more opportunities like implicitly accounting for interaction potentials, influence of solid interfaces, and particle alignment due to electrolyte flow.[101]

A recent modeling approach by Lohaus *et al.*[100] reports coupling of Butler Volmer based electrochemical dynamics with Computational Fluid Dynamics (CFD) and colloidal physics based on Discrete Element Method (DEM). This approach simulates the dynamics of percolation networks as a function of solid volume fraction.

Fluctuations in current density are coherent with the discrete nature of DEM and the magnitude of current density and 3D visualization of state of charge of particles are used to ascertain extent of percolation.[100]

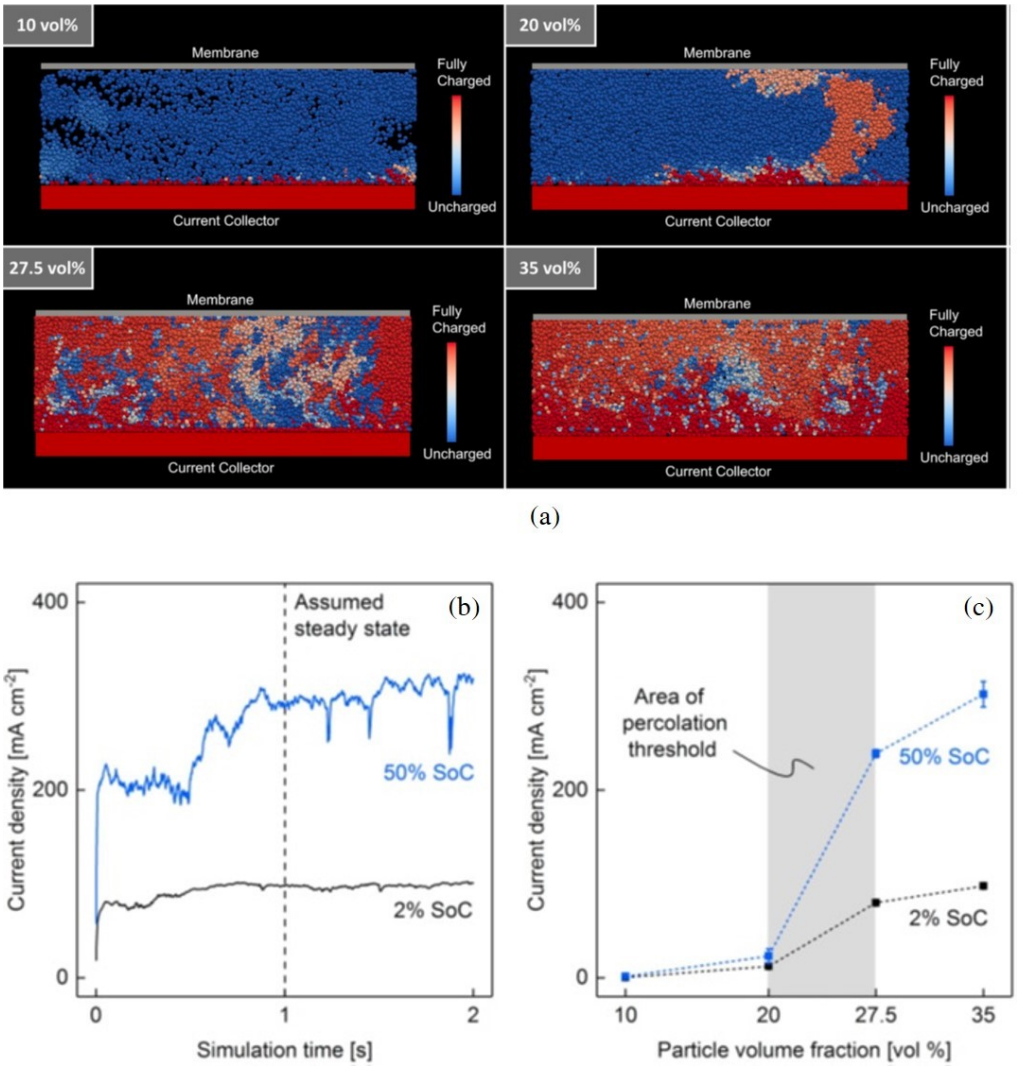

Figure 2.13. (a) Visualization of the charge distribution on the slurry electrode particles at 50% state of charge and 10, 20, 27.5 and 35vol.% particle volume fraction. (b) Net currents at different states of charge varying as a function of time. (c) Impact of state of charge on the percolation threshold.[100]

2.4. Conclusions

When looking deeper into the state of the art of SSRFBs, it becomes evident that rather than forming a clearer picture of underlying mechanisms, studies appear to provide phenomenological explanations based on conflicting assumptions. For instance, silicon and carbon based slurries are shown to maintain both good and bad inter-particle contact under cycling.[72,73] The contribution of interface between current collector and slurry towards electrical resistance is shown to be both significant and insignificant.[25,85] Two schools of thought explain the mechanism of electrical conductivity in slurries; one wherein particle networks are known to dominate and another wherein electron tunneling dominates such that distribution and size of particle clusters is more important (Figure 2.14).[78,84,88,102] The zeta potential of conductive carbon suspensions in organic electrolyte also cannot be generalized to either always positive or always negative; furthermore, the size of the cation used in the electrolyte is shown to be significant.[78,103] The impact of channel depth on electrical conductivity of slurry is shown to vary with multiple simultaneous parameters like flow rate, active material concentration, and C-rate.[25,79]

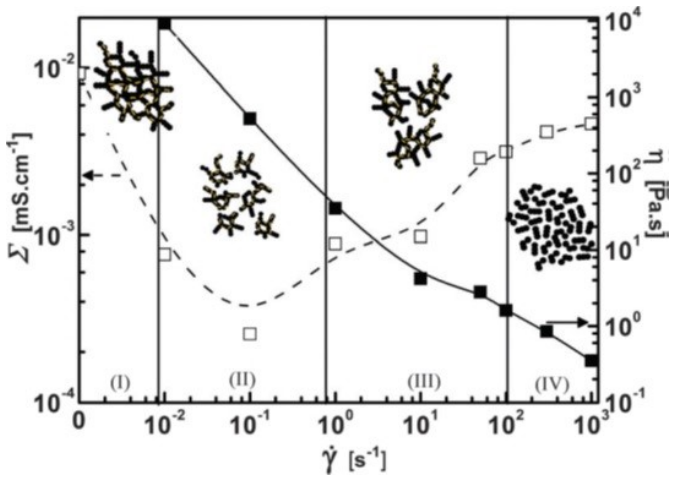

Figure 2.14. Variation of the conductivity and viscosity with the shear rate for KB suspensions as a demonstration of complexity : (I) a 3D network of agglomerates; (II) breakup of the network into agglomerates; (III) formation of hydro-clusters or anisometric agglomerates; (IV) erosion into small agglomerates or even single aggregates.[78]

The experimental work attempted in this thesis work offered significant optimization challenges. A brief overview of various studies is mentioned in the Appendix A.2, difficulties faced can be linked to the nature and source of silicon particles plays a significant role in the stability and electrochemical nature of the slurry. While no conclusive results were obtained, this work helped provide a sound foundation for building the model and in general, provided evidence of the complex challenge that a researcher will confront when attempting to create a SSRFB with new material.

The literature consists predominantly of continuum modeling approaches so that CFD can be intuitively incorporated to simulate flow conditions. However, from this reference point of continuum models, modeling studies attempt to relax certain assumptions, for instance the current density boundary condition[90], to obtain more information. Readdressing assumptions of a model provide the grounds for computational efficiency, for instance how considering infinitely fast pulse in intermittent flow allows for continuum modeling.[91] In a manner of speaking, modeling literature tends to negotiate between obtaining more detail and simplifying the problem. On one hand, swapping assumptions in and out of a modeling framework without concrete experimental backing may lead to creation of models that have poor prediction capability and on the other hand, the range of exploration of continuum models may not be sufficient. Particle interactions and electrochemical phenomena clearly play a dominant role in SSRFBs, thus a significantly high degree of discreteness in a model may be necessary.

Additionally, when playing with assumptions that are challenging to prove, it becomes relevant to create models based on a holistic picture, in the form of an interconnected web, so that the theoretical framework is as self-correcting as possible. This can minimize the potential errors introduced from hypothesis which are not rigorously introduced. Building elaborate graphs to show interconnections between phenomena and using agent-based models wherein particles have autonomy to experience phenomena, as described in this work, provide such a self-correcting nature. It is therefore vital to build mechanistic models where mechanisms and on-the-fly evolution of parameters drives simulations. Such approaches can also be categorized as complex adaptive models that follow the principles of complex adaptive and dynamic systems.[104]

While the approach and findings reported by Lohaus *et al.*,[100] as shown in Figure 2.13, represents a first step in this direction, this thesis work addresses the numerous aforementioned challenges more rigorously. Our work also shows how establishing a reliable model and obtaining experimentally verifiable results from mechanistic models is not straightforward and what tools can be used to counter that.

From the perspective of fields of research, it is clear that standard experiments and models developed to study either LIBs or RFBs are an insufficient means to achieve commercialization, and standard performance metrics do not appear to offer much insight. There is a tendency in both experimental and modeling studies to incorporate more and more phenomena which were traditionally not studied in context to LIBs, showing the importance of considering more complexity. Due to the lack of concrete and generalized quantitative understanding, it can be concluded with certainty that SSRFBs are complex systems. Non-linearity and non-intuitiveness are hallmarks of complexity and any emergent behavior is merely the appearance of unanticipated phenomena that tend to confound and polarize the scientific community. Therefore, this study provides a good basis to study a more abstract and fundamental phenomena, *i.e.* complexity in electrochemical systems, that is found in disciplines that are otherwise considered to have little in common.

Chapter 3

Description of the Model

3.1 Basis of Approach

The previous chapter on the state of the art of SSRFBs shows that it is not straightforward to understand and predict SSRFB device behavior; therefore it becomes relevant to find reliable fundamentals to build upon. If multiple relationships exist between parameters and phenomena such a system can be termed as *complex*. This complexity can arise either from (i) a lack of understanding of the system, such that after sufficient trial-and-error, a set of simple relationships will emerge, or (ii) the nature of the system is such that simple relationships, mathematically speaking, may not exist. The latter makes it especially very hard to cross early stages of device development. Complexity in SSRFBs is expected to be a mix of both categories, (i) and (ii). While a lack of understanding can be overcome by extensive systematic studies, complexity arising from category (ii) is a result of the many-phenomena problem (with multiple competing forces), the many-body problem (where particle behavior at the mesoscale is non-trivial) and the many-scale problem (where interactions occur across length and time scales), which generally manifest simultaneously.

The many-body problem at mesoscale is especially prevalent in suspension electrodes since rheological behavior and interaction between particles cannot be generalized and represented as analytical equations. Even in solid electrodes for LIBs, where particles of the electrode are not free to move, the presence of inhomogeneity at nanoscale and mesoscale is known to impact lithium ion transport experimentally.[105] Thermodynamic studies on insertion materials show that voltage hysteresis also originates from collective particle behavior.[106] This domino cascade effect, where particles are shown to sequentially undergo charging and discharging has also been experimentally observed.[107] Battery models that treat electrodes as effective media, where discharge occurs simultaneously in all particles cannot capture this effect; it thus promotes interest in 2-D or 3-D models that consider multi-particle interactions.[108] Typically, to address these challenges, models that were originally developed for microscale and computationally parallelized for efficiency are used for describing particle dynamics, such as Molecular Dynamics, Dissipative Particle Dynamics, Brownian Dynamics, or Stokesian Dynamics.[109–114] These established techniques are inhibitory for causal discovery because these are computationally programmed

in accordance to certain empirical and theoretical assumptions. If, in a given system, the physical phenomena are very poorly understood and the many-body problem is significant, it is imperative to allow an open theoretical framework for empirical equations. Additionally, based on the need, it can help to accommodate a spectrum between continuum and a discrete particle simulations. The purpose of the study in this thesis is to explore the use of kinetic Monte Carlo (kMC) to create such an open, self-correcting modeling framework, designed especially for causal discovery.

The electrochemical system chosen herein is based on studies previously conducted in our laboratory with slurries composed of silicon and carbon.[72] When the galvanostatic behavior of the slurry electrode (Figure 3.1(a)) was compared with those of solid electrodes either with binder (Figure 3.1(b)) or without binder (Figure 3.1(c)), it was noted that reasonable retention of capacity and low polarization was obtained. The initial irreversibility of the electrode was ascribed to formation of thick solid electrolyte interface due to the large excess of electrolyte present in the SSRFB when compared to solid electrodes.[72] It was proposed that the advantages arise from the breathable space silicon particles have, to experience volume expansions and contractions during electrochemical cycling. For the model considered in this study, the mechanical stresses and phase changes of silicon during cycling are simplified and single phase lithiation is assumed. This corresponds to the electrochemical behavior typically seen from the second cycle onwards, wherein all of the silicon can be assumed to be amorphous.[115] It is also possible to take into account how electronic conductivity of silicon, a semi-conductor, increases after lithiation. An increase in density of state at the Fermi level is indeed reported by first principles simulations.[116]

A mechanistic picture of coexistence of rheology and electrochemistry for a slurry in static, *i.e.* non-flowing mode, is essential before fluid dynamics can be included. The particle size of battery materials falls within the range of the definition for a Brownian particle. Therefore, the particle motion here is random, or computationally pseudo-random, and not biased towards a direction to mimic flow. Studies have been done to find an appropriate algorithm to take flow into account within the event list of a kMC model, and can be taken into account in future generations of this algorithm.[117,118] Furthermore, the assumption not to take fluid dynamics into

consideration also stems from the numerous studies which recommend intermittent flow mode for discharging batteries,[20,91] thereby rendering the slurry essentially immobile during a consequent portion of the period of interest.

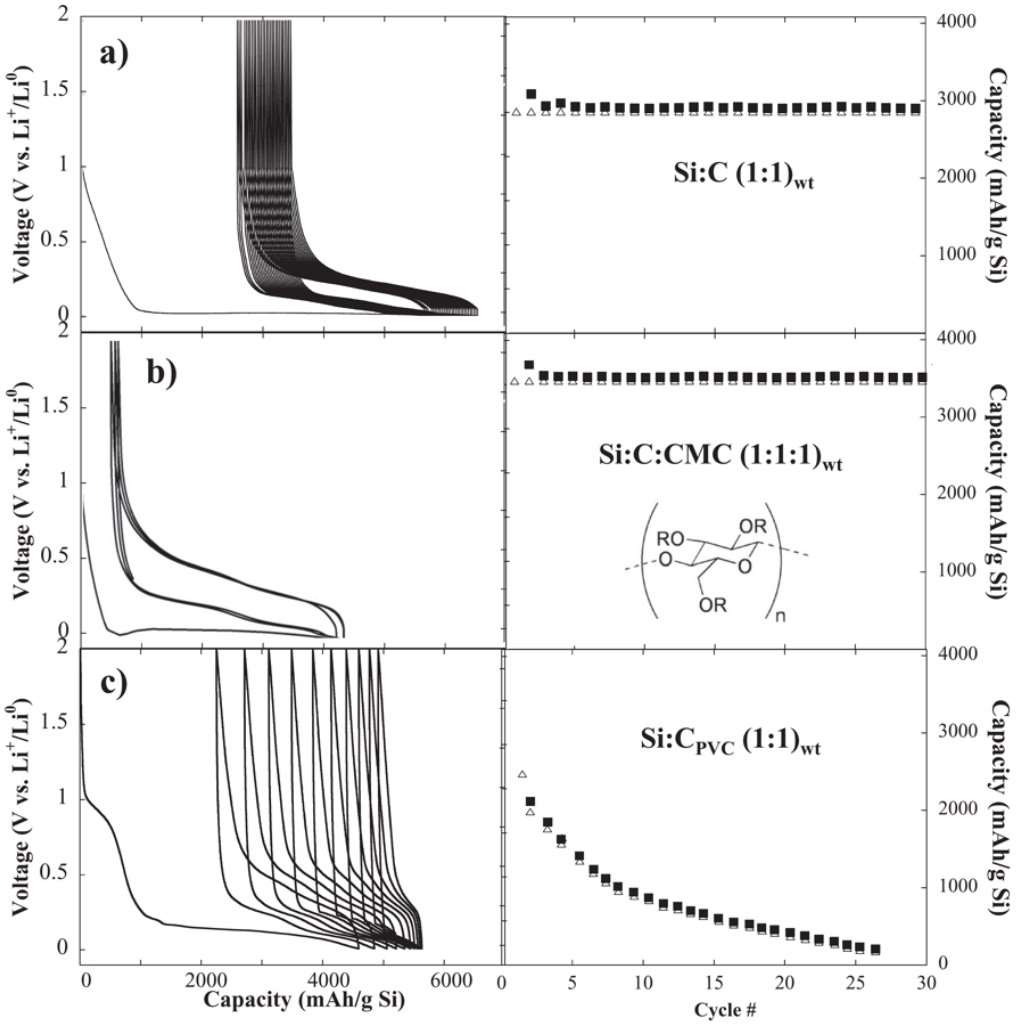

Figure 3.1. Galvanostatic curves and capacity retention plots for discharge versus lithium metal for (a) suspension electrode, (b) Si/C/CMC composite electrode and (c) Si/C from pyrolyzed Si/PVC blend.[72]

At this stage, only a simplified picture of rheology will be considered as a first approach to estimate effective viscosity of the suspension while still explicitly simulating particle motion. Once this framework is more established, models addressing phenomena at other scales can potentially be incorporated for more detail, in future

work. For instance, a mechanistic model can be created for interfaces to capture the nature of SEI. This can be used as a particle surface property at a higher scale, for instance to assess the degree of aggregation with particles of the same or different type. Such information, for example, can help predict conditions for clustering, network formation, or sedimentation.

3.2. Description of Framework

The following sections elaborate the tools used to build the in-house mechanistic model in Python programming language. A set of empirical expressions are first presented that establish the physical core of the framework. The evolution of the model in space and time is governed by kMC. The phenomena are captured through the simulation of particles as agents in a three-dimensional Agent-Based Model (ABM). The use of object oriented programming allows more structured handling of the simulation, especially to quantify and update properties associated to each agent or particle, thereby providing an insight at mesoscale. Given the high degree of flexibility and ongoing development of the model, only the essential aspects are described in this chapter. A more extensive explanation of the Python tools and algorithms used is mentioned in the Appendix, section A.1.1. Other modeling work attempted is also briefly mentioned in A.1.2.

As highlighted in the conclusion of Chapter 2, this ensemble of methods, along with parameter sensitivity analysis and graph theory, as described in the following chapters, provides an example of how a mechanistic model with self-correcting and complex adaptive nature can provide important insights. Taking into account as many phenomena as possible within the theoretical framework can provide the checks and balances needed when many hypotheses are being made.

3.2.1 Equations governing physical phenomena

The main physics included in this model pertains to particle motion and electrochemistry. Particles are chosen to move in random directions, with frequency of motion based on kinetic rates originating from diffusion coefficient, which in turn is influenced by particle size and slurry viscosity. The Stokes-Einstein equation (Eqn. 3.1) is used to express the diffusion coefficient ($D_{i,j}$) as a function of the viscosity of the slurry (η_{sl}) and particle radius ($r_{i,j}$),[119] where subscript *i* refers to particle type (Si or C) and *j* refers to the identity of the specific particle, k_B is the Boltzmann constant and T is temperature:

$$D_{i,j} = \frac{k_B \,.\, T}{6 \,.\, \pi \,.\, \eta_{sl} \,.\, r_{i,j}} \qquad \text{(Eqn 3.1)}$$

The viscosity of the slurry (η_{sl}) is estimated as a product of pure liquid viscosity (η_l) and relative solid viscosity (η_r). The estimation of η_r is done on-the-fly, based on solid volume fraction (ϕ_{sol}) using the Thomas' expression (Eqn. 3.2).[120,121] Here, we assume that ϕ_{sol} takes into account the additional volume occupied by volumetrically expanding silicon particles.

$$\eta_r = 1 + 2.5 \cdot \phi_{sol} + 10.05 \cdot \phi_{sol}^2 \qquad \text{(Eqn 3.2)}$$

The electrochemistry taken into consideration is based on Butler-Volmer kinetics for the redox couple shown as follows:

$$Li \rightleftarrows Li^+ + e^- \qquad \text{(Eqn 3.3)}$$

$$Si_{0.26} + Li^+ + e^- \rightleftarrows LiSi_{0.26} \qquad \text{(Eqn 3.4)}$$

Eqn. 3.3 describes lithium metal oxidation at the anode and Eqn. 3.4 shows lithium insertion into silicon at the cathode. Although conventionally, the discharged silicon host is expressed as $Li_{15}Si_4$, for simplicity $LiSi_{0.26}$ (i.e. $LiSi_{4/15}$) is chosen so that stoichiometry of lithium (y in $Li_ySi_{0.26}$) at any point of discharge is between 0 and 1.[72] Fully discharged silicon particles ($LiSi_{0.26}$) reach an effective diameter 1.5 times greater on volume expansion.

The state of charge of the battery is obtained by tracking the potential difference between the electroactive silicon particles as cathode (E_c) and the lithium metal anode (E_a) as shown in Eqn. 3.5. Here, E_a is set to zero and the kinetics for the lithium oxidation reaction are assumed to be fast enough to consider negligible contribution to the activation overpotential. E_c is calculated based on a standard Nernst potential (Eqn. 3.6) where $E^0_{0.26}$ is the standard potential of silicon, y is the state of charge of silicon, F is the Faraday's constant, R is the gas constant, T refers to temperature, and n is the number of electrons involved. Here, the slope of the Nernst discharge is modified to correspond with experiments by Hamelet *et al.*[72] by incorporating a thermodynamic term containing the Margules constant (A):

$$E_{cell} = E_c - E_a \tag{Eqn 3.5}$$

$$E_c = E^0_{Si_{0.26}} + \frac{R \cdot T}{n \cdot F}\, ln\left(\frac{(1-y)}{y}\right) + \frac{R \cdot T}{n \cdot F} \cdot A \cdot (2y - 1) \; + \eta_c \tag{Eqn 3.6}$$

The activation overpotential (η_c) of lithium insertion reaction (Eqn. 3.4) is derived from the Butler-Volmer kinetic equation:

$$i_g = i_0 \cdot \left(exp\left(\frac{\alpha \cdot F \cdot \eta_c}{R \cdot T}\right) - exp\left(-\frac{(1-\alpha) \cdot F \cdot \eta_c}{R \cdot T}\right)\right) \tag{Eqn 3.7}$$

where the transfer coefficient (α) is taken as 0.5 such that the expression can be simplified to :

$$\eta_c = \; -\frac{R \cdot T}{0.5 \cdot n \cdot F} \cdot sinh^{-1}\left(\frac{i_g}{2 \cdot i_o}\right) \tag{Eqn 3.8}$$

The current density applied (i_g) is estimated by dividing the galvanostatic current by the surface area of electroactive silicon (A_{act}) obtained at a given time step. The surface area A_{act}, as shown in Eqn. 3.9, is an approximation of how much surface area of a given particle is exposed to the electrolyte. The particles, which are actually lower resolution spheres on the grid, are considered to have effective radius, r. Information from the environment of the particle on-the-fly is taken into account through k_f (Eqn. 3.10) which is a weighted sum of the

facets of the particle j that are blocked by other silicon particles ($A_{bSi,j}$) or other carbon particles ($A_{bC,j}$) and the number of facets are freely exposed to the electrolyte ($A_{f,j}$). As an example, constants ($k_1 = 0.2$) and ($k_2 = 0.5$) are assumed to describe the extent of interaction between particle surfaces, such that silicon particles do not tend to stick together as much as they would stick to carbon aggregates. Here the range for these constants is between 0 for no interaction and 1 for sticking. Surface roughness (R_{BET}), in Eqn. 3.11, is an important parameter to include experimental values of BET surface area (A_{BET}), which is made dimensionless by density (ρ) and radius (r):[122]

$$A_{act} = k_f \cdot R_{BET} \cdot 4\pi r^2 \qquad \text{(Eqn 3.9)}$$

$$k_f = \sum_{j=0}^{n_{actSi}} \left(\frac{A_{f,j} + k_1 \cdot A_{bSi,j} + k_2 \cdot A_{bC,j}}{A_{total}} \right) \qquad \text{(Eqn 3.10)}$$

$$R_{BET} = \frac{1}{3} \cdot A_{BET} \cdot \rho \cdot r \qquad \text{(Eqn 3.11)}$$

The exchange current density (i_o) as seen in (Eqn. 7) can be expressed as follows:

$$i_o = F \cdot K \cdot {c_{Li,el}}^{\alpha} \cdot {c_{Si}}^{\alpha} \cdot {c_{Li_xSi}}^{1-\alpha} \qquad \text{(Eqn 3.12)}$$

As a starting point, the reaction rate constant K in Eqn 3.12, was obtained from literature for crystalline silicon.[123] This equation takes into account concentration of lithium ion in the electrolyte ($c_{Li,el}$) as 1mM. It further incorporates volume expansion such that the volume increases 2.75 times, based on the state of charge (y). Concentration of silicon (c_{Si}) and lithium inserted silicon (c_{Li_xSi}) are expressed in terms of initial concentration of carbon ($c_{Si,in}$):

$${c_{Si}}^{\alpha} \cdot {c_{Li_xSi}}^{1-\alpha} = \frac{c_{Si,in} \cdot (1-y)^{1-\alpha} \cdot y^{\alpha}}{(1 + 1.75 \cdot y)} \qquad \text{(Eqn 3.13)}$$

At this stage, it is assumed that no mechanisms for irreversible loss of capacity are present in the system, *i.e.* electrons and lithium ions are only consumed by the silicon insertion reaction. Any other contribution to the potential drop arising from capacitive effects of carbon, resistance across carbon particle contacts in the network,

parasitic effects such as electrolyte degradation and lithium uptake by carbon, as well as cracking of silicon particles is ignored but can be introduced in the future. Resistance arising from lithium ion transport in the electrolyte is neglected under the low c-rate conditions in which batteries containing silicon are usually operated. It is assumed that lithium ions are readily available at the silicon-electrolyte interface and do no limit the insertion reaction shown in Eqn. 3.4.

3.2.2. Agent-Based Model Description

In this study, the many-body problem of SSRFB systems is taken into account explicitly, through the implementation of an Agent-Based Model (ABM) to capture mechanistic details. These are typically used to track collective motion of many entities or agents in economics, social studies and biology.[124–126] ABMs can also provide a platform for hybrid multiscale modeling and exploring different assumptions for a given theory.[124,125] However, for mechanistic models, experimental validation of results is known to be a significant challenge. These models have been criticized for lack of standardization, and while some attempts have been made to build mathematical formalism,[125,127] there is still no consensus as to how such models should be validated.[126] Despite these challenges, mechanistic insight can be vital to explore phenomena that standard models or experiments cannot capture.

For the SSRFB simulated in this study, the silicon and carbon particles are agents which are free to move around and possess properties like radius, volume, density, state of charge, electronic conductivity, lithium insertion capability, and information on the neighboring particles. Based on the particle dynamics, the number of events and time step can be scaled with a kMC engine described in the following section. The algorithm of this mechanistic model, summarized in Figure 3.2, is based on implementing the physics described in the previous section to the particles in discretized three dimensional space. The agents or particles are classified into two types, *i.e.* silicon and carbon, each having different sizes and electrochemical behavior. The empty cells on the grid, *i.e.* those between particles, are assumed to have lithium ion containing electrolyte necessary for discharge. Initially,

carbon and silicon particles occupy one and seven unit cells respectively, in order to generate a particle size difference which is computationally and experimentally viable. The silicon particles are designed by seven sub-particles occupying positions: (x, y, z) , (x+1, y, z) , (x, y+1, z) , (x, y, z+1) , (x-1, y, z) , (x, y-1, z) , (x, y, z-1). At the end of discharge, the silicon particle is expected to expand through the means of additional unit cells and become a cube. These shapes were chosen to obtain sphere-like symmetry at low resolution both before and after discharge. Particles with more intricate shapes or particle size distribution can potentially be included once computational speed and handling is enhanced. This initialization module is labeled as *1* in Figure 3.2, here, the user inputs like C-rate, temperature, electrolyte viscosity, lithium ion concentration, solid concentration, and surface area of materials, along with parameters relevant for the simulation like simulation box size, unit cell size, and particle shape.

The position of all the particles is generated by randomly positioning carbon and silicon over the discrete grid wherein the particle density is estimated by the solid fraction. The next two modules, namely particle motion and electrochemistry are said to be implemented simultaneously in terms of physical time and are labeled as *2* in Figure 3.2. Once initiated, the module for particle motion finds and updates available free cells in the vicinity of each particle to ascertain which direction the particles can move in. Based on viscosity and diffusion coefficient, the kinetic rates for motion of a given particle in a given direction, are obtained. The kMC engine helps choose an event at random and provides the time step. During this time step, it is assumed that simultaneous electrochemical discharge takes place. Under conditions of galvanostatic discharge and constant current, the time step provides the charge transferred to the system. Apart from identifying neighboring cells of particles, another time consuming computational effort is to identify percolating carbon networks and find electrochemically active silicon particles. The electric charge is then used to update the state of charge of the silicon particles and implement volume expansion. This expansion is expected to be visible in terms of addition of new unit cells to the particle shape if the available charge crosses a certain threshold. Carbon particles are assumed to participate only as electronic conductors, ferrying electrons from the current collector to the active material. The role of silicon as both electroactive material and electronic conductor is explored in the following chapters.

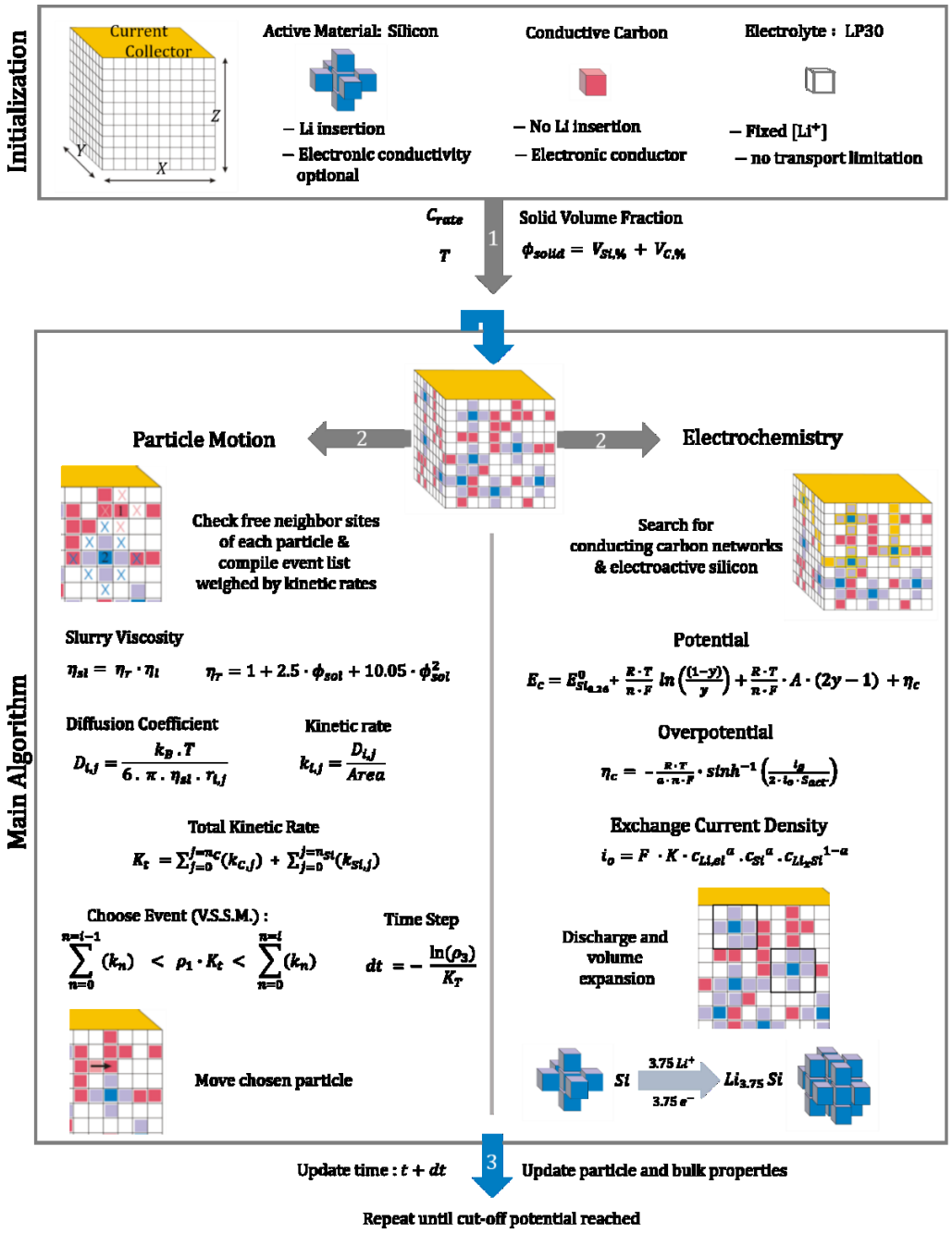

Figure 3.2. Simulation workflow describing the three main modules: (a) Initialization of simulation box; (b) Brownian motion using kMC-VSSM; (c) electrochemical phenomena for silicon discharge. Modules (b) and (c) are implemented till the potential calculated in (c) reaches a cut-off potential.

3.2.3 Kinetic Monte Carlo engine

Historically, spatial Monte Carlo (MC) techniques have been used for structure-property determination in condensed phases. For instance, to study a variety of phenomena at solid-liquid interfaces involving surfaces, defects and nanoparticles, and to study gas-phase-like transport, thermo-physics, magnetism, and mechanics.[128–136] MC methods were successfully applied beyond systems at equilibrium, to non-equilibrium systems in the 1970s-1980s.[137] However, since their predictive capabilities at that time were restricted by computational power and since they were not viewed as first principles method, their applicability was taken over by methods like Molecular Dynamics (MD) and atomic scale dynamic simulations. As computational power increased, so did the need to make even more accurate predictions, and it was realized that models like MD cannot handle phenomena across multiple time scales. With the added computational power, MC techniques became relevant again. Studies in biological systems, which have been a forerunner in application of complex system theory, also reported the use of MC methods to handle stochasticity in biological networks.[138–142] Recently, mechanistic models based on kMC have been proposed for various battery applications like Li-air and Li-S batteries[143–152]. Algorithms like variable step size method (VSSM) in kMC are promising as they are capable of tuning simulation time step based on the possible number of events within a given state of the system, making it suitable to address multi-scale and multi-phenomena problems. In this work, VSSM is used to choose an event from a weighted list of all possible particle displacements occurring in the module for particle motion, here the weights are based on the diffusion rate. The particle most likely to be selected by VSSM is the one that has small size and many empty neighboring cells.

Once the diffusion rates of all carbon (n_C) and silicon (n_{Si}) particles have been calculated, the weighted cumulative list of particle displacements can be obtained. The total diffusion rate (K_T), as shown in Eqn. 3.14, is taken as a sum of individual diffusion rates ($k_{i,j}$) of all particles where i denotes silicon (Si) or carbon (C) and j refers to the particle number:

$$K_T = \sum_{j=1}^{j=n_C}(k_{C,j}) + \sum_{j=1}^{j=n_{Si}}(k_{Si,j}) \quad \text{(Eqn 3.14)}$$

The VSSM algorithm typically proceeds by generating a random number (ρ_1) to pick an event within this weighted list (Eqn. 3.15). The m[th] particle is chosen to move within a time step calculated as shown in Eqn. 3.16, based on another random number:

$$\sum_{n=1}^{n=m}(k_n) \leq \rho_1 \cdot K_T < \sum_{n=1}^{n=m+1}(k_n) \quad \text{(Eqn 3.15)}$$

$$dt = \frac{ln(\rho_2)}{K_T} \quad \text{(Eqn 3.16)}$$

3.3. Model Initialization

The first studies were done based on as many experimentally relevant parameter values as possible, which are highlighted in Table 3.1. In correspondence with the publication by Hamelet *et al.*,[72] the slurry composition is taken to be 9 vol% of carbon and 14 vol% of silicon suspended in electrolyte.

Table 3.1. Parameters used in the simulations

Symbol	***Parameter***	***Material***	***Value***
T	*Temperature (K)*		290
$c_{Li,el}$	*Concentration* (mol/m^3)	*Lithium ion*	1×10^{-3}
η_l	*Viscosity* $(Kg/s.m)$	*LP30 electrolyte*	$5{,}03 \times 10^{-4}$
α	*Charge Transfer Coefficient*		0,5
K	*Reaction Constant*		1×10^{-10}
A	*Margules Constant*		$-9{,}8$
r	*Particle Radius (nm)*	*Carbon*	157
		Silicon	370
A_{BET}	*BET Surface Area* (m^2/Kg)	*Carbon*	$7{,}8 \times 10^5$
		Silicon	3×10^4

The simulation box is considered to have a depth of 10 unit cells and a square current collector top with an edge of 20 unit cells. The unit cell length is used to scale the simulation box without compromising on physically relevant parameters like volume fraction, therefore the unit cell is varied along the result sections and will be

specified. It is important to note that particle shapes for carbon and silicon are fixed to ensure the mesoscopic and mechanistic impact of particle size differences. For the results mentioned in this chapter, the unit cell is assumed to be 100 nm. The simulation box typically looks like Figure 3.3(a) where the blue particles represent silicon, red represent carbon, the empty void around the particles is assumed to consist of electrolyte containing lithium ions, and the top facet in brown represents the current collector providing electrons. This three dimensional visuals presented henceforth were generated using OVITO.[153]

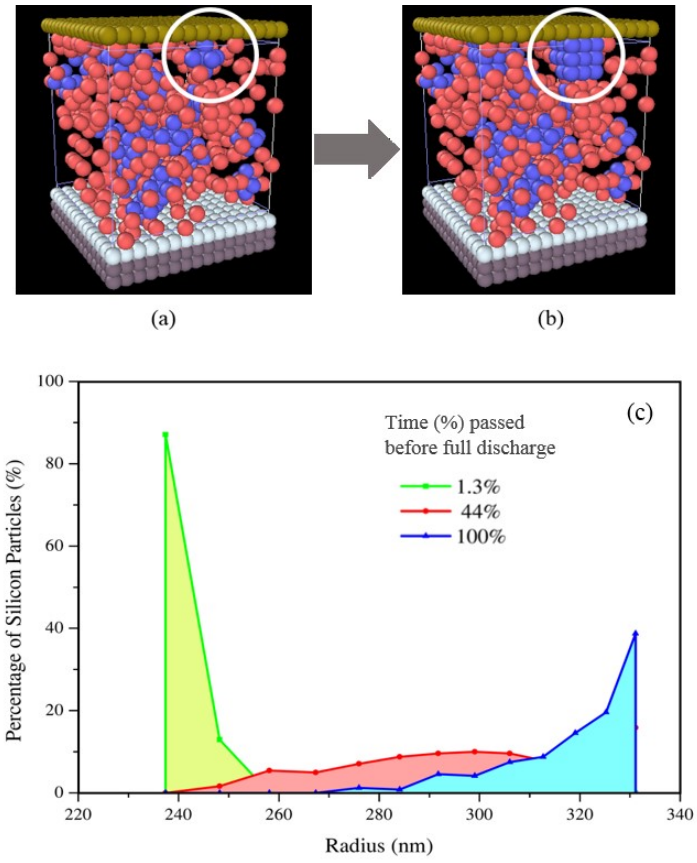

Figure 3.3. Simulation box containing slurry, (a) before and (b) after a silicon particle on the top right (in blue) experiences discharge. (c) An example showing particle size distribution of silicon along discharge.

The volume expansion of silicon particles on discharge can be seen in Figure 3.3(b). The results presented henceforth will be shown without the top and bottom faces for maximum visibility of the slurry mesostructure. The effect of volume expansion on silicon particle size distribution can be presented along time normalized to

percentages of total discharge time, regardless of final capacity, as in Figure 3.3(c). This tool can also help: (i) visualize the landscape of state of the charge of silicon particles, (ii) show how well the particle networks are constructed based on the rate of change of particle size distribution, (iii) the portion of silicon particles that were not fully discharged, and (iv) provide a means to capture local viscosity effects in the future. The radius used here is effective radius which is calculated by assuming that the sum of the volume of all individual silicon sub-particles on the three-dimensional grid corresponds to the volume of a sphere. It can be highly advantageous to be able to track the behavior of every parameter used in the theoretical description of the model. This helps to form more accurate hypotheses to explain a simulated trend regardless of system complexity.

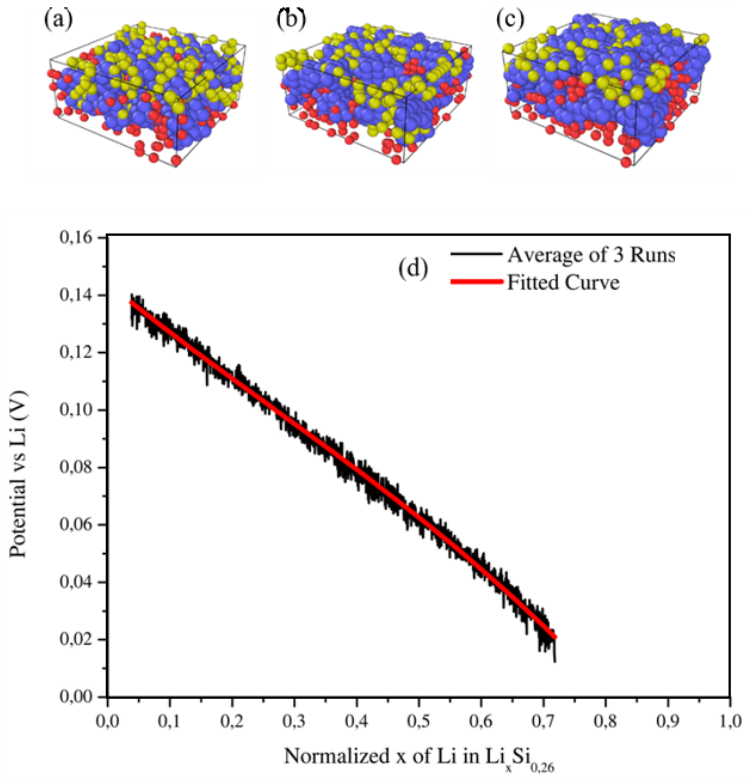

Figure 3.4. Snapshots of three dimensional visualization of the slurry with at: (a) beginning of simulation, (b) half discharge, and (c) full discharge; (d) average of three simulation runs (in black) and the final discharged curve obtained as a fitted cubic polynomial (in red). The current collector on the top has been removed for clarity.

To demonstrate how an electrochemical discharge curve is obtained, C-rate of C/20 was taken and for this particular case, the time steps obtained from VSSM were predominantly within the range of 10^{-1}-10^{-3} seconds and the total physically relevant time of battery discharge was 12 h. The discharge can be visualized in 3D as shown in Figure 3.4 (a)-(c), where the electronically conducting carbon particles wired to the current collector are shown in yellow. The silicon particles in blue visibly increase in volume along the discharge. Typically, a single simulation run produces a discharge curve with fluctuations due to the discrete nature of kMC (Figure 3.4 (d)). In order to produce statistical trends for all parameters, for each case, three simulations are run, averaged, and the resultant discharge curve is fitted either with a cubic polynomial function or a power law, to show its mean characteristic.

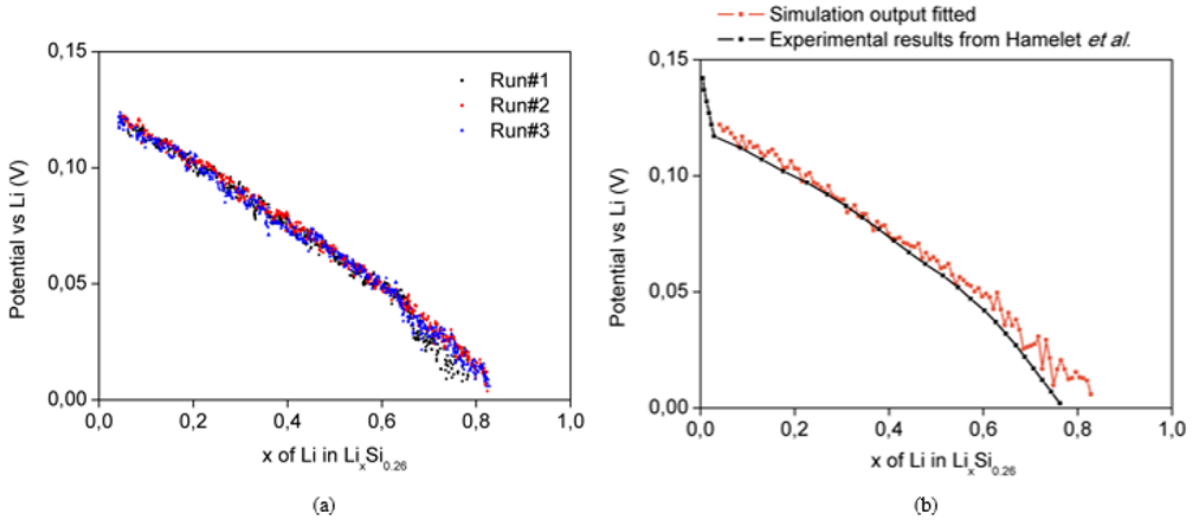

Figure 3.5 (a) Scatter plot for three sample simulations and (b) average for three runs is intrapolated to create an average curve to show its inherent stochasticity.

Reaction constant and Margules constant are the only parameters fitted to obtain experimentally relevant results, additionally, the starting value for the reaction constant was taken from literature and adjusted. An experimental discharge curve from Hamelet *et al.*[72] was used as reference but a good fit would only be possible if an extensive experimental parameter sensitivity study was available. All other parameters like the BET surface

area for silicon, viscosity of electrolyte, particle size, and standard potential of silicon were taken from experimental studies. This degree of pseudo-quantification is suitable for a first attempt where the priority is to study the features and the nature of the model itself. For this case, C-rate corresponding to the experimental data was chosen, *i.e.* C/4, the average of three simulation runs (Figure 3.5(a)) is taken and intrapolated (Figure 3.5(b)) in order to clearly show the stochasticity. While the curvature of the discharge curve is not accurately reproduced, such a simplified electrochemical model is not expected to provide a very precise fit. Over-fitting by introducing additional fitting parameters is not of interest for this mechanistic model.

In line with more continuum methods, it can be possible to convert various metrics like electronic charge uptake of particles into heat maps, an example of which is shown in Figure 3.6. The heat map here is prepared by projecting all particles on to an x-z plane, clearly demonstrating how the particles close to the current collector are the most discharged. While this is just to show the capability of the results obtained from the model, such heat maps can be made more accurate with respect to the continuum assumption when larger slurry volumes are simulated in the future.

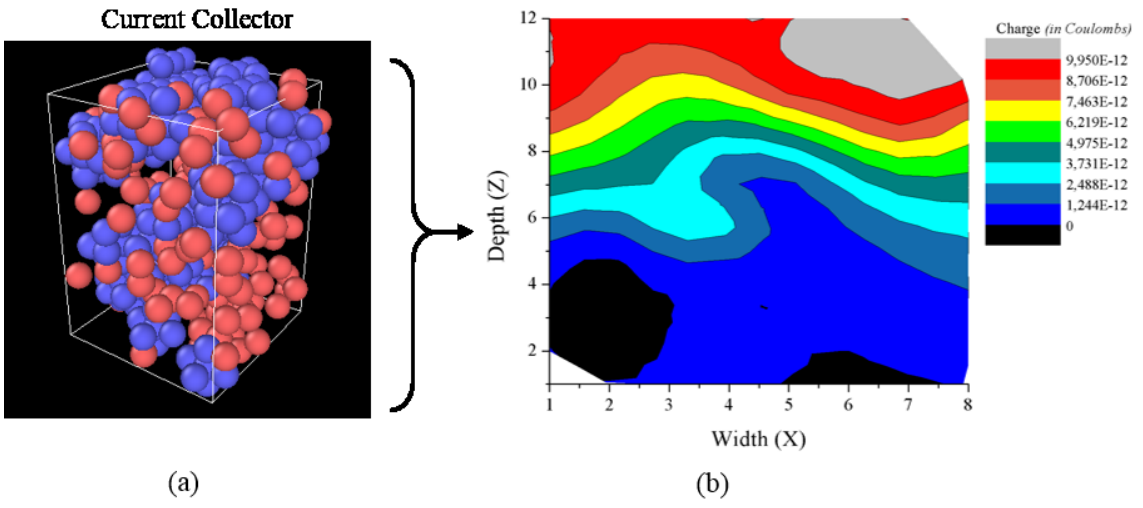

Figure 3.6. An example to show how a simulation box shown in (a) can be represented as a heat map in (b), to demonstrate state of charge of silicon particles.

3.4. Summary

This chapter begins with a discussion pertaining to sources of complexity in SSRFBs, which is said to arise from numerous competing phenomena across scales and especially due to many-body interactions and collective particle behavior at mesoscale. Popular modeling tools, like MD, do not allow the theoretical freedom necessary for causal discovery which is vital for SSRFBs. As an example to build this model, an experimental study based on a slurry containing silicon and carbon in organic electrolyte, is taken from literature.

The mechanistic model, described in this chapter, is particularly designed to provide an open and adaptive theoretical framework. It consists of an ABM developed in-house in Python that simulates physically relevant time and implements particle motion through a kMC engine. It takes into account parameters like diffusion coefficient, viscosity, particle radius, volume fraction of solid, to generate kinetic rates for motion. The electrochemical discharge of silicon versus lithium metal anode is modeled using Butler-Volmer kinetics wherein the exchange current density is modified to take into account volume expansion of silicon. A schematic of the algorithm is provided to give an overall picture of how the simulation takes place on the three dimensional grid.

Some basic results were produced with the objective of calibrating the algorithm and adjusting the input parameters to produce physically relevant results, in context to experimental literature. Stochasticity in the discharge curves was observed as an inherent output feature of the model. It was dealt with by running multiple simulations for the same conditions and considering the average. The volume expansion of silicon particles is evident from the three dimensional visualization of the results using the software OVITO.

The next chapter is designed to provide insight on the method itself so that idea simulating conditions can be obtained. This following chapter provides physically relevant results that can provide qualitative explanations for various, seemingly contradictory studies in experiment.

Chapter 4

Insights on the Method

4.1. Introduction

This chapter provides an assessment of the modeling method by highlighting its abilities and limitations. Since studies of this genre are rare, even more so in the discipline of materials for energy applications, significant effort was needed to establish sound basis and justification for the method. Furthermore, it was challenging to calibrate the model to obtain experimentally relevant results which will be presented in the following chapter.

The following sections present parameter sensitivity analysis (PSA) performed to understand the evolution of parameters as well as effectiveness of the method. In a system dealing with multiple parameter interdependencies, having access to only a few simulation results fitted to experimental results is not enough. PSA is instrumental for model configuration and finding suitable input parameters which may not be otherwise available.

The use of on-lattice Agent Based Model (ABM) in conjunction to kinetic Monte Carlo (kMC) brings a stochastic nature to the output of the simulations. This is an added challenge for performing PSA, where perturbation are made to input values to see the impact on the output. Studies done in this context indicate that (i) large step sizes in input parameters are useful to counteract the deleterious effect of stochastic fluctuations and that (ii) statistically reliable sensitivity of output from large perturbations is more valuable than unreliable sensitivities arising from small perturbations.[154] These aspects have been taken into account for data generation in the following sections. The use of graph theory to handle complexity is further proposed as a perspective.

4.2. Local Parameter Sensitivity Analysis

After the adjusting the input parameters to experimentally relevant values, as shown in the previous chapter, a local PSA was performed on the size of the simulation box, C-rate, and volume fraction of carbon particles, by adding small perturbations to these parameters. This is particularly important to see whether the results

are physically feasible and reasonable under these perturbations. In the presence of anomalies, it is necessary to either identify bugs in the code or modify the algorithm prior to a global, wider scale PSA.

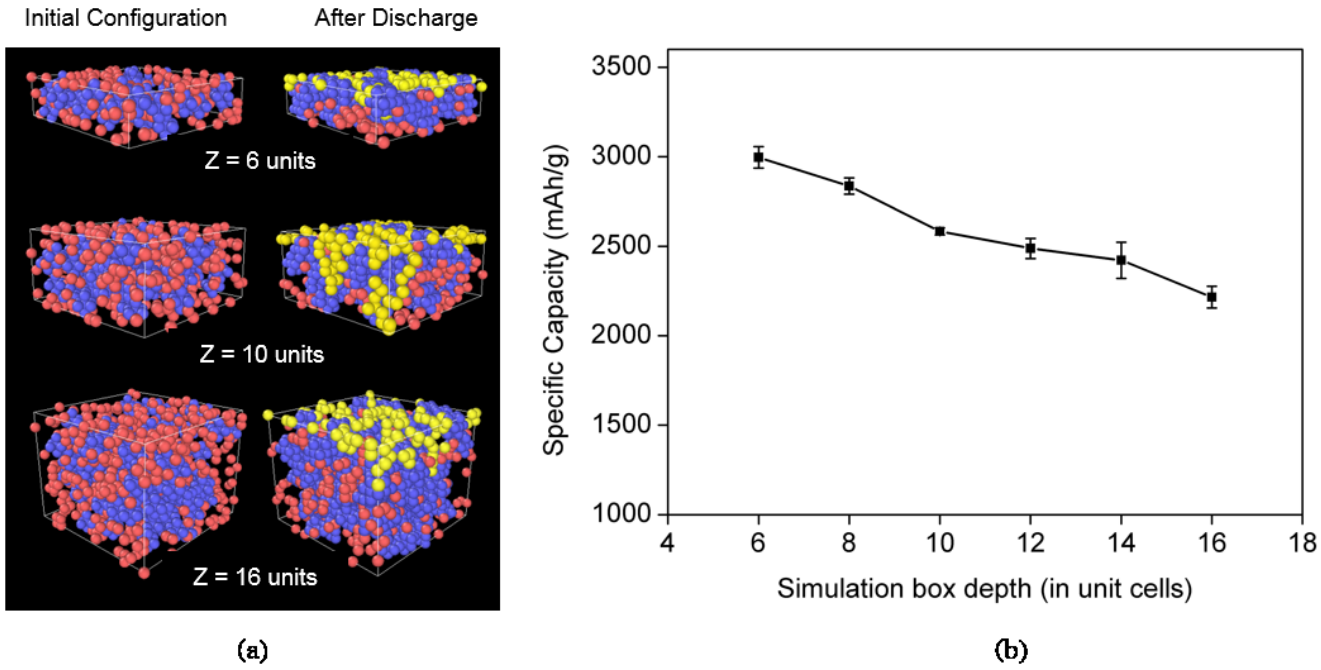

Figure 4.1. The impact of depth of simulation box on discharge capacity where (a) shows three example cases chosen from the trends shown in (b). The depth or Z is varied from 6 to 16 units in steps of 4 units.

With the size of the current collector on top, fixed, the impact of simulation box depth on specific capacity, at the end of discharge, is shown in Figure 4.1, at a C-rate of C/20. The slurry in contact with the current collector is chosen as a representative system assuming that conditions needed to achieve good conductive networks in this region is essential for any conductivity to be seen in the bulk. Furthermore, the solid concentrations needed to form networks at this scale can be roughly representative of bulk behavior. The heights of simulation boxes or the depth, in direction Z, are varied from 6, 8, 10, 12, 14, to 16 unit cells and the capacities are shown in Figure 4.1(b). The cases for 6, 10, and 14 units are also visualized in Figure 4.1(b). The capacity is seen to decrease as the depth is increased. Regardless of how good the carbon networks are, it is evident that silicon particles closer to the current collector can easily discharge due to higher chances of encountering an electronically conducting carbon

particle. Similarly, in smaller simulation boxes, it is easier for silicon particles at the bottom to discharge. The error bars in Figure 4.1(a) do not show a constant trend, suggesting that there may be more factors worth exploring.

For a composition with 9 v% carbon, 14 v% silicon, in a simulation box of dimensions 20 × 20 × 10 units, the specific capacity is also studied as a function of C-rates, 2C, C, C/5, C/10, and C/20. Figure 4.2 shows how the capacity is seen to decline at higher or faster C-rates. This trend is expected to result from both, the physical time for which the discharge occurs and the applied current density which manifests in influencing the potential through the activation overpotential. Given that lithium ion transport is not calculated in this model, slower C-rates are preferable under both simulation and experimental conditions.

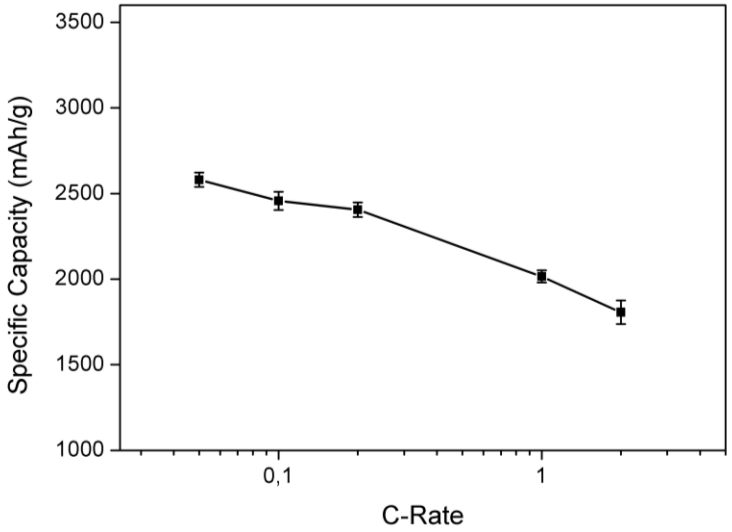

Figure 4.2. The impact of C-rates 2C, C, C/5, C/10, and C/20, on specific capacity.

With the aforementioned reference system, *i.e.* 14 v% silicon, in a box of dimensions 20 × 20 × 10 units, at C/20, a detailed study of the impact of carbon fraction on the specific capacity is presented in Figure 4.3. The carbon fractions considered range from 3 v% to 17 v% in steps of 2 v%. The 3D simulation boxes obtained at the end of discharge are shown in Figure 4.3 (a)-(h). The sensitivity of discharge capacity to carbon content is shown in Figure 4.3 (i). According to nomenclature from Medalia *et al.*,[155] typically DC conductivity with carbon black is seen to vary as a sigmoid-like curve shown in Figure 4.3 (j), wherein the percolation threshold is known as the

starting point for the linear part labeled *B i.e.* the percolation region. To avoid confusion, the region labeled *C* is associated with conductive chains of carbon particles that span throughout the volume of the electrode and represents a threshold or saturation for conductivity of slurry.[155]

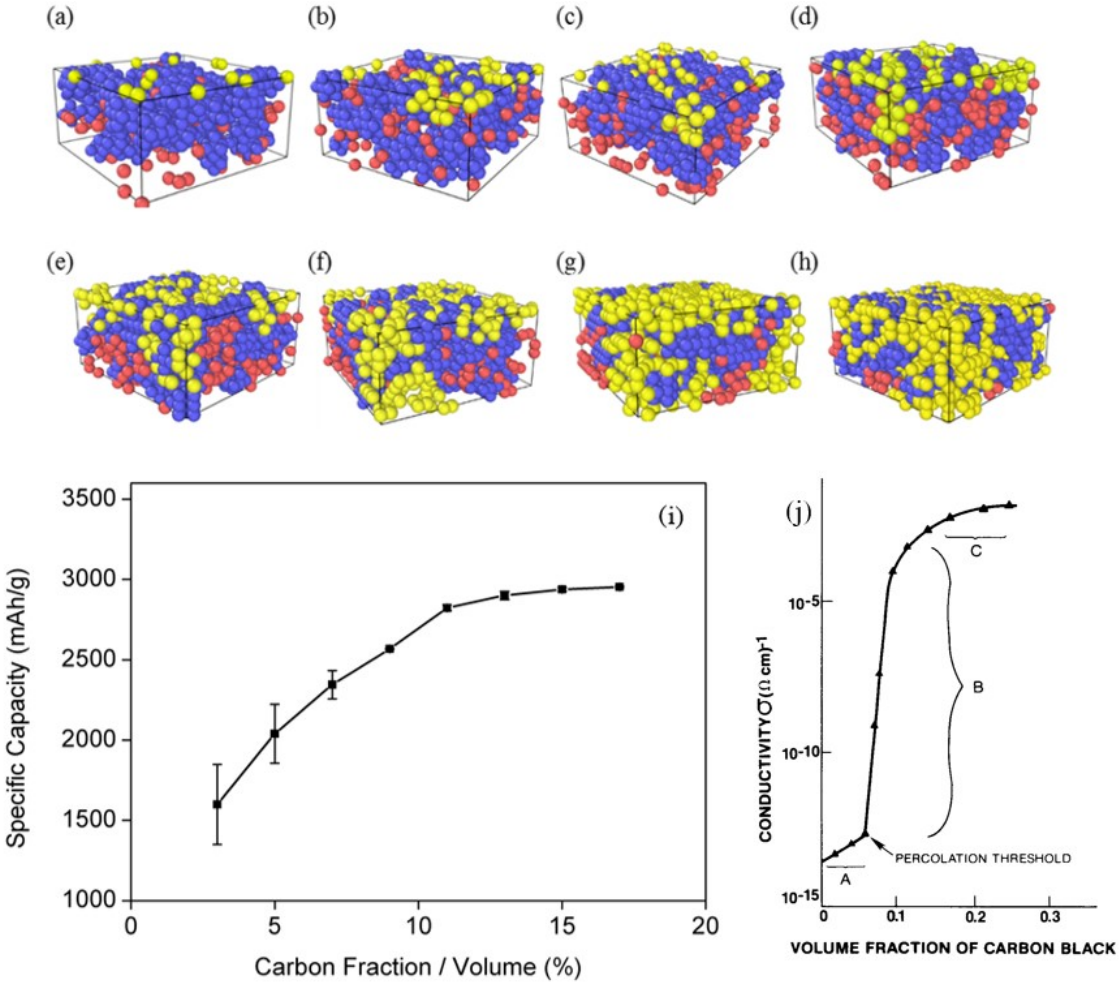

Figure 4.3. Cases simulated to study sensitivity of discharge capacity to carbon content which is varied from 3 v% to 17 v% in steps of 2 v%. (a)-(h) show simulation boxes at the end of discharge, (i) shows the overall trend of capacity and (j) provides a reference from literature by Medalia et al.[155] indicating the important features of a composition versus conductivity curve.

Based such nomenclature, it can be said that in Figure 4.3 (i) the region below 11 v% carbon roughly corresponds to the percolation region and that at 11 v% and beyond, the conductivity is said to have saturated. It

can be said that beyond this composition, carbon networks are always available and the specific capacity is no longer a function of the number of carbon particles. The error bar gradually decreases as carbon fraction is increased, this can be explained by: (i) small system size, (ii) decreasing sensitivity of kMC to the initial particle configuration in slurry, (iii) reduced diffusion rate, and (iv) decrease in importance of the role of each carbon particle in the carbon network. The mechanistic nature of the model provides more diagnostic tools as shown in Figure 4.4 and Figure 4.5, to analyze the impact of carbon fraction in greater detail, two of which are discussed.

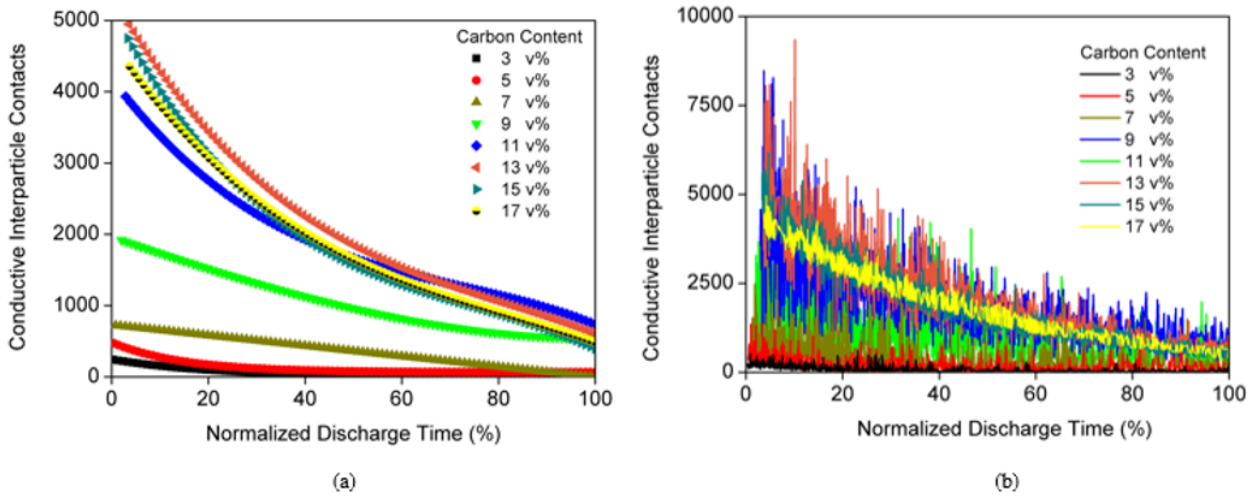

Figure 4.4 (a) The impact of carbon fraction (3-17 v%) on the evolution of average number of particle contacts within a conductive network, along normalized time of discharge and (b) raw data.

The nature of the particle assembly (Figure 4.3 (a)-(h)) can be quantified based on the number of inter-particle contacts in a carbon network, offering a means to visualize and analyze the extent of conductivity. It is evident that within the range 7-11 v% carbon, there is a significant jump in the number of conducting particle contacts, beyond which the number saturates. This observation clearly demonstrates the existence of a percolation region and conductivity saturation as reported by Medalia *et al.*[155] and provides a more precise range than Figure 4.3 (i). The raw data shown in Figure 4.4 (b) provides additional insight, for instance, the amount of fluctuation is seen to increase with carbon fraction and then decrease beyond the plateau. The most significant data fluctuation is observed between 9-13 v% carbon, and corresponds to the transition between region *B* and *C* in

Figure 4.3 (j). The fluctuations can be said to arise from a number of competing effects: (i) increase in carbon content resulting in larger conductivity networks in the percolation region, (ii) larger particle populations suppressing particle diffusion, and (iii) higher dependence on initial configuration below conductivity saturation because each carbon particle plays an important role in maintaining conductive networks. Beyond 15 v% of carbon, the fluctuations are drastically reduced, indicating that the conductive carbon network is stable and that particle diffusion also slows down, suppressing stochasticity in the data. Exploring the evolution of the number of silicon particles in contact with conductive networks, as shown in Figure 4.5, can provide support for these claims.

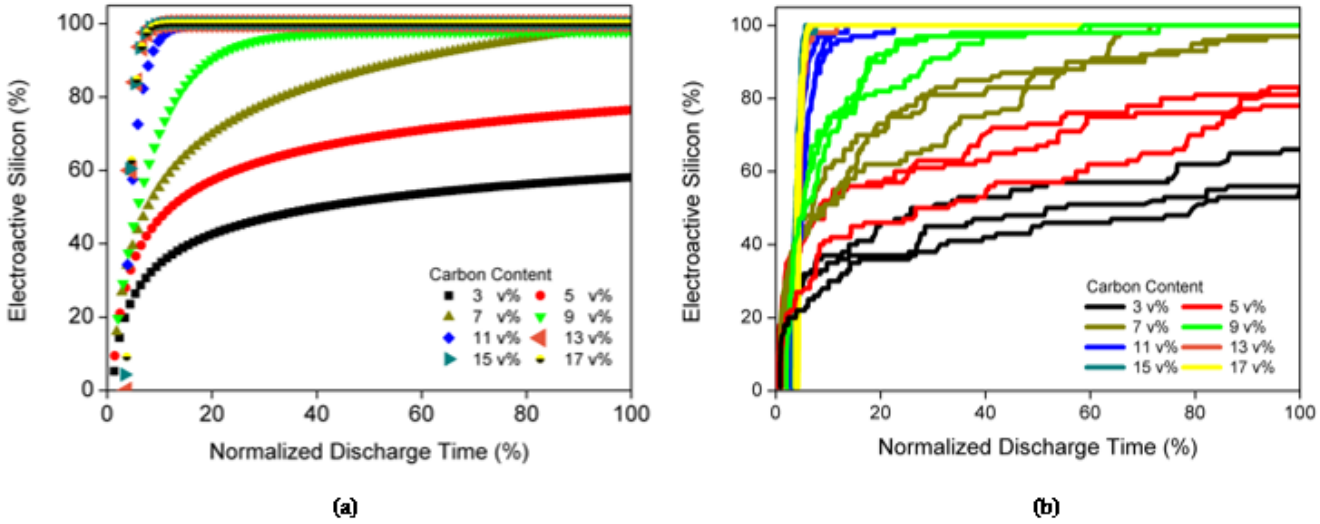

Figure 4.5 (a) The impact of carbon fraction (3-17 v%) on the fraction of silicon particles connected to conductive networks and its evolution in time. (b) Raw data for the same, showing the dispersion of each case.

The transition seen in Figure 4.4 (a) over 7-11 v% is evident in Figure 4.5 (a). For carbon fractions at and below 7 v%, the power-law type trend has an upward slope and does not attain 100% silicon content, indicating that some silicon particles are out of reach. For carbon fractions at and above 11 v%, all the silicon particles are very rapidly connected to conductive networks and corroborates with the conductivity threshold previously observed. The raw data in Figure 4.5 (b) shows how the dispersion of data for each case decreases as the carbon

content approaches 11 v%. For lower carbon content, the large variation between the individual runs indicates the high sensitivity of the collective particle behavior to the initial configuration of particles in the slurry.

4.3. Data Generation for Parameter Sensitivity Analysis

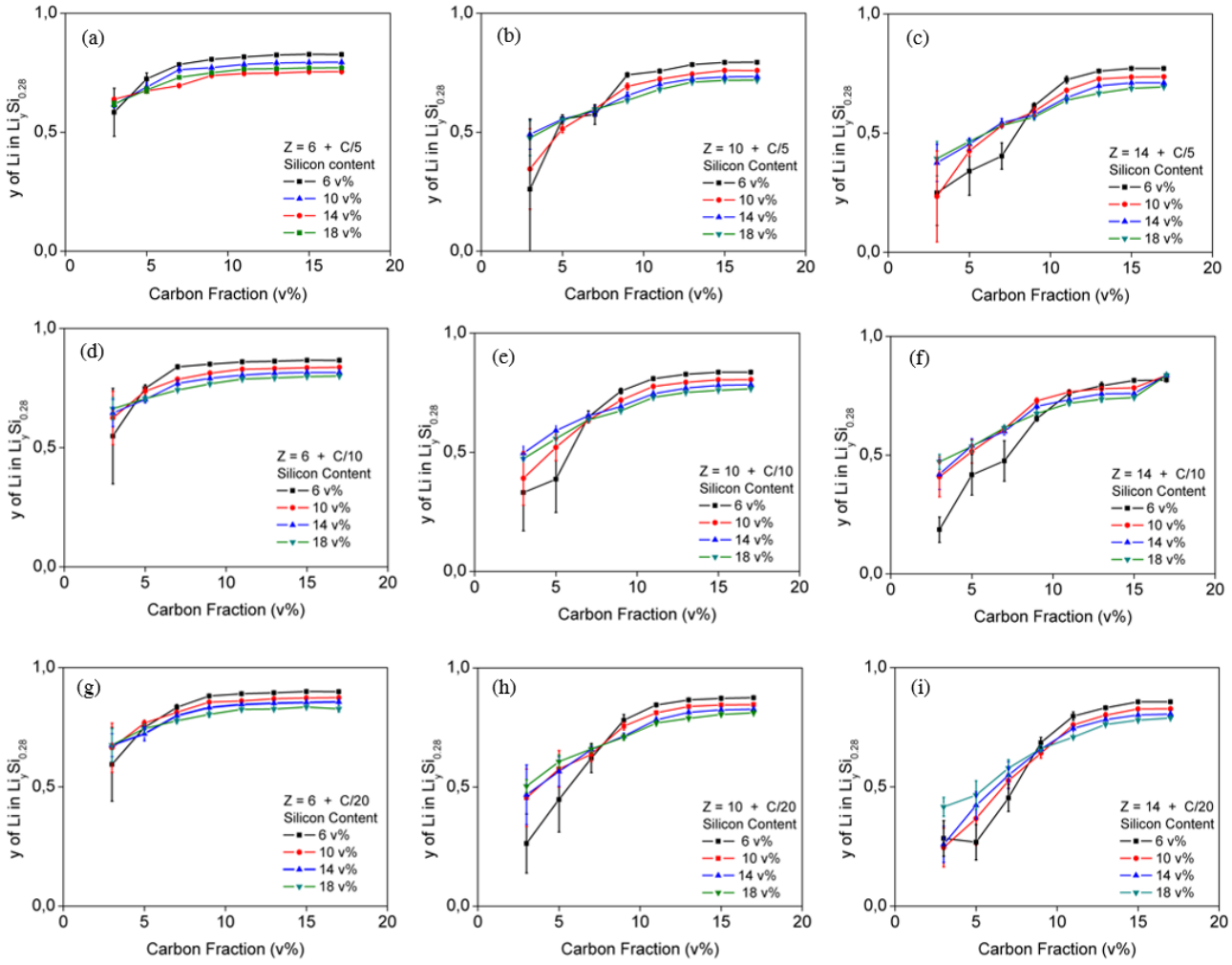

Figure 4.6. Sensitivity to four parameters is simultaneously studied in these 288 cases where simulation box depth (Z) is varied from 6, 10 to 14 units, at C-rates C/5, C/10, and C/20, silicon is varied in increments of 4 % between 6-18 v% and carbon in increments of 2 % between 3-17 v%.

A larger sensitivity study with 288 cases was simulated by the first generation of the in-house Python code developed and the curves are shown in Figure 4.6. The simulation box size was varied over Z = 6 units, 10 units

and 14 units with the unit cell of length 100 nm. The C-rates C/5, C/10, and C/20 were chosen to avoid ionic transport limitations. In these simulations, since the size of the simulation box is fixed, it is difficult to isolate effects of solid-liquid ratio variation from silicon-carbon ratio variation. While this can be addressed in the future, worthwhile mechanistic information can still be obtained from this version of the model. Silicon volume fraction is varied between 6-18 v% with increments of 4 v% and carbon volume fraction between 3-17 v% in steps of 2 v%. Each case was simulated five times for reproducibility and averaged, amounting to a total of 1440 simulation runs. The nature of the trend is similar for all case, as it consists of a percolation region, a conductivity threshold, and a saturation region. Drop in capacity is observed for faster C-rates and for increase in silicon volume fraction.

These results are further analyzed in the following subsections to highlight features of the model. This data also identifies the complexity that manifests within a system where numerous forces impact the final outcome. Thus parameter sensitivity analysis where multiple parameters are simultaneously varied, offers a useful means to study the system from many facets.

4.3.1. Simultaneous Multi-Parameter Impact

The data from the 288 cases is presented in terms of sensitivity of the conductivity threshold (C_T) towards perturbations in Z, C-rate, silicon content, and carbon content. Since parameter sensitivity depends on the value of the parameter in question, sensitivity is reported in context of a nominal (reference) value. For instance, the nominal value for the simulation box depth Z is taken as 10 units with perturbations of $\pm$ 4 units, and for C-rate it is taken as C/10 with perturbations of $\pm$ C/10 to obtain C/5 and C/20. For silicon content, two nominal values were chosen, 10 v% and 14 v%, each with perturbations of $\pm$4 v%. The sensitivity index ($S_+ \; or \; S_-$) is calculated based on literature,[156] where the function f provides the output of the model, n indicates the nominal value and Δp denotes the perturbation (Eqn. 2). In this study the sensitivities are is represented as a sum (S) of both sensitivity

indices (S_+ *or* S_-) as in Eqn. 1 to condense the amount of data, thereby the index is scaled to a maximum of 2. However it is important to keep in mind that the individual sensitivity indices may be different.

$$S(n \pm \Delta p) = S_+(n + \Delta p) + S_-(n - \Delta p) \quad \text{(Eqn 1)}$$

$$S(n \pm \Delta p) = \left|\frac{f(n+\Delta p)-f(n)}{\Delta p/n}\right| + \left|\frac{f(n)-f(n-\Delta p)}{\Delta p/n}\right| \quad \text{(Eqn 2)}$$

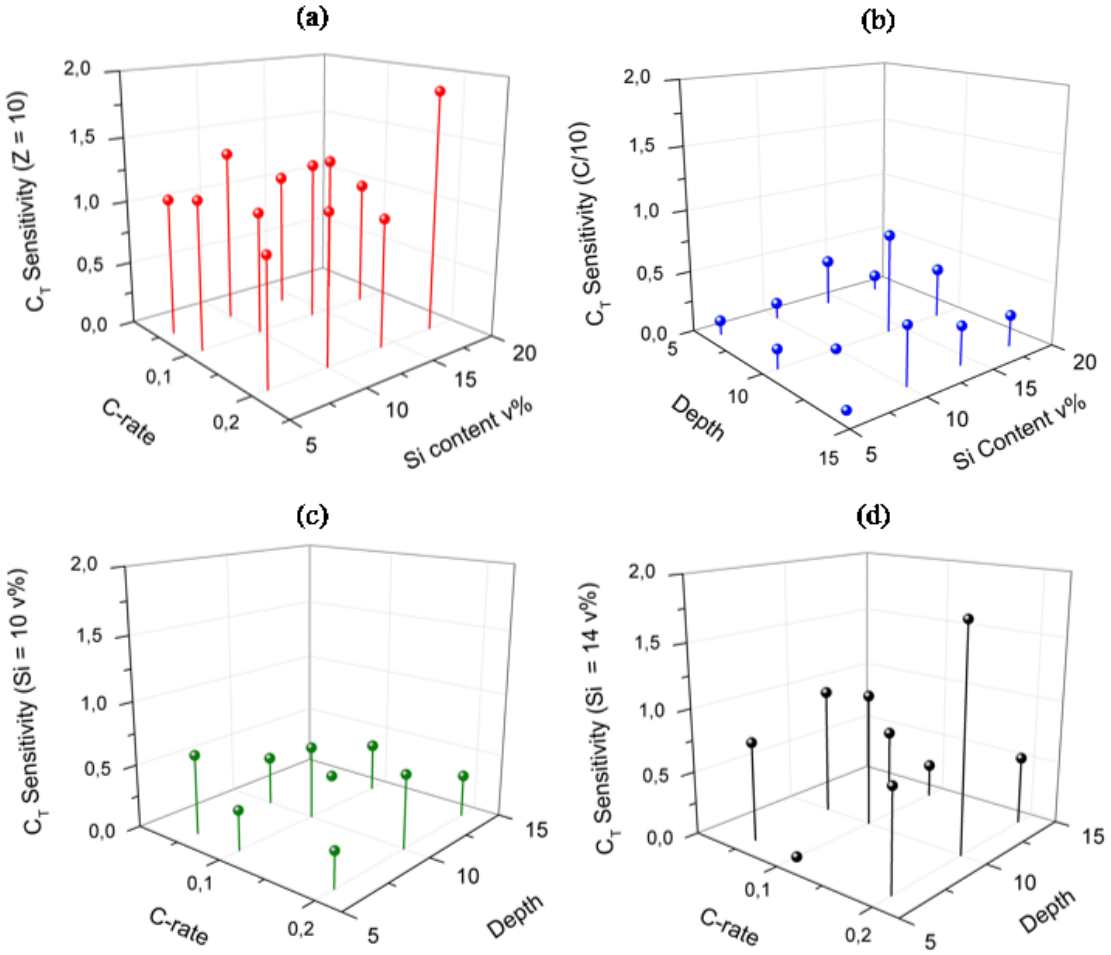

Figure 4.7. Sensitivities of threshold of conductivity (C_T) towards (a) simulation box depth at Z = 10 units with perturbations ± 4 units, (b) C-rate ($C/5$, $C/10$, $C/20$), and silicon content at (c) Si = 10 v% ± 4 v% and (d) Si = 14 v% ± 4 v%

The sensitivities are compiled and are presented in 3D plots in Figure 4.7 (a)-(d). The sensitivity for $C_T(Z = 10 \pm 4\ units)$ in Figure 4.7 (a) is shown to be most significant, *i.e.* perturbations in depth cause a big impact on the conductivity threshold for various C-rates and silicon fractions. Sensitivity for $C_T(C_{rate} = C/5, C/10, C/20)$ in Figure 4.7 (b) suggests that the impact of changing the C-rate is generally less and is seen at higher silicon content for all Z considered. When considering sensitivity of the threshold to silicon content, it is evident that the nominal value has an impact, *i.e.* sensitivity for $C_T(Si = 10 \pm 4\ v\%)$ is less significant than for $C_T(Si\ 14 \pm 4\ v\%)$. The results in Figure 4.7 provide a means to quantify the degree of non-intuitiveness of the system and provide a more tangible picture of complexity.

4.3.2 Efficiency and Accuracy of the Model

The data from the 288 cases can be processed in terms of the error bar and time taken for the simulations to run, to assess the accuracy and efficiency of the algorithm used. The trends are studied in terms of solid content to normalize the compositions but since each curve consists of a fixed silicon fraction, any changes in solid content indicate changes in carbon content. As an example, Figure 4.8 shows results for the simulations done at C/10. The accuracy of the model is studied in terms of the standard deviation of the capacity at the end of discharge for each of the 5 runs for reproducibility and is shown in Figure 4.8 (a). In general, increasing carbon content results in an overall increasing accuracy at all simulation depths studied, except for very high silicon content (18 v%) in a small simulation box (Z = 6 units). Furthermore, accuracy is shown to fluctuate more significantly for Z = 6 than Z = 10 or Z = 14 units, suggesting large sensitivity to initial configuration and highly restricted particle motion. The presence of carbon particles is expected to increase reproducibility of the simulations since they are more mobile due to small size and do not experience any volume changes. The accuracy of this model can thus be dynamic and not only is worth identifying the conditions under which the results generated are more reliable, this analysis can also provide mechanistic information.

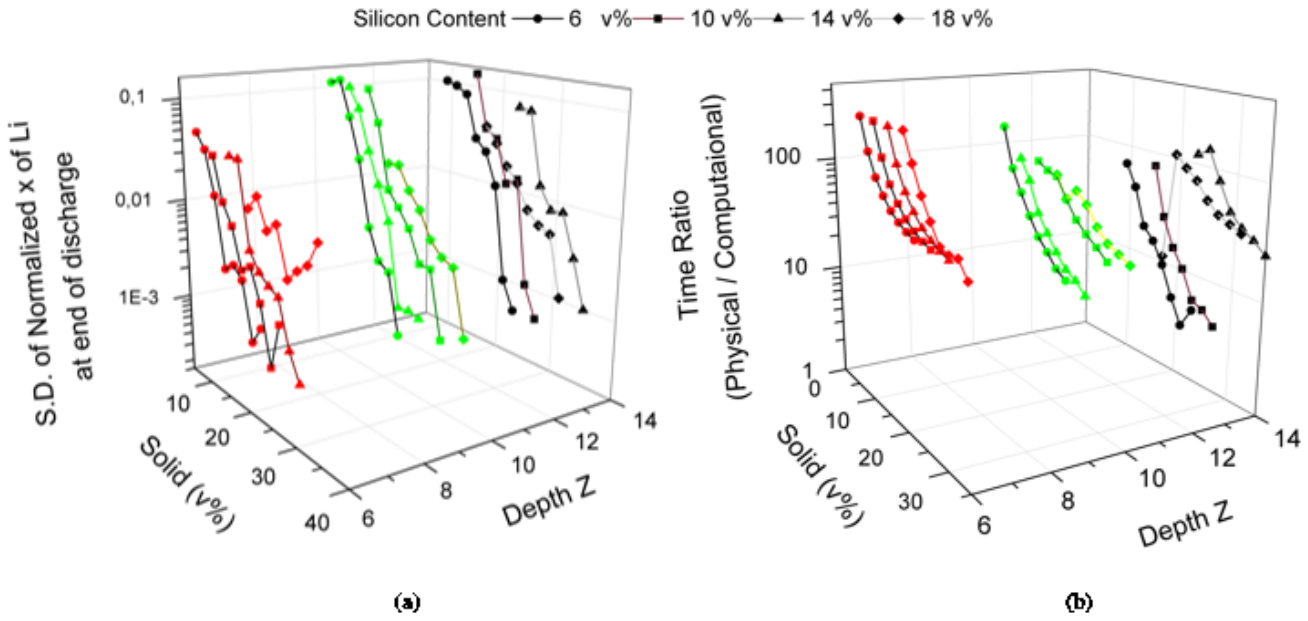

Figure 4.8. Studying the model algorithm in terms of (a) accuracy, by considering standard deviation of capacities attained for reproducibility runs and (b) efficiency, by considering the ratio of physical time simulated versus computational time taken by the simulation.

The efficiency of the model is depicted in Figure 4.8 (b) in terms of the ratio of physical time taken for discharge in the simulation versus the computational time taken for the simulation to run. Here, larger is the time ratio, more efficient is the model. Increase in depth is shown to decrease efficiency regardless of silicon content, this may arise from the larger population of the particles and consequently increased computational load. It can be concluded that higher accuracy in results is obtained at the cost of lower efficiency of the model.

4.3.3 Finite Size Effects

The aforementioned observations lead to question whether discreteness can have degrees, *i.e.* the physical resolution in a simulation can lie on a spectrum between continuum and discrete. As observed in the state of the art for modeling work, the concept of degree of discreteness drives the creation of new models for SSRFBs.

In our study, the overall electrode capacity is obtained from individual capacities of every silicon particle. Consequently, silicon's ability to discharge depends on carbon networks that have access to electrons. Furthermore, the finite package of electrons provided to the silicon is determined by the time step, which is estimated from total kinetic rate under the variable step size method (VSSM) of the kMC framework. The individual event rates arise from diffusion coefficients, which are calculated through the Stoke-Einstein equation and depend on particle radii and viscosity. Finally, viscosity, through the Thomas' empirical expression, depends on volume fraction or total volume of particles, and eventually on particle radii again.[119,121] Thus, it was found that time step and degree of discreteness of capacity depended heavily on the way particle radii were captured. A comprise was implemented to reduce the size of the error bar while still maintaining mechanistic detail on the three dimensional grid. For the sake of simplicity, at the initial stages of gauging the global and local behavior of the model in terms of physics, the degree of discreteness is minimized and only three runs for reproducibility are implemented instead of five. Additionally, the previously observed sensitivity of the conductivity threshold towards depth is expected to arise from two effects: (i) physically relevant phenomena and (ii) finite size effects from the discrete model. With the degree of discreteness minimized, the finite size effects can further be isolated in terms of total system size.

Another study, highlighted in Figure 4.9 shows the impact of increasing the slurry depth. Here, the unit length taken is around 300 nm and depth is varied from 6 to 26 units in steps of 4 units, with only three runs for reproducibility; amounting to 120 simulations. Excluding the first case which may be too shallow for silicon particles, the nature of the capacity-composition trend does not change significantly on increasing depth. The sigmoid-like nature of the curve becomes more evident at Z above 10 units, the linear percolation region sharpens between carbon fractions 9-13 v%, and the different curves are nearly superimposable at 11 v% carbon. This suggests that the larger simulation boxes would provide a more uniform environment in terms of particle density throughout the depth and allow results to converge. For immediate purposes, a box depth of 20 units is suitable, thus rendering the simulation box a cuboid.

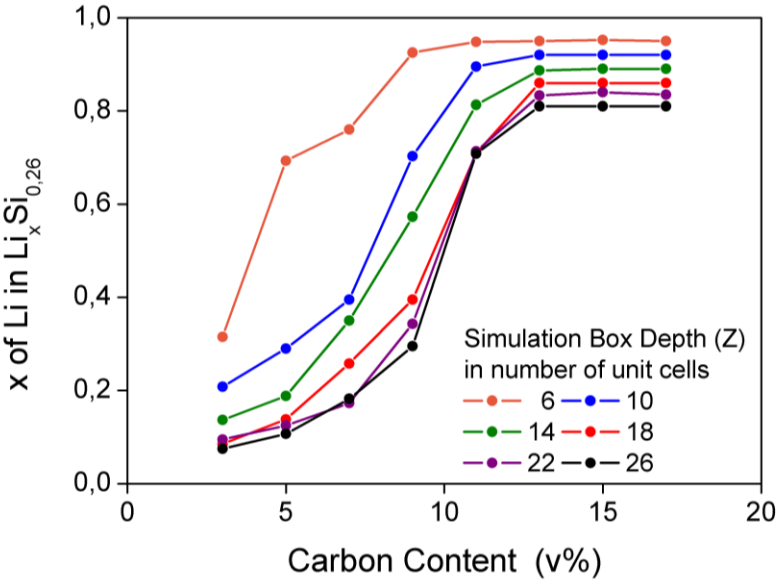

Figure 4.9. Sensitivity study with slurry depths varying from 6 units to 26 units in steps of 4 units, to minimize finite size effects.

4.4. Perspective use of graph theory

Based on the discussion in section 4.3.3 which shows how the intricacies of numerous parameters and their interdependence can ripple across the theoretical framework, and to ensure the adaptive, self-correcting nature of the model, it is relevant to create a causal flow systematically. For such a new and multidisciplinary battery system, significant challenges lie in building the first causal flow diagram[157] which is formally referred to as model specification.[158] Causal discovery is usually based on probabilistic methods employed in graphical modeling approaches like Bayesian Networks (BN) or Structural Equation Models (SEM). It is challenging to build a theoretical framework with very high degree of flexibility in a mathematically rigorous way. Typically, when there is confidence in the basic structure of a causal network, the Bayesian approach is applied to fine tune weightage between relationships and update knowledge in the light of new information. This approach belongs to one of the many schools of artificial intelligence, however, since there are many unknown relationships, both the relationships and the weights are subject to change, rendering the Bayesian network unrestricted and non-standard.

While this raises the question of what can be achieved by an unrestricted causal network, it is evident that it is a necessary step at this juncture. This thesis work uses PSA[156,159] to introduce rigor to studying an unrestricted network. After a causal flow is established with certainty, the Bayesian approach can be systematically applied. The present parameter sensitivities can lay the groundwork for application of more established graph theory methods wherein conditional probabilities, correlations, and covariance structures can be employed and backed up by appropriately obtained experimental datasets.

BNs and SEMs combine information of cause and effect with empirical data to provide a quantitative description of parameter relationships.[160] However, for many complex systems like those seen in economic and social sciences, most of the established modeling frameworks and procedures are ruled out. For instance, BNs have highly advanced tools to generate new knowledge from prior knowledge, but necessitate working with Directed Acyclic Graphs (DAGs). The following paragraphs briefly describe some basics of graph theory used in this work. A node is considered as a parameter or entity which undergoes evolution during the simulation. Graphs contain edges, *i.e.* lines connecting two nodes, which are directed in nature, as depicted by the arrows in Figure 4.10 (a).

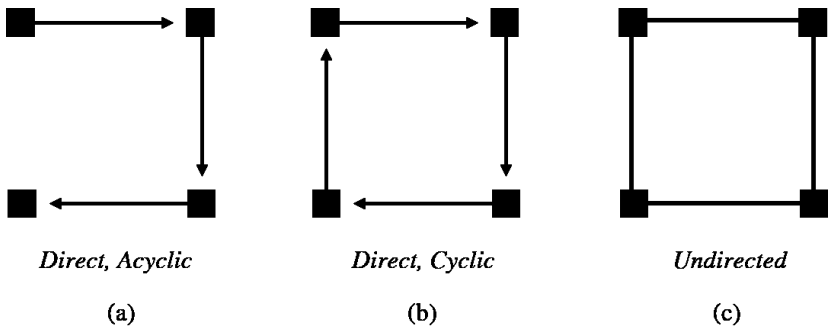

Figure 4.10 Schematics to explain different types of graphs with 4 nodes (a) Direct Acyclic Graph, (b) Direct Cyclic Graph, and (c) Undirected Cyclic Markov network.

Directionality indicates the existence of causal flow between two nodes, such that the second node is activated only after the first. In graph theory, this is referred to as topological ordering and usually implies

existence of causal flow that does not loop back to the first node to form a cycle. This chronological pathway with an end point, makes it possible to understand causation and create a model. Otherwise, it is impossible to identify a starting point; just as a chicken-egg problem. Typically, complex nature of a system can be attributed to strong parameter interdependencies, which bring strong feedback across different scales. Such systems can be best described as cyclic in nature, even if at a smaller scale causation is directed, as shown in Figure 4.10 (b). While there have been attempts to reduce Directed Cyclic Graphs (DCGs) to DAGs[161], not all systems can be satisfactorily modeled as DAGs. Open questions at this juncture include whether causality can be discovered in a DCG at all[162], if the DCG in question can be satisfactorily reduced to a DAG, and what kind of information would be lost or misinterpreted through this assumption. Cyclic systems, on the other hand, are better described by undirected Markov networks (Figure 4.10 (c)) than by BNs. Markov networks are those in which the probability of events occurring in a system depends only on the previous state of the system. This can be made possible with kMC: if the chain of events in a complex system can be converted to an event graph with topological ordering, then at the end of the chain, updated system parameters can be stored and used to describe a new state of the system for the next iteration. The kMC algorithm also provides scalability of time step based on how dynamic the system is, *i.e.* fast dynamics yields smaller time steps and slow dynamics gives longer time steps.

Nodes in a directed graph can either be *d-connected* or *d-separated*, where *d* stands for *directional*. When two nodes are dependent on next each other by causation, a continuous path (*i.e.* an edge or consecutive edges regardless of direction) is said to connect the two nodes. For instance, in Figure 4.11, a continuous path can be found between nodes x-r, x-t or r-s on one side, and y-v, y-u or y-t on the other side of the collider node t. A collider node is one which receives two directed edges as input and does not transmit any information forward, therefore a continuous path should not contain a collider node. Nodes on either side of the collider node are d-separated, *i.e.* they are independent and not connected by causality; for example, x-y, x-u, or r-u in Figure 4.11. Root nodes are defined as those which act only as inputs into the graph; in Figure 4.11, those are x and y. It is also possible to consider conditional d-connectedness between two nodes, as noted in the following section, this will allow conversion of a DCG to a DAG.

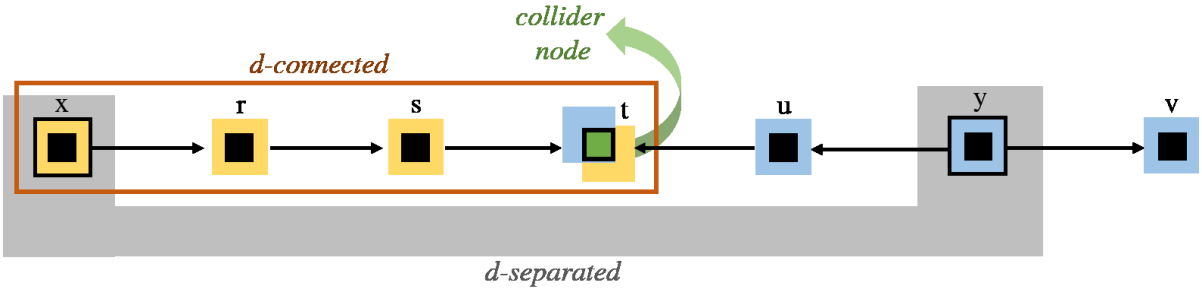

Figure 4.11. Schematic showing a collider node and describing d-connected and d-separated nature of a pair of nodes in a graph.

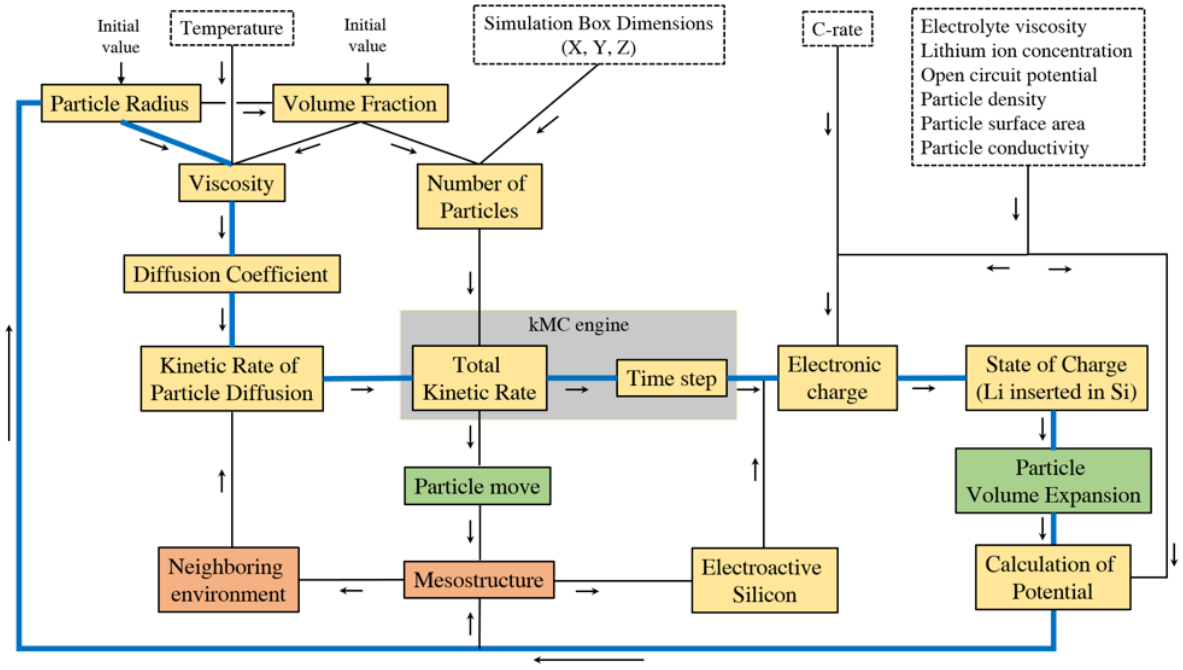

Figure 4.12. Schematic of a causal flow diagram: Root nodes are specified by boxes with dotted lines and include the starting values. The main cycle is highlighted in blue suggesting its DCG nature. Boxes with colors yellow, green, and orange indicate that the entity is a state descriptor, dynamics descriptor, and spatial descriptor, respectively.

The graph with reduced complexity (reduced compared to real, experimental conditions), is constructed based on the aforementioned discussions and is shown in Figure 4.12. It provides the flow of logic for the algorithm used in the ABM-kMC model and offers a means to quantify complexity. The kMC engine used to calculate time steps from system dynamics is highlighted in grey in Figure 4.12. The root nodes (in dotted line boxes), are namely temperature, simulation box dimensions, C-rates, initial values of particle radius and volume fraction, and other parameters used for estimation of electric potential. All the other nodes (in solid lined boxes) show a high degree of d-connectedness and parameter interdependence.

Here, there are no true collider nodes because every node passes information forward to another node even if it receives multiple inputs. The main chain (in blue in Figure 4.12) represents the causal flow: particle radius → viscosity → diffusion coefficient → kinetic rate → total kinetic rate → time step → electronic charge → state of charge → volume expansion → calculation of potential → particle radius, therefore, the graph can be categorized as a DCG. Here, the last edge is conditional, such that if the potential crosses the cut-off potential, the simulation stops. Additionally, the final directed edge: volume expansion → particle radius is separated between time steps and model iterations, breaking the DCG into a DAG.

At the end of each model iteration, parameter updates along the traversed nodes are saved and the next iteration is implemented over the new state of the system, thus adopting the required Markov property. Different nodes in Figure 4.12 can be classified as state descriptors in yellow and dynamics in green. Of the state descriptors, viscosity, state of charge, and total electrode potential are observable while most others, especially at the single particle level, are latent parameters. The orange boxes are spatial descriptors which track arrangement of particles in three-dimensional space and can be elaborated by many other parameters which are not mentioned here for the sake of brevity. As evident from the graph, multiple smaller DCGs overlap with the main causal chain (in blue). Increments are only made one time to the parameters that fall along the main chain, while all side branches are implemented once and their impact is observed in the following cycle. For instance, the moving particle can be

excluded from the estimation of electronically percolating networks such that both particle diffusion and electrochemical discharge can be said to occur simultaneously, while still maintaining a degree of causation.

It should be noted that nodes with multiple inputs, like viscosity, particle diffusion rate, mesostructure, and electric charge are important. The greater are the number of competing forces that influence the output from a node, more are the chances that its behavior will be non-intuitive. Thus, the prediction of these parameters is expected to be difficult to experimentally quantify in order to obtain an empirical relationship. The nature and population of such nodes are an important metric for complexity for a given system. These nodes are not only difficult to predict, they bring complexity to the entire graph. Such that non-intuitiveness ripples and cascades across the entire system. Thus, even experimentally observable parameters can show unexpected trends and emergent behavior.

4.5. Summary and Conclusions

This chapter explores the mechanistic model through parameter sensitivity analysis (PSA) to discover its features, strengths and weaknesses as a method. A local PSA is first performed with respect to the experimental conditions published in literature. The sensitivity of discharge capacity is studied in terms of (i) simulation box size with depth, Z = 6, 8, 10, 12, 14, 16 units, (ii) C-rate 2C, C, C/5, C/10, and C/20, and (iii) carbon content with 3, 5, 7, 9, 11, 13, 15, 17 v%. The capacity is seen to decrease with increasing Z and C-rate. The impact of increasing carbon content consists of an increase in capacity followed by a saturation, which roughly resembles the sigmoidal curve experimentally obtained. More accurate distinction between the percolation and saturation region can be obtained by exploring the evolution of the size of the conductive network and the number of silicon particles in contact with the conductive network.

A larger scale PSA is conducted over 288 cases where depth, C-rate and composition are simultaneously varied, with Z = 6, 10, 14 units, C-rates C/5, C/10, C/20, silicon content of 6, 10, 14, 18 v%, carbon content of 3,

5, 7, 9, 11, 13, 15, 17 v%. Each case was simulated 5 times and averaged for reproducibility. The evolution of error bar as well as the computational efficiency of the model were studied as a function of composition and simulation box size. This provides a useful tool to quantify the compromise between accuracy and efficiency for a given algorithm. Furthermore, this large amount of data provides a means to explore sensitivity of the transition between percolation and saturation region, called *conductivity threshold* for convenience. Sensitivity of this threshold depends not only on the parameter but also the value of the parameter, for instance, the threshold is more sensitive to silicon content at 14 v% rather than 10 v%. It was observed that depth was the most sensitive parameter, suggesting that finite size effects could overshadow physically relevant mechanistic details. After modifying an algorithmic detail that reduced the degree of discreteness of the model and made the particle radius vary in a more continuum-like fashion on volume expansion, the error bars of the results were significantly reduced. Additionally, a larger range of simulation box sizes were simulated, Z = 6, 10, 14, 18, 22, 26 units and it was observed that above Z = 18 units, convergence in behavior was observed and simulation box artefacts reduced.

The complex origin of finite size effects in this discrete model unveils the complex parameter interactions that take place within the model. Graph theory was introduced as a perspective tool to characterize and quantify the interdependence of parameters to provide a clear causal flow chart. It was observed that complexity arises from a specific class of nodes, or parameters, which have a large number of inputs. This results in a competition between numerous effects resulting in potentially non-intuitive output from the given node, substantiating claims that complexity arises from the many-phenomena problem. This kind of behavior cannot be described by simple empirical relations, thus showing the importance of creating models with flexible theoretical frameworks with causal flow graphs.

Chapter 5

Insights on Phenomena

5.1 Case Study

Based on studies published from density functional theory studies, one can assume that fully delithiated silicon, whether crystalline or amorphous, is expected to be a poor electron conductor due to lack of density of states at the Fermi level, however this property changes in the presence of inserted lithium.[116] From a mechanistic point of view, it can be interesting to study the impact of silicon participating in forming conductive networks. The following sections elaborate the power of a mechanistic model to offer insights for a SSRFB and showcase how, very much like in experiments, behavior can emerge from such models due to the many-body and many-phenomena effects.

5.1.1 Conductivity Switch for Silicon

The Python code used for this study was generation II, which offers more computational efficiency and is elaborated upon in the Appendix A.1.1. The algorithm described in Chapter 3 is modified in terms of: (a) conductivity switch (σ on/off) which controls the participation of silicon in networks, *i.e.* an inter-particle electronic conductivity, and (b) lithiation rate of silicon due to intra-particle electronic conductivity, for rigor. The latter condition is implemented by having charge uptake 100 times slower at the very beginning of lithiation, such that conductivity has two values or two steps. The study is performed in a cubic simulation box with a 20 unit cell of edge length 300 nm at C/20. Silicon content of 6 v% and 14 v% are chosen to study the behavior above (13 v%) and below (5 v%) the conductivity threshold, as observed in the previous chapter. Three distinct cases are considered for these four slurry compositions (Figure 5.1): (a) constant lithiation (CL) without silicon participating in networks (σ off), highlighted in black circles, (b) two-step lithiation (2SL) without silicon participating (σ off), highlighted in blue triangles, and (c) two-step lithiation (2SL) with silicon participating (σ on), shown in red squares. Each of the 12 cases was simulated three times and averaged in Figure 5.1 (a)-(d), which shows the distribution of particles in terms of state of discharge. The results show that introduction of the two-step lithiation

has little impact for cases (i) 6 v% Si + 5 v% C, (ii) 14 v% Si + 5 v% C, and (iii) 6 v% Si + 13 v% C, and a very marginal impact in (iv) 14 v% Si + 13 v% C. Since error bars in x-axis are case dependent and hard to display in the same plot, the raw data is classified based on four types of distributions summarized in Table 5.2 and assigned to the different cases in Table 5.1.

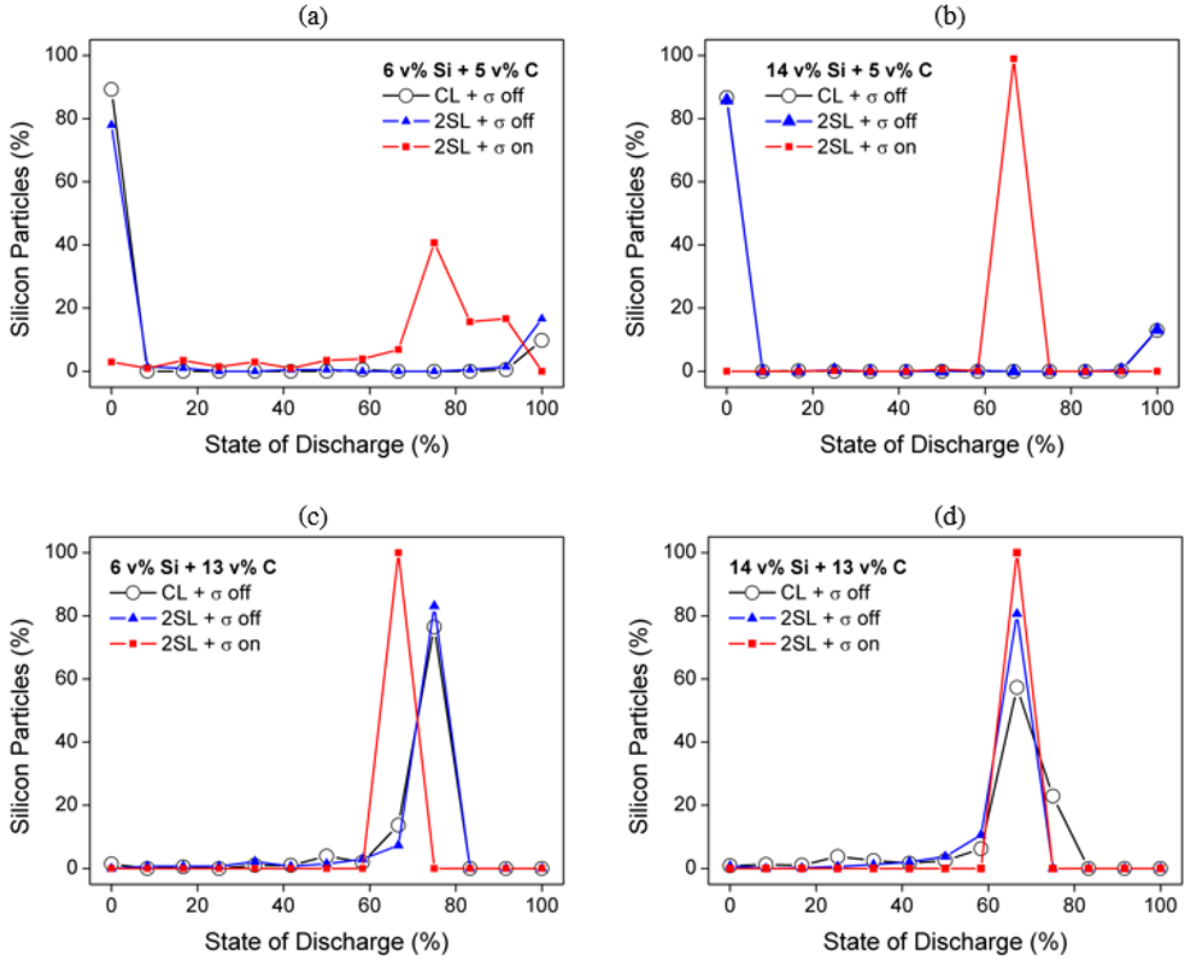

Figure 5.1 : Constant lithiation (CL) without silicon participating in networks (σ off), highlighted in black circles, two-step lithiation (2SL) without silicon participating (σ off), highlighted in blue triangles, and two-step lithiation (2SL) with silicon participating (σ on), shown in red square for compositions (a) 6 v% Si + 5 v% C, (b) 14 v% Si + 5 v% C, and (c) 6 v% Si + 13 v% C, (d) 14 v% Si + 13 v% C.

Table 5.1 Summary of capacity and particle size distribution (PSD) obtained for three cases studied to incorporate the conductivity switch for silicon, at different slurry compositions.

Composition (v%)		CL + σ off		2SL + σ off		2SL + σ on	
Si	C	PSD #	y of Li	PSD #	y of Li	PSD #	y of Li
6	5	2	0.12	2	0.26	4	0.75
14	5	2	0.19	2	0.14	1	0.68
6	13	3	0.74	3	0.74	1	0.74
14	13	3 / 4	0.68	3	0.68	1	0.68

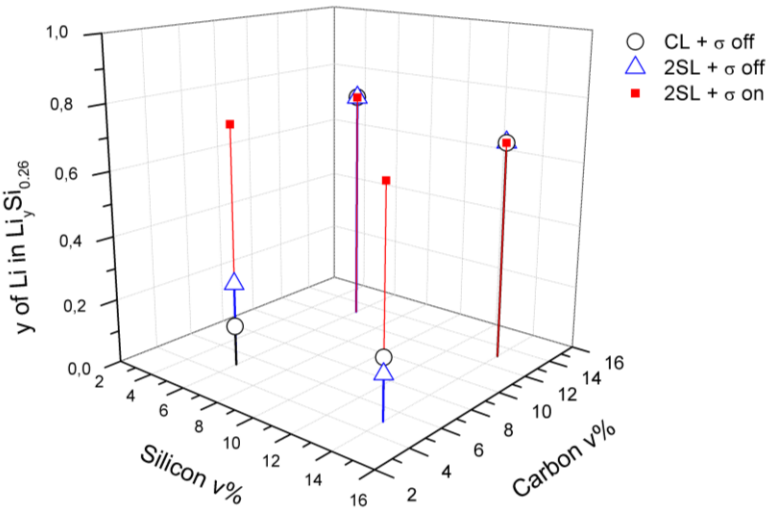

Figure 5.2 Data from Table 5.1 presented in a 3D plot for three cases at different compositions

Meanwhile, red curves in Figure 5.1, which correspond to the on-switch, show an unmistakable shift towards higher capacities, especially for carbon content below the conductivity threshold. This result is reasonable and intuitive since carbon, by itself at this volume fraction, is insufficient to form networks (as seen in Chapter 4). The overall capacity obtained at discharge for each case is shown in Figure 5.2 and summarized in Table 5.1. Capacity obtained at the end of discharge is normalized in terms of $Li_ySi_{0.26}$ such that y goes from 0 to 1. The three-dimensional plot in Figure 5.2 is used particularly to collectively visualize the three cases at four different slurry compositions.

Table 5.2 Categorization of particle size distributions (PSDs) observed.

PSD #	Centre	Symmetry	Spread	Reproducibility
1	Unimodal	Symmetric	Low	High
2	Bimodal	Major & Minor Mode	Low	High
3	Multimodal	Left skewed	Moderate	Reasonable
4	Multimodal	Left skewed	Moderate to High	Low

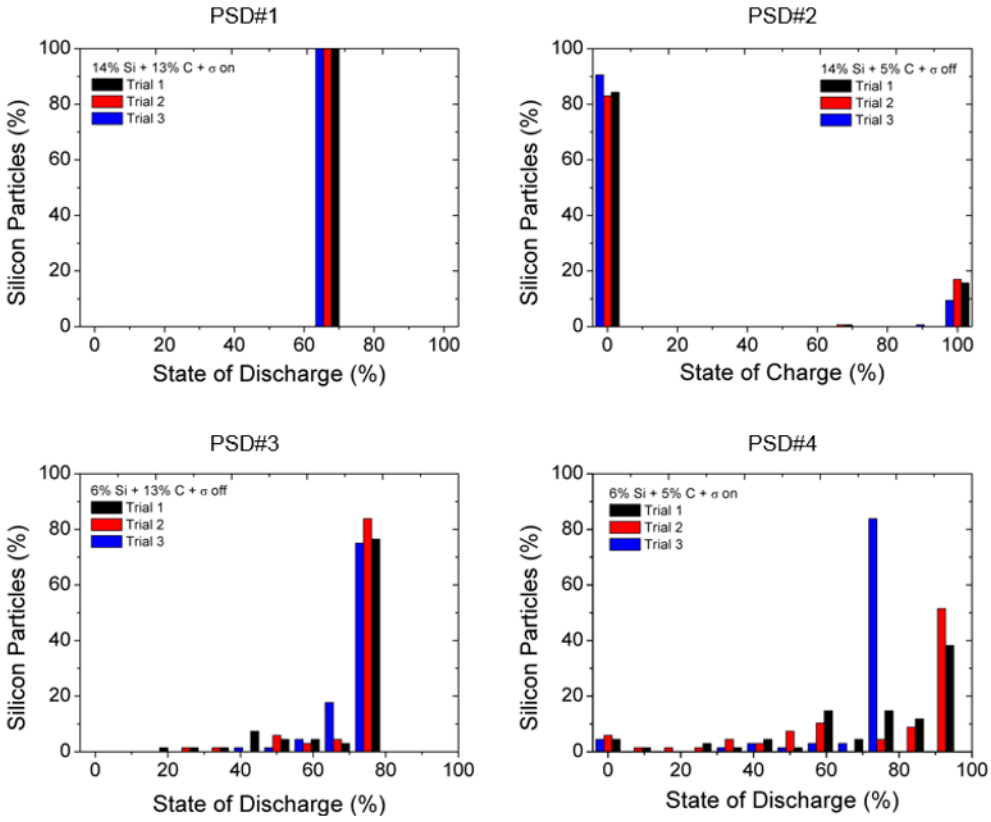

The four dominating types of dispersions observed can be described in terms of modality, symmetry, spread, and reproducibility in different runs, as shown in Table 5.2. In terms of mechanistic details, it can be said that PSD#1 corresponds to simultaneous discharge of nearly all silicon particles, suggesting an extensive conducting network. This is confirmed by studying the corresponding conductive particle network, seen in Figure 5.3 (c) where the green, blue, and red curves show a consistently good network with little fluctuation.

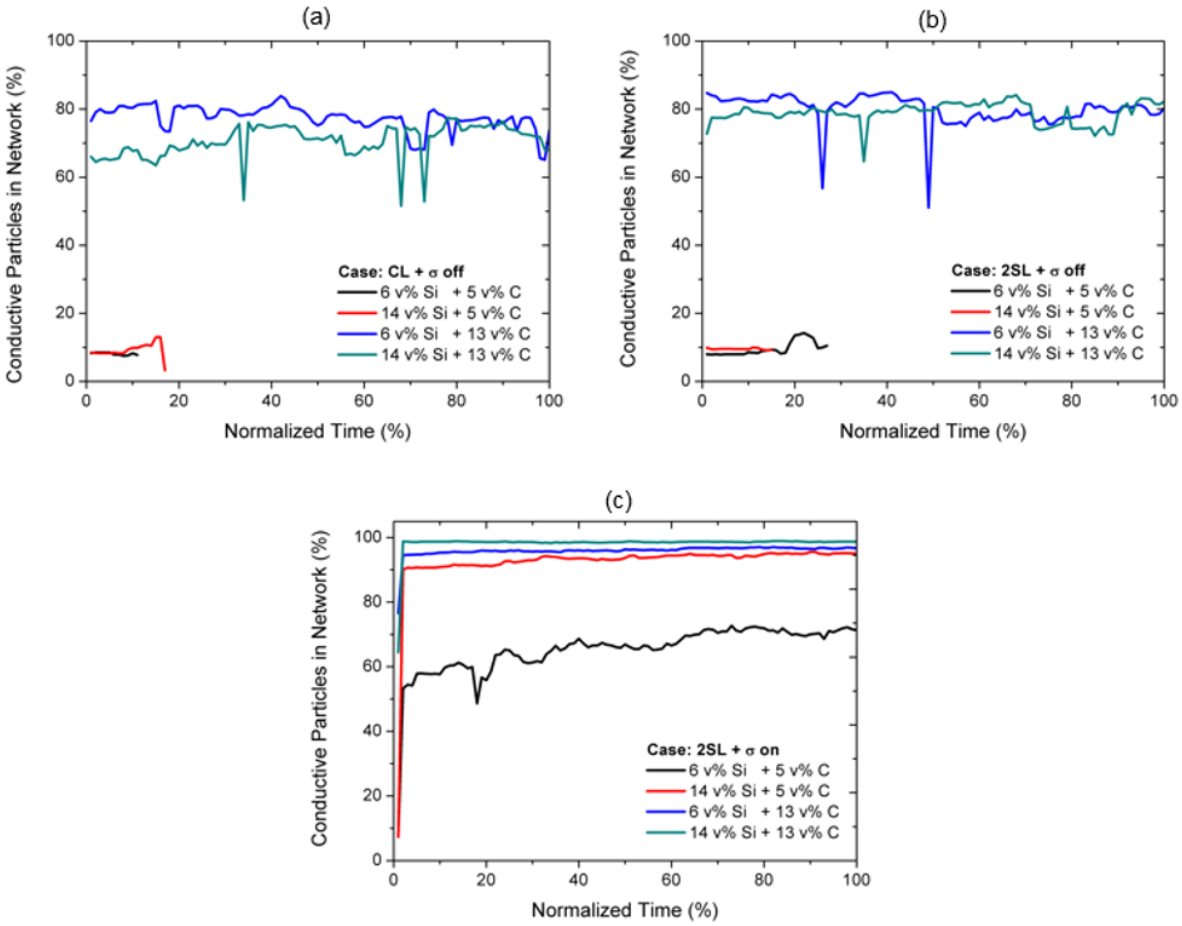

Figure 5.3 Impact of slurry composition on the evolution of conductive particle networks with time for the three cases.

The case for bimodal distribution, as in PSD#2, indicates that conductive network has limited reach, possibly only around the current collector since a small population of particles discharge completely while the rest remain unlithiated. The corresponding conductive particle network formation, seen as the black and red curves in Figure 5.3 (a) and (b), clearly corroborates this observation. The population of particles participating in the conductive network are significantly low and the discharge lasts for a much smaller time period when compared to PSD#1, which is further confirmed by the low capacity obtained. Case PSD#3 has a single sharp peak and an asymmetric distribution with small trailing peaks. This appears to suggest that most of the particles are well connected to a network while others receive charge sporadically. The case PSD#4 with a wide dispersion of peaks

and state of discharge, suggests that most particles receive charge intermittently, indicating that there can be large fluctuations in the nature of the conductive network and thus poor reproducibility among simulation runs. While it is not straightforward to assign PSD#3 or #4 to curves in Table 5.2, subtle differences in the highly fluctuating curves of Figure 5.3 provide some insight. Blue and green curves in Figure 5.3 (a) and (b) can be classified as predominantly PSD#3 as shown in Table 5.2, in that while there are large fluctuations, the nature of the conducting network does not undergo significant change in terms of size. The black curve in Figure 5.3 (c) shows less fluctuation but instead displays an upward slope, suggesting that the size of the network is increasing. The evolving nature of the network would eventually be highly dependent on where the particles are originally placed and result in chaotic, non-reproducible dispersions at the end of discharge and thus can be classified as PSD#4.

The subtle differences in collective particle behavior for different cases which otherwise produce identical overall discharge capacities, is an important strength of this model. The impact of the two-step lithiation rate in the initial stages is eclipsed by consequent discharge steps, making it easy to draw conclusions for the impact of silicon particles participating in conducting networks. A system where lithiation rate of a material depends on its extent of lithiation, can be ascribed to have recursive interdependencies and would be represented by directed cyclic graphs, as discussed in Chapter 4. The advantage of defining a mesoscopic parameter like lithiation rate of a particle is that it allows a vast number of microscopic properties to be bundled together. Aside from conventional parameters like ion transport, lithiation rate is governed by a massive interconnection of other parameters. For instance, simple concepts like electronic and ionic conductivity of a particle arise from a myriad of interlinked physical and chemical aspects like crystal structure dynamics, existence of grain boundaries, and nature of solid electrolyte interface. Introduction of such a parameter which can be termed as *emergent* is a significant step towards handling complexity in this system. Without explicitly and individually quantifying the microscopic influences, significant understanding of complexity can be attained by studying the impact of lithiation rate as various mathematical functions which are assumed to be the resultant of all the microscopic influences.

5.1.2 Multi-Parameter Sensitivity Study

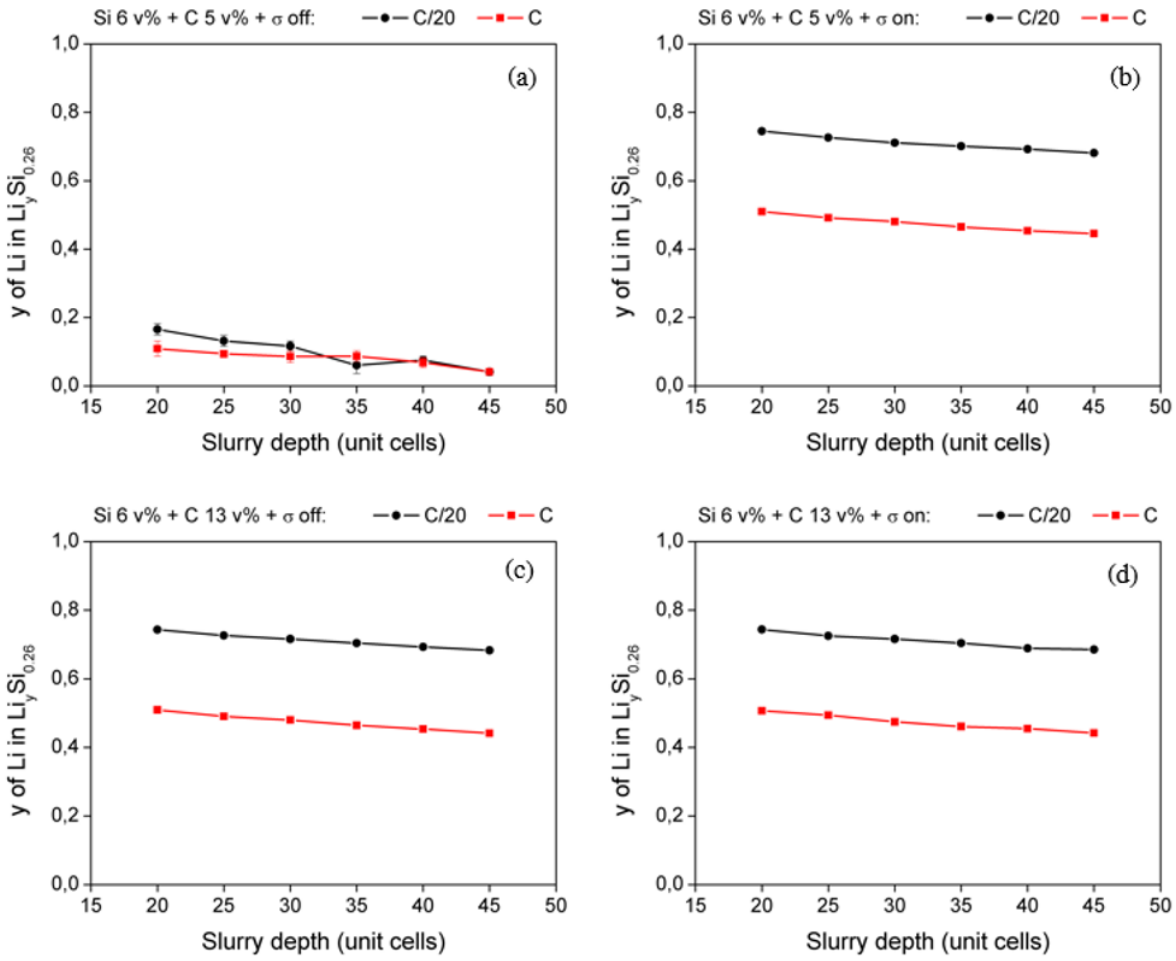

Figure 5.4 Impact of silicon conductivity switch on slurries with composition: (a)-(b) Si 6 v% + C 5 v%, and (c)-(d) Si 6 v% + C 13 v%, studied at different simulation box depths and C-rates.

When studying the impact of C-rate, simulation box depth, and carbon content simultaneously in context to the conductivity switch, silicon content 6 v% (Figure 5.4) and 14 v% (Figure 5.5) are studied and both show similar behavior. The simulation box depth was varied across values 20, 25, 30, 35, 40, and 45 units and for the two silicon fractions, carbon content was chosen to be above and below threshold, *i.e.* 5 v% and 13 v%, and C-rates chosen were C/20 and 1C. In total, the 192 cases were run 3 times for reproducibility and the results were

averaged. Regardless of silicon content, the only case that showed very poor capacity were those with 5 v% carbon where silicon conductivity was switched off, while all the other cases showed the existence of conductive networks. The PSDs for both 6 v% and 14 v% are similar and Figure 5.6 shows only the latter as an example, specifically for the condition where the silicon conductivity switch is off. The cases with 5 v% carbon content at 1C or C/20, both of which show very low discharge capacity, are shown in Figure 5.6 (a)-(b) and can be classified as PSD#2. Above the threshold, for 13 v% carbon content, PSD#3 is observed in Figure 5.6 (c)-(d), here the mode is shifted to a lower state of discharge for 1C.

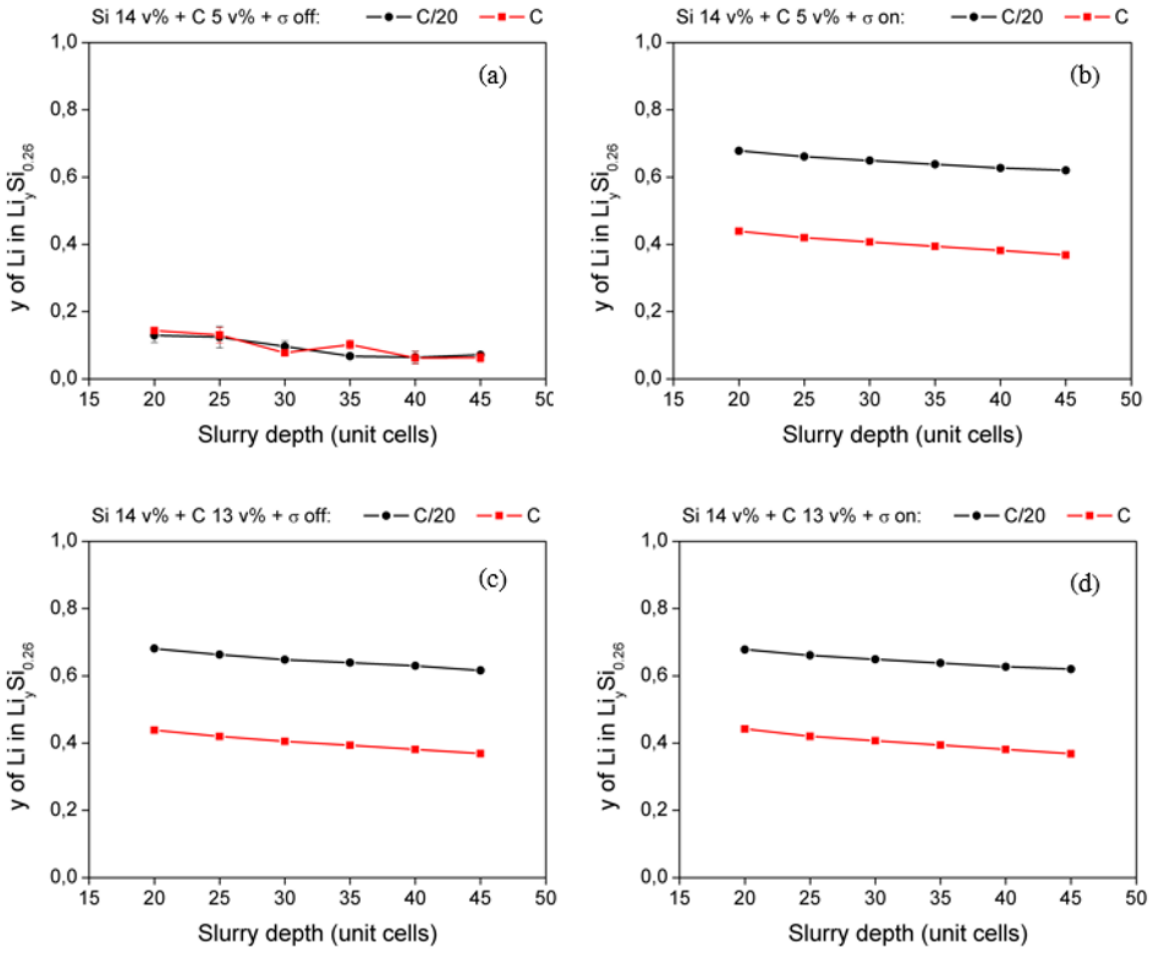

Figure 5.5 Impact of silicon conductivity switch on slurries with composition: (a)-(b) Si 14 v% + C 5 v%, and (c)-(d) Si 14 v% + C 13 v%, studied at different simulation box depths and C-rates.

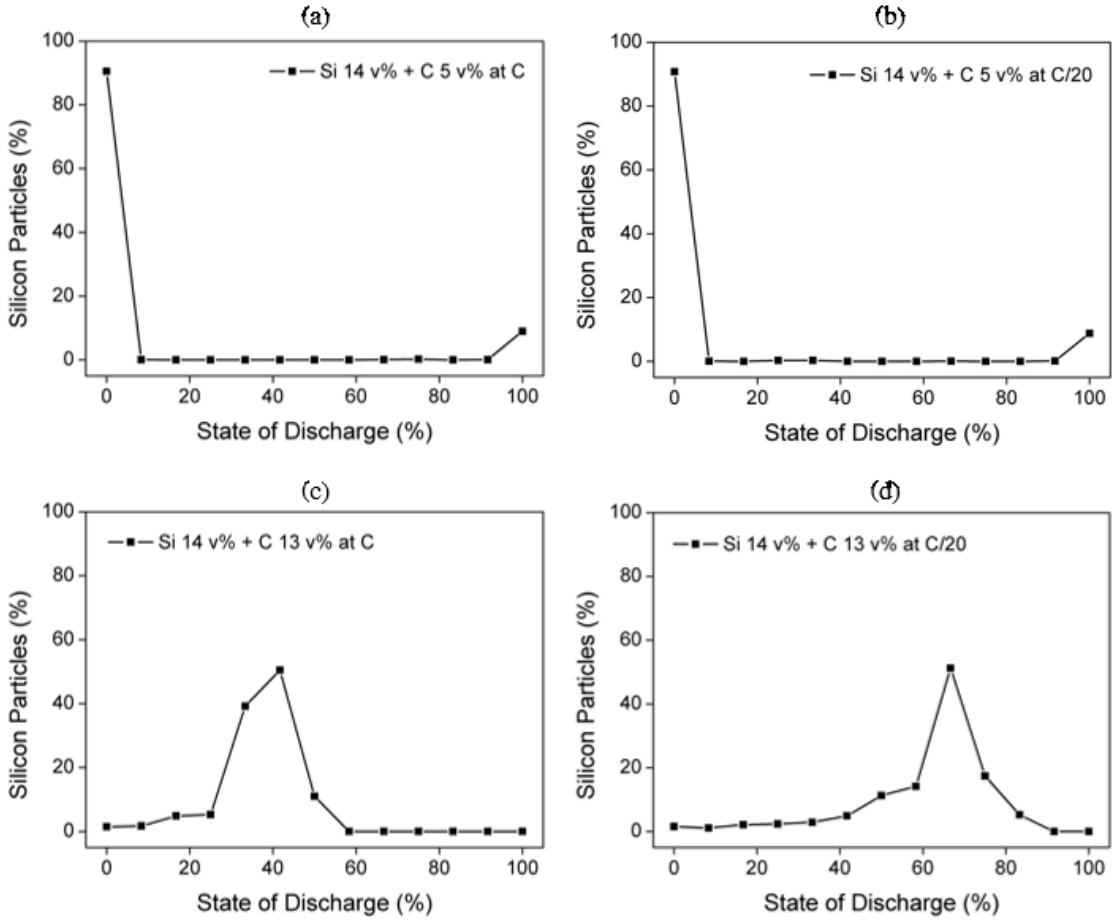

Figure 5.6 Particle size distribution at the end of discharge for slurry with composition Si 14 v% with 5 v% and 13 v% carbon at C and C/20.

Intuitively, it can be said that increasing simulation box depth would result in a higher probability for some silicon particles that are farther away from the current collector, to experience difficulty finding suitable conductive networks. The impact of increasing simulation box depth resulted in a 13 % capacity decrease for 1C and 9 % decrease for C/20. Slower C-rates would allow more time for particles trapped at the bottom of the simulation box to move through the box and access conductive networks, thereby explaining why capacity falls faster at 1C than at C/20. The impact of higher silicon content is less intuitive, for instance increasing the silicon content from 6 v% to 14 v% at 13 v% carbon resulted in an 8.5 % decrease in capacity at Z = 20 and 9.5 % decrease at Z = 45, at C/20. On the other hand, at 1C, a 13.5 % decrease at Z = 20 and 16.7 % decrease at Z = 45 was seen.

Simultaneously increasing silicon content and switching off silicon conductivity is advantageous at Z = 20 at C/20 and at Z = 45 at 1C but disadvantageous at Z = 20 at 1C and Z = 45 at C/20. This indicates that silicon can play both, a constructive and a disruptive role in the formation of conductive networks, even if it is electronically conducting. The non-intuitiveness observed within these 192 cases where 5 parameters are varied, clearly originates from numerous competing mechanistic effects. Therefore, complexity arising from such an interplay at the mesoscale where the many-body problem is significant, would be far more convoluted within an experimental study.

Studies to observe the impact of active material without volume expansion, are underway. Here, even though silicon is assumed to experience significantly more volume expansion than typical LIB materials, the relative trends identified through large scale PSA can provide a generalized guideline for similar electrochemical systems. This is demonstrated in the following comparisons made amongst published research. Considering multiple variable parameters in experimental studies is gaining importance but is very challenging to accomplish within traditional approaches. A publication by Madec *et al.*[79] which is most closely relevant to the simulations hereinabove, studies electrode capacity as a function of C-rate, channel depth, and active material concentration such as LTO. While the electrode capacity is seen to decrease at faster C-rate, the trend is non-linear and shows dependence on nominal values of channel depth and LTO concentration.[79] Similarly, when increasing channel depth, capacity is seen to fall but its trend is highly dependent on LTO concentration and C-rate.[79] Within the publication, this behavior is simply attributed to poor electrical contact but the nuances of individual trends are not explained. A study by Dennison *et al.*[25] reports slurry conductivity as a function of salt concentration in electrolyte. Electrolytes with lower salt concentrations show sharp decline in conductivity while higher salt concentrations do not show a significant correlation.[25] While no explicit evidence is given to support the following explanation, the phenomena is ascribed to the ability of ions to screen interparticle repulsive forces and promote aggregation sufficient for formation of carbon chains, but not enough to induce flocculation.[25] This suggests that the non-linear sensitivity of LTO based slurries towards channel depth could result from insufficient salt concentration. While this is usually optimized for handling transport limitations in conventional lithium ion

batteries, it may not be enough to prevent flocculation in suspensions. There are no studies showing simultaneous impacts of carbon, C-rate, and channel depth on capacity. Given the high dependence of sensitivity of capacity on (i) C-rate and channel depth[79] and (ii) carbon content[84] reported separately in literature, our model predicts that their simultaneous impact on capacity will be highly competitive, system specific, and non-intuitive.

5.1.3. Studying Slurry Compositions

Various slurry compositions were simulated with both off and on switch for silicon conductivity. The data presented in Figure 5.7 shows a summary of 121 compositions with silicon conductivity switch off, each simulated thrice, with silicon content (3, 4, 5, 6, 7, 8, 9, 10, 11, 14, 15 v%) paired with carbon content (0, 2, 4, 6, 8, 10, 12, 14, 16, 18, 20 v%). Since the trends obtained are fairly similar, two extreme cases for silicon content are chosen in Figure 5.7(a), to show the range of capacity values obtained.

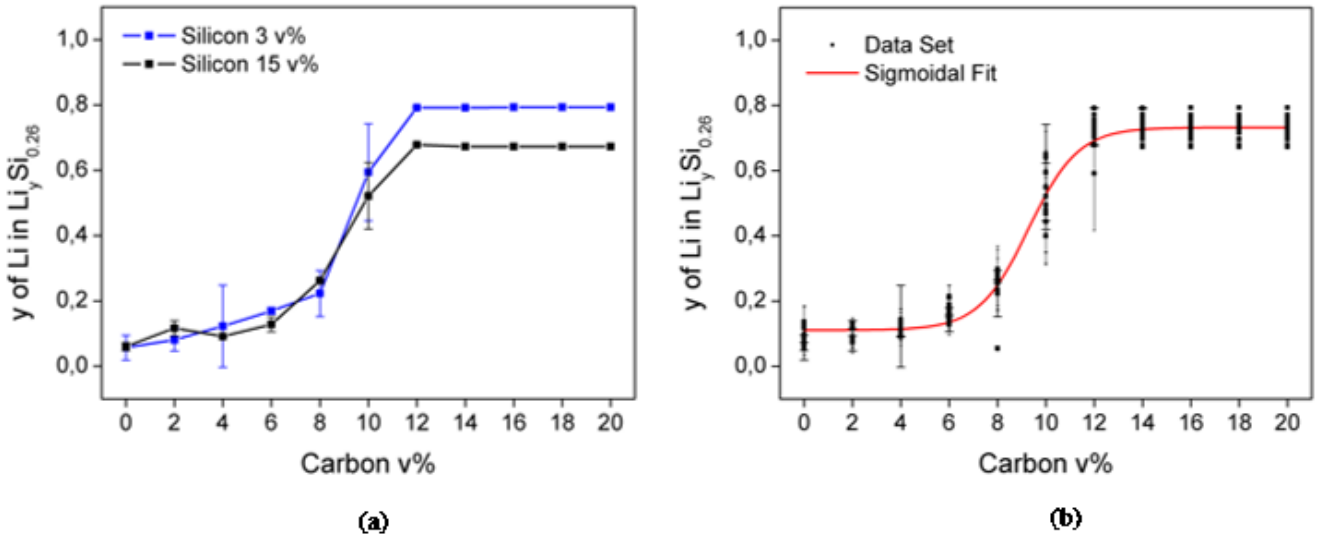

Figure 5.7 Out of 121 compositions simulated with silicon conductivity switch off, with silicon content (3, 4, 5, 6, 7, 8, 9, 10, 11, 14, 15 v%) and carbon content (0, 2, 4, 6, 8, 10, 12, 14, 16, 18, 20 v%), two extreme cases are shown in (a) and the entire data set with error bars is shown as a scatter plot in (b) with a sigmoidal fit.

All the data points for the 121 cases are shown as scatter points in Figure 5.7(b), with a sigmoidal fitting shown in red. It is evident that silicon content does not significantly impact the salient features of the sigmoidal trend. Under the assumptions of the first and second generation Python code (described in Appendix A.1.1), which can take only a small population of carbon particles into account, the grid size was increased to accommodate two carbon particles in one grid unit space. Given these conditions, one may estimate that percolation region between 6 v% - 14 v% obtained from Figure 5.7(b), would otherwise be attained between 3 v% - 7 v% for a spherical particle or an aggregate size of 150 nm. Based on the carbon entity and its size, whether considering an elementary particle, aggregate or cluster, this model is capable of capturing the network formation of that entity by adjusting the grid unit size. Simultaneously considering carbon entities at different scales can be computational challenging, but possible in a telescopic multiscale model, or with reduced, representative entities. Assuming that obtaining suitable electronic conductivity for battery operation and the condition for Brownian particle to obtain a stable suspension enforces submicron particle sizes, it is reasonable to simulate with a grid unit cell of around 300 nm, halfway between the size of an elementary carbon particle and an aggregate.

Experimental work published by Parant *et al.*,[84] shows two types of conductive carbons of significantly different bulk densities, Ketjenblack 600JD (AzkoNobel) and Ensaco (Timcal), whose conductivity varies roughly like a sigmoid. The study was conducted in aqueous medium with 1.5 wt% Arabic gum as emulsifier and 0.5 wt% alginate as thickner. The elementary particle size obtained through TEM images of raw powders was 23 nm ± 14 nm for Ketjenblack and 61 nm ± 19 nm for Ensaco, while aggregate sizes are as large as a few microns. Optical microscopy of suspensions suggests particle aggregation can lead to clusters spanning 200 μm. Parant *et al.*[84] report estimated percolation thresholds starting at 3.6 v% for Ensaco and 8.1 v% for Ketjenblack and TEM images of dry powder clearly show complex networks and chains of elementary particles. In-situ TEM studies in wet mode performed in-house with silicon and carbon based slurries in organic electrolyte (LP30) were challenging due to air bubbles, blurry images, particles sticking to the cell window, and beam effects (see Appendix A.2.2).

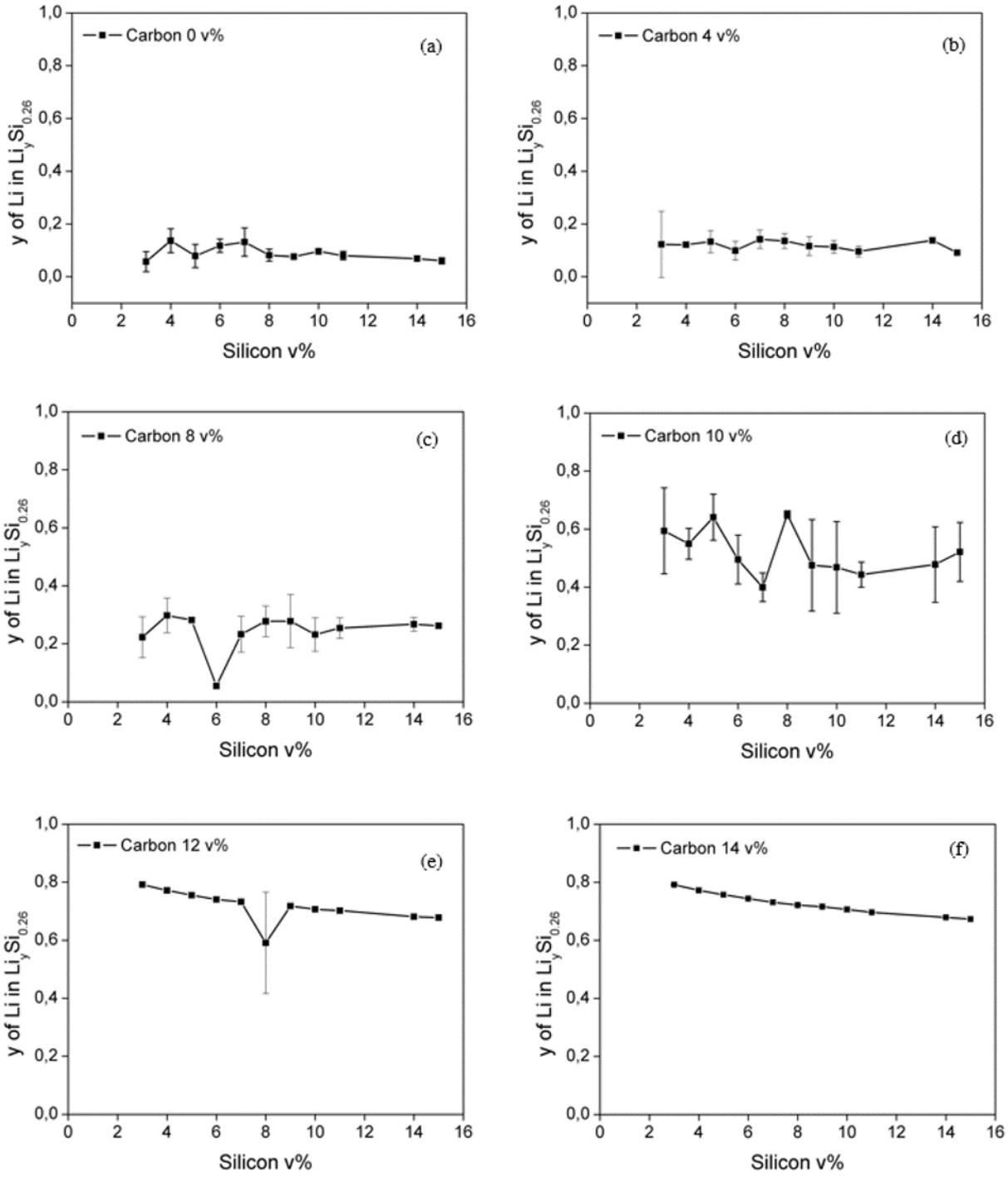

Figure 5.8 Representation of data set plotted in Figure 5.7 in terms of capacity as a function of silicon content for the 121 cases.

Various rheological studies offer visualizations and mechanisms of complex particle arrangements, showing the importance and relevance of simulating with submicron particle entities.[27,78,86,88] It is therefore, not trivial to estimate volume fraction of solid in a given experimental system. It is also challenging to find generic metrics that are relevant across carbon types and suspension mediums so as to provide a reliable theoretical prediction of conductivity.

Data from Figure 5.7 can also be visualized in terms of increasing silicon content for a fixed carbon fraction, as shown in Figure 5.8. The resultant trends bear no resemblance to a sigmoidal curve, suggesting that increasing silicon content does not provide any mechanistic means to improve capacity and that carbon content is indeed the limiting factor. Stochasticity lends to high fluctuations within the threshold region at 10 v% carbon, and the PSD is multimodal with a large spread and low reproducibility. The error bar nearly disappears above the threshold, suggesting suitable conductive pathways to silicon particles. In general, an overall dip in capacity is observed as silicon content is increased. Considering the example of 14 v% carbon, while going from 3 v% to 15 v% of silicon, a 30% decrease of conductive material in all solid material results in a 15% decrease in capacity. It is likely that increasing non-conductive material hinders conductive network formation, which has been suggested in literature.

When electronic conductivity of silicon is taken into account, with the switch on, for the 121 slurry compositions studied in the previous section, the resulting trends are not sigmoidal, as intuitively expected. Discharge capacity as a function of carbon content and silicon content are shown in Figure 5.9 and Figure 5.10 respectively. Figure 5.9(a) and (b), show trends for 3 v% and 4 v% silicon fraction, they most resemble sigmoidal behavior. The linear part of the s-curve *i.e.* the percolation region as defined in Chapter 4, is seen to diminish on increasing silicon content and above 6 v% of silicon, the percolation region entirely disappears. The behavior of capacity versus silicon content, as seen in Figure 5.10, shows a power-law type trend, *i.e.* a sharp percolation region followed by a saturation, instead of an s-curve and above 6 v%, this curve also reverts to a linear trend.

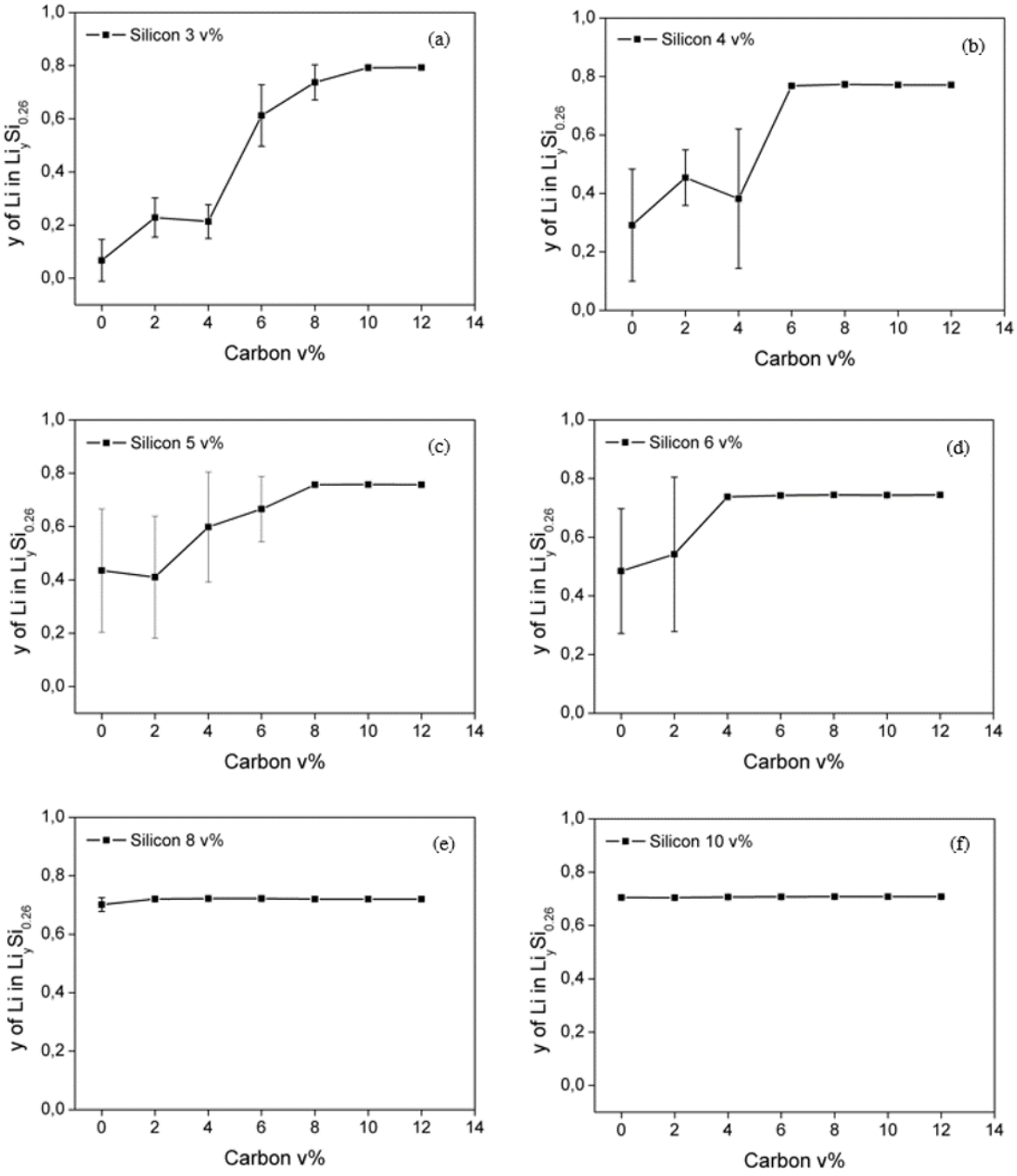

Figure 5.9 The 121 cases simulated with silicon conductivity switched on

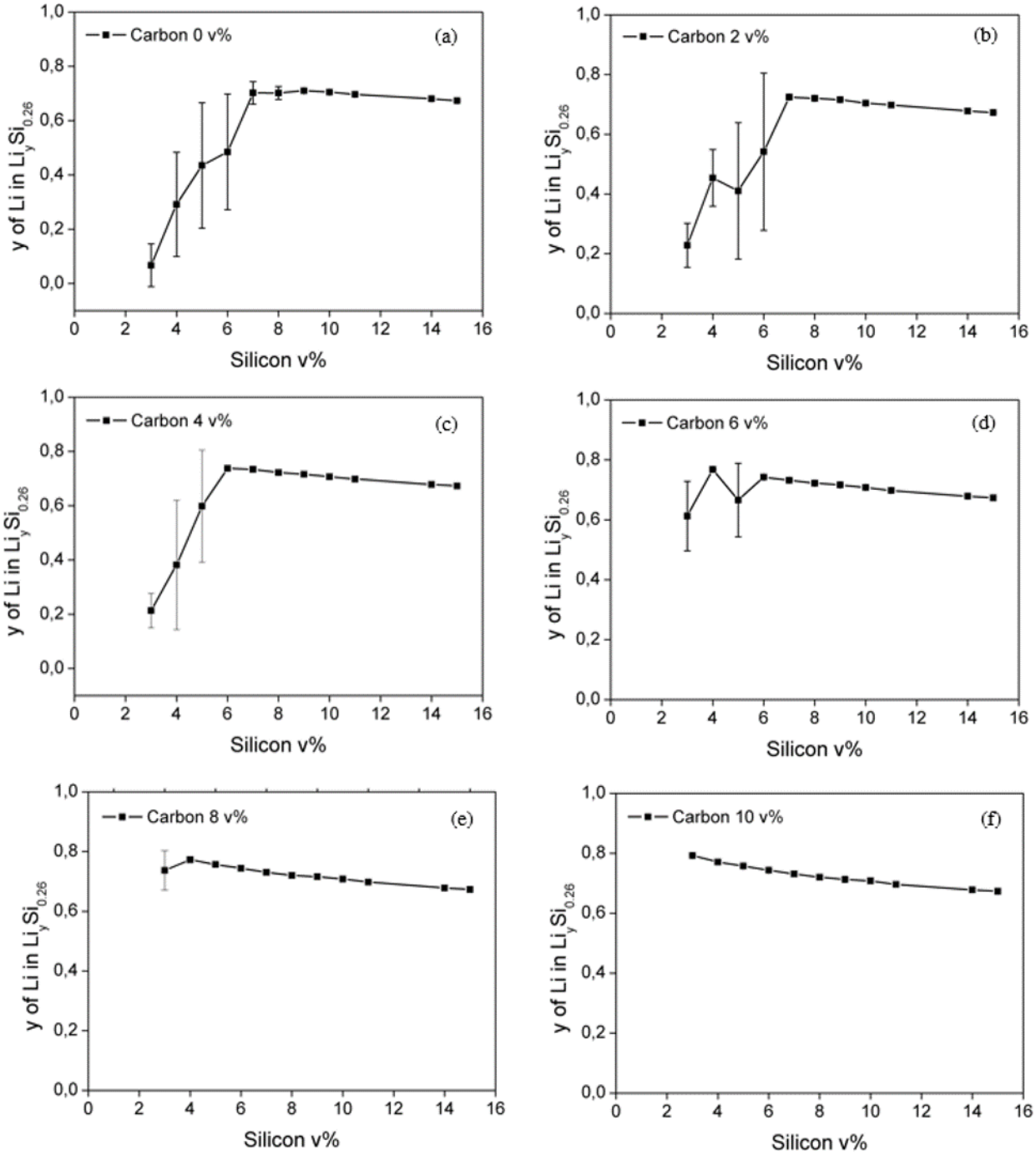

Figure 5.10 Data set from Figure 5.9 represented in terms of capacity as a function on silicon content

A gentle decrease of capacity is observed on increasing silicon content as in Figure 5.10 and not when increasing carbon content, as in Figure 5.9. This possibly arises from the role that silicon plays in the formation of conductive networks. Therefore, for slurries with low carbon content, addition of silicon is shown to drastically improve discharge capacity but after a threshold has been reached, any additional silicon content tends to slightly decrease capacity. Interestingly, at high carbon content for both on and off switch for silicon conductivity, discharge capacities tend to slowly decrease on increasing silicon content.

There is no notable difference between the sizes of the conductive network or percentage of active silicon at, for instance, 3 v% silicon or 15 v% silicon with 20 v% carbon. While this may be an artefact of having a fixed simulation box size where silicon particles are undergoing massive volume expansion, many strategies were used within the algorithm to suppress these effects. It is likely that the dip in capacity occurs due to an aggravated lithium ion transport limitation due to reduction in the number of facets of active material particles which are in contact with lithium ion containing electrolyte. This suggests that results obtained with this model can provide a global parameter sensitivity analysis, *i.e.* access all states of the system, especially those which may not be intuitive when performing experiments.

Studying the sensitivity of discharge capacity towards simulation box depth can be interesting for compositions that lie at the linear part of either the sigmoidal curve or the second order exponential curve. A composition consisting of 3 v% silicon and 10 v% carbon was considered for a multi-parameter sensitivity study as shown in Figure 5.11. The capacity is clearly more sensitive to the simulation box depth when conductivity switch is turned off. A significant drop in capacity is observed as depth is increased when the conductivity switch is off, regardless of slow or fast C-rate, as seen in Figure 5.11(a). The PSDs observed at Z = 20, Z = 30 and Z = 40 at 1C are shown in Figure 5.11(c), wherein a transition from scattered peaks in PSD#4 to bimodal PSD#2 is observed. The conductive network, as shown in Figure 5.11(d), corroborates the trends with PSDs because increasing Z results in decreasing network size. It is interesting to note that while the discharge time for Z = 30

and Z = 40 is similar, larger fluctuations in size of the conductive network are seen in the former. This possibly permits silicon particles to have more opportunity to discharge and result in PSD#4.

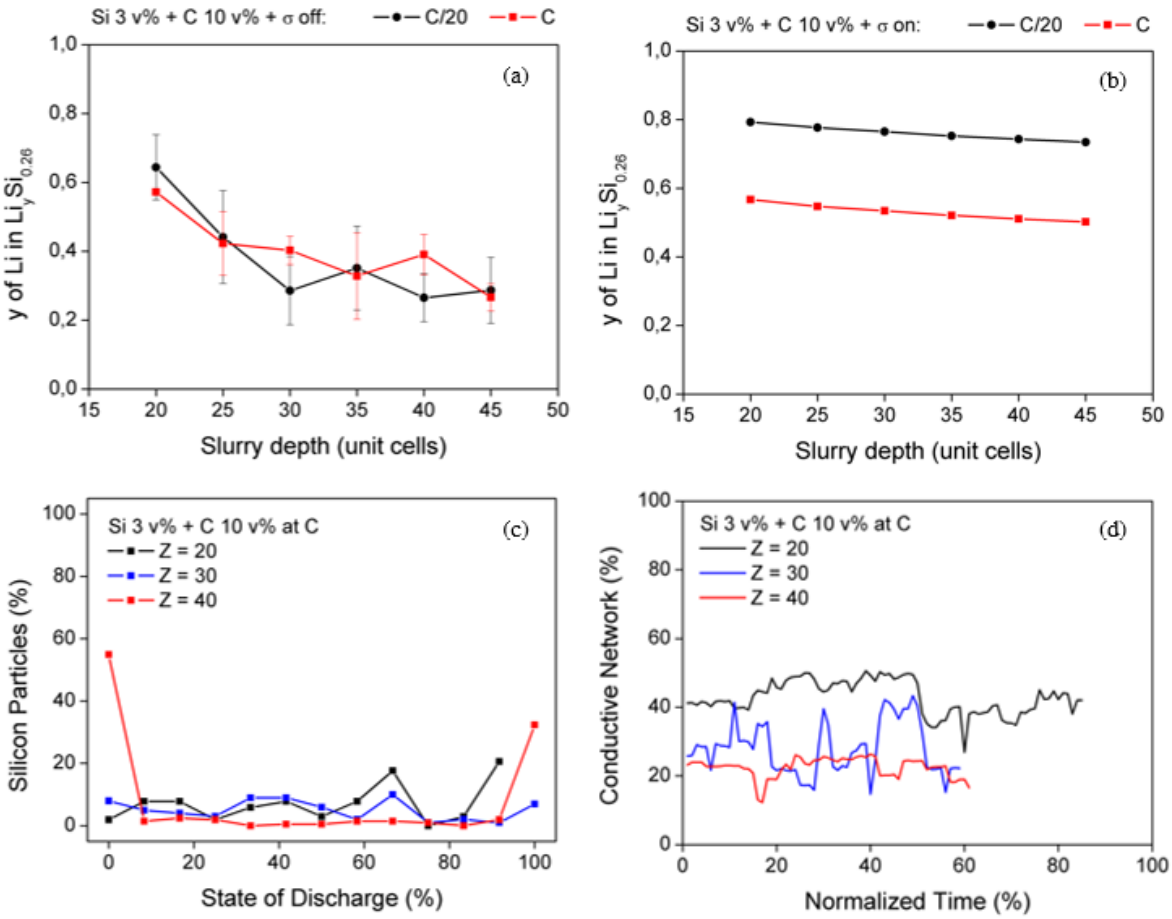

Figure 5.11 Parameter sensitivity study of slurry of composition Si 3 v% + C 10 v% at C-rate C/20 and 1C for different simulation box depths with switch (a) on and (b). Particle size distribution of silicon particles at end of discharge is shown in (c) and evolution of size of conductive network is shown in (d) for cases chosen from (a).

5.1.4. Identifying New Metrics

The results discussed hereinabove can help provide insights for experimental studies that measure conductivity as a function of composition. For instance, two studies performed with $LiFePO_4$ (LFP) material, which is usually carbon coated and thus electronically conducting, show increasing discharge capacity with increase in active material.[71,163] According to the model, such behavior would be expected when carbon content is insufficient to form an extensive conductive network. Another study with $Li_4Ti_5O_{12}$ (LTO) and Ketjen Black (KB) in organic electrolyte[79] showed that for slurries with 15 wt% LTO and 20 wt% LTO with 3 wt% KB, the particle networks were perfectly percolating and the entire LTO mass was active. However, a poorer capacity was observed for 25 wt% LTO with 3 wt% KB and it was suggested that the particle network for this case could be fragmented and consist of isolated KB clusters, rendering only a fraction of LTO electroactive. In the modeling results shown hereinabove, any significant decrease in conductivity on addition of active material is only observed within the threshold region. While this can be ascribed to stochasticity, it appears less likely that conducting carbon networks would be disrupted by active material that is considered to be electronically conducting, unless the particle size difference between the carbon entities and the active material is of several orders of magnitude.

With regard to the LTO-KB slurry, it may be reasonable to perform an even more comprehensive parameter sensitivity study to see how increasing LTO content impacts capacity at different carbon fractions. Li *et al.*[70] report such a study in their supplementary information wherein various LFP and KB volume fractions are considered for conductivity measurements. The trends appear as exponential growth curves, which may be visualized as the lower half of an s-curve. As LFP content is increased, the threshold is seen at lower carbon content. When compared to Figure 5.7 however, there is no evidence of such a shifting of capacity to lower carbon content. The sigmoidal trends seen for both cases of silicon conductivity, on and off, at 3 v% silicon are compared in Figure 5.12(a). The s-curve is observed to have shifted or translated to lower carbon content with the conductivity switch on. However, when capacity is plotted against the total volume fraction of electronically conducting particles, as seen in Figure 5.12(b), the s-curves move closer together. It is safe to assume that if the

actual number of conducting particles were captured on-the-fly during the simulations, and normalized for the differences between carbon and silicon, the two curves would overlap even more.

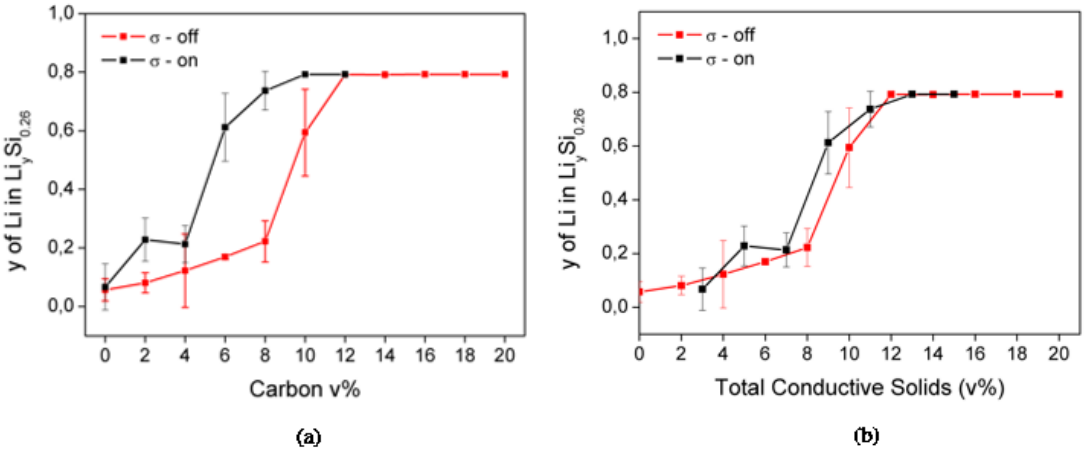

Figure 5.12 (a) Comparison between on and off switch for slurry with silicon content 3 v% on increasing carbon content, (b) data set from (a) replotted in terms of total electronically conductive solids.

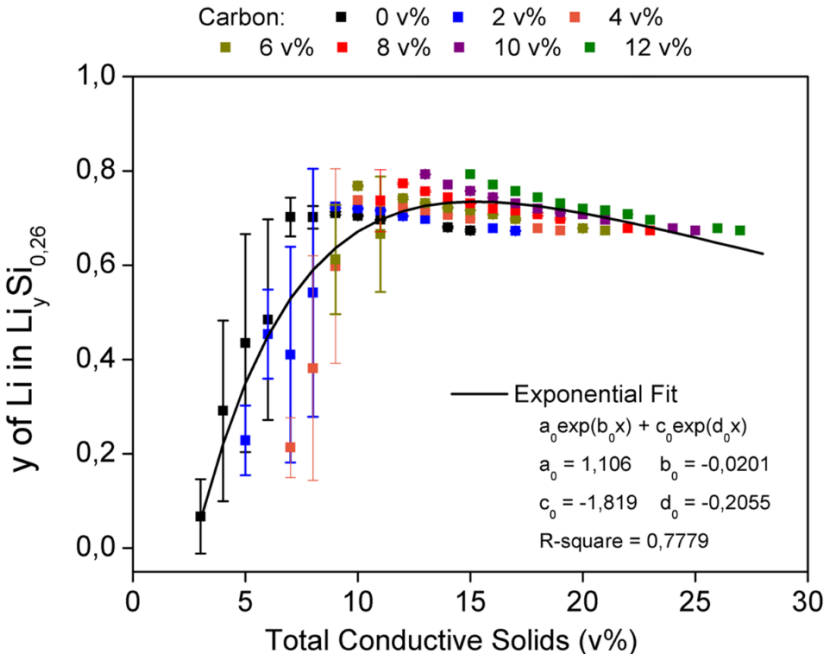

Figure 5.13 Data set for 121 cases with conductivity switch on represented as scatter plot in terms of total conductive solids with a two-term exponential fit.

Therefore, when both active material and carbon are expected to participate in conductive network formation, instead of plotting composition in terms of either silicon or carbon, it can be useful to consider a new parameter, *i.e. volume fraction of total conductive solids*. The entire data set for 121 cases with silicon conductivity switch on, is shown as a scatter plot in Figure 5.13 with a two term exponential (second order exponential fit). In order to account for decreasing capacity as silicon content is increased, it can be more useful to fit the data with a second order exponential rather than a power law. When considering a slurry without carbon as in Figure 5.10(a) or turning the conductivity of carbon off, as in Figure 5.14(b), the curve resembles the second order exponential.

The previously mentioned study by Parant *et al.*[84] also studies the sensitivity of acetylene black as a carbon additive which shows neither sigmoidal behavior nor a plateau in conductivity within the range studied.[84] The conductivity of acetylene black is seen to increase linearly from 1 v% and is attributed to filamentous aggregates where the clusters are fractal-like, possibly arising from diffusion limited aggregation mechanism. Mathematically, this region represents the linear part of the exponential function, where growth is steady. As an analogy, it can be said that for a slurry where both active material and carbon participate in network formation, the conductivity of the slurry is observed to grow linearly at low solid concentrations, which is attributed to the percolation region. It then reaches a peak and the saturation curve has a downward slope, thus an optimal composition is expected since any further increase in solid content would not only result in poorer capacity but would also compromise the fluidity of the suspension. It can further be said that based on the population and electronic conductivities of active material and conductive carbon, there would be a competition between sigmoidal and second order exponential behavior for conductivity.

At this junction, it is reasonable to assume that the behavior of capacity or conductivity as a function of composition reflects the mechanistic details of network formation. Very large differences in particle size, which are not captured in this model, may also lead to other nuanced behavior and require other types of mathematical fitting to conductivity trends. Within this model it is assumed that nanoparticles, with very large surface area, may aggregate and not play as significant role at the mesoscale. Other particle properties, like surface functional groups

would manifest as interparticle sticking coefficients which can result into the formation of new entities which are larger in diameter and can thus impact the kinetic rate of particle motion and network formation. New algorithms are being prepared in-house to take a sticking coefficient into account, however, in context to the results of this version of the model, it is assumed that all particles simulated are entities which are a result of aggregation and are only likely to hit-stick-and-go instead of remain attached to another entity.

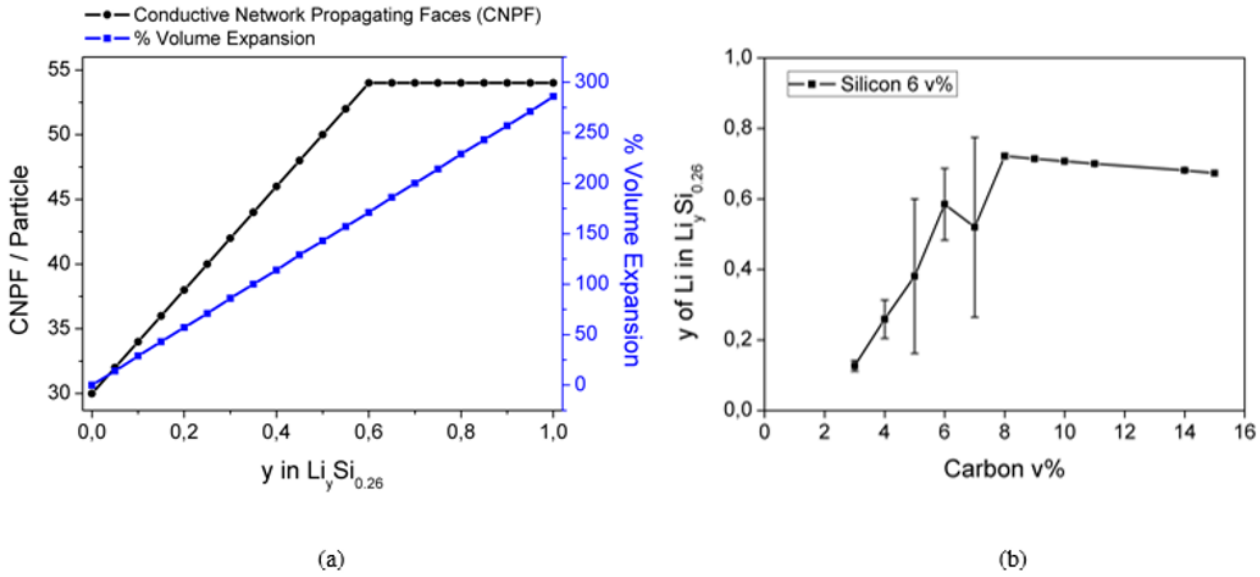

Figure 5.14 (a) The number of conductive network propagating faces (CNPFs) and volume expansion of a silicon particle as a function of state of charge (b) Behavior of slurry with carbon particles that do not participate in network formation.

Another interesting property of silicon particles considered within this study is the growing particle size which may impact how networks evolve within the suspension. Considering the simplest case, where face-to-face contact between neighboring particles is needed for electronic conduction, a single carbon particle provides 6 faces, while a silicon particle would provide a wide range of number of faces based on its state of charge, as shown in Figure 5.14. Here, the y-axis indicates the number of conductive network propagating faces (CNPFs) and how they evolve with the volume expansion during discharge, starting from 30 faces to 54, plateauing at 54

beyond 60% discharge. A 5 to 9 fold increase in potential nodes for branching is expected to significantly influence fractal dimension of conductive networks and can potentially influence the threshold for conductive networks. This suggests that based on the types of electronically conductive particles available, in terms of particle shape and particle size, the threshold for conductive networks will change. A constant growth in the number of faces available to propagate networks is also expected to contribute to overriding the initial slow growth seen in sigmoidal curves. This phenomena, mathematically, is reminiscent of the constant growth mechanism seen in diffusion limited aggregation of acetylene black, as reported by Parant *et al.*[84] Additional studies can be conducted to verify the sensitivity of network propagation to rate of increase of CNPFs and by varying extent of volume expansion permissible.

Table 5.3 Selected cases from the 242 simulated to create a global landscape.

#	Si (%)	C (%)	σ	Total Conductive Solids (%)	y of Li in $Li_ySi_{0.28}$	Conducting Network (%)
1	15	4	0	4	0.09	9
2	3	4	1	7	0.21	15
3	3	8	0	8	0.22	16
4	3	10	0	10	0.57	43
5	5	6	1	11	0.67	61
6	5	12	0	12	0.76	61
7	3	10	1	13	0.79	80
8	3	14	0	14	0.79	86
9	10	6	1	16	0.71	93
10	10	16	0	16	0.71	93
11	15	18	0	18	0.67	96
12	15	4	1	19	0.67	94

In light of the extensive parameter sensitivity study performed with 242 cases simulated in the previous section and the introduction of a new mesoscopic metric, *volume fraction of total conductive solids (TCS)*, there is sound basis for creation of a global landscape, along the lines of a potential energy surface. Table 5.3 summarizes all the data points chosen to cover the entire range of TCSs, with multiple cases for the same TCS to incorporate a variety of cases with regard to silicon, carbon, and conductivity switch. The capacity obtained at the end of each simulation and the average size of the conductive network is also shown in Table 5.3.

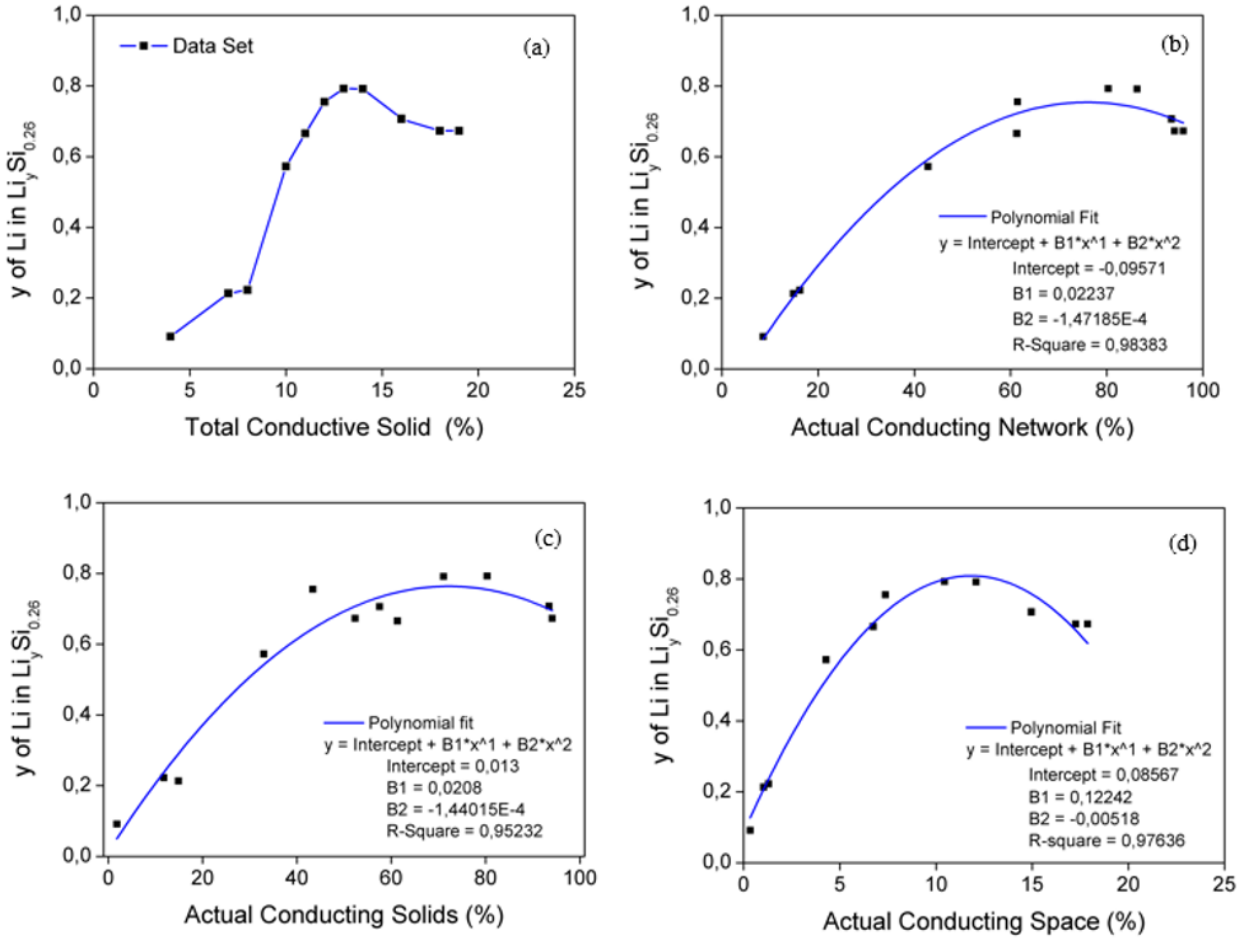

Figure 5.15 (a) Global impact of conductive solid material on capacity, (b) actual conductive network obtained from a product of total conductive solids and percentage of particles forming network, (c) percentage of volume occupied by the conducting solids, and (d) percentage of total solids present in slurry which are conducting.

Based on the parameters mentioned in this table, three new, emergent, mesoscopic metrics are calculated and plotted in Figure 5.15 with reference to capacity. All these figures may be obtained more accurately from the simulation on-the-fly, however, post analysis also provides a reasonable proof of concept. First of all, the global landscape can be seen in Figure 5.15(a) which plots TCS versus capacity. The first half of the behavior is sigmoid-like, while the second half appears to loosely reflect a second order exponential. This clearly suggests that sigmoid

behavior is dominated by carbon particles since such low TCS fractions may not be achieved in the presence of large conductive silicon at this simulation scale. The next mesoscopic metric is the *actual conductive network*, shown in Figure 5.15(b) which is estimated by multiplying TCS with the percentage of particles participating in the conductive network, since not all particles can participate in the network. *Actual conducting space* is shown in Figure 5.15(c), a parameter that estimates how much of the total volume of the slurry or simulation box is occupied by the actual conductive network. *Actual conducting solids*, shown in Figure 5.15(d), is obtained by dividing TCS by the sum of all solid material regardless of whether or not it conducts and then multiplying it by the percentage of particles in the network.

While actual conducting solids may appear similar to the actual conducting network, the former takes into account non-conductive solid material as well, providing a distinction between a slurry in which all the solid conducts and one in which only a part of it can conduct, even if their TCS and percentage of particles in network is identical. This allows for a certain amount of deconvolution between data points that are too close to each other in Figure 5.15(b) and (c). The concept of actual conducting solids can be visualized in yellow in Figure 5.16, (a) represents what is captured by the model, (b) how it is visualized at the particle level, and (c) at the slurry level.

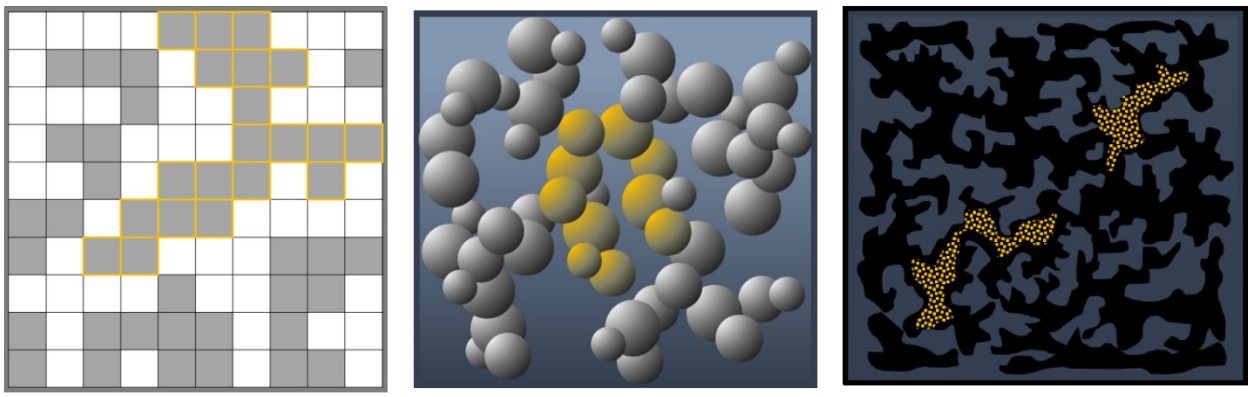

Figure 5.16 Representation of actual conducting solids as seen in (a) the model, and schematics for visualization at (b) particle level and (c) clustered fluid level.

The visualization of slurry as a clustered fluid phase was reported by Hipp *et al.*[88,89] from simultaneous Rheo-uSANS (ultra-small angle neutron scattering) and spatiotemporally resolved Rheo-SANS (small angle neutron scattering) measurements.[89] Furthermore, a study by the same group which combined SANS, oscillatory rheology, and impedance spectroscopy, reported that rather than conductive networks, cluster size is a far more significant parameter impacting conductivity.[88]

Therefore, with the cluster identified as an important entity, finding a means to assign effective properties, can provide useful insight. The trends observed in Figure 5.15 (b)-(d) all fit to second order polynomial equations. The advantage of these metrics is that aside from a simple conductivity-carbon content plot, metrics like the actual conducting solids can help identify suitable slurry compositions faster by helping narrow down candidates. While it may not be intuitive to obtain these mesoscopic metrics directly from experiment, new simultaneous measurements that incorporate electrochemistry and rheology is a new domain which can provide numerous possibilities as mentioned in Chapter 2. A notable means to reconstruct clusters using synchrotron radiation X-ray tomographic microscopy has been reported by Hatzell *et al.*[164] in the context of semi-solid flow capacitors.

5.2. Conclusions

This chapter provides a case study for a simple assumption, *i.e.* how the participation of silicon particles in formation of conductive network can impact SSRFB discharge behavior. For this purpose, an on-and-off switch for silicon conductivity was introduced to the algorithm. In addition to impacting the phenomena of network formation, it was assumed that electronic conductivity of silicon increases on lithiation, and it would also impact the rate of lithiation itself. Section 5.1.1 shows how to systematically add a new feature to the model, by studying its response for four different slurry compositions (silicon content 6 v%, 14 v% combined with carbon content 5 v% and 13 v%). While the impact of an evolving lithiation rate remains to be further studied, it was observed that the impact of participation of silicon in conductive networks was most evident when carbon content is insufficient

to form networks by its own. While this result is intuitive, the evolution of conductive networks and the particle size distribution shows four distinct morphological behaviors in the slurry. These can be used as tools to characterize and explain other results as well as provide a qualitative picture of some experimental results in literature. Section 5.1.2 further explores the impact of the conductivity switch in context to perturbations in simulation box size and C-rate at different compositions. The parameters varied here are carbon content (5 v%, 13 v%), silicon content (6 v%, 14 v%), C-rate (1C, C/20), simulation box depth (20, 25, 30, 40, 45, units). It was seen that regardless of C-rate, increasing depth resulted in a decrease in discharge capacity. However the role of silicon content, regardless of the conductivity switch, was less intuitive. Results suggested that it may play both, a constructive and disruptive role for the conductive networks. Multi-parameter sensitivity studies from experiments were discussed in this context and it was demonstrated how complexity and non-intuitiveness in experiments arise from competition between multiple phenomena.

A large PSA study for exploring the impact of the conductivity switch on slurry compositions is reported in Section 5.1.3. The 121 compositions made from combinations between silicon content (3, 4, 5, 6, 7, 8, 9, 10, 11, 14, 15 v%) and carbon content (0, 2, 4, 6, 8, 10, 12, 14, 16, 18, 20 v%). The nature of the capacity versus carbon content trend is sigmoidal when the conductivity switch is off and a second order exponential when the conductivity switch in on. This study provides a means to access several states of the system and is essentially a global parameter sensitivity study. This further offers the possibility of creating a global picture, along the lines of a potential energy surface, to explore how the capacity is influenced by solid content within a slurry, regardless of extent of participation in network formation. The results from this analysis show that it is possible to create a landscape taking multiple aspects like composition and operation conditions into account, to create a comprehensive toolkit to choose a system optimum. This has been made possible by the introduction of several new mesoscopic quantities which allow bundling of lower scale parameters into usable metrics, for instance, total conducting solids, actual conducting network, actual conducting space and actual conducting solids. These parameters provide means to categorize the clustered slurry phase based on the ratios between solid, liquid and electronically active and in active, simultaneously. While it may be challenging to obtain direct validation for such

metrics, recognizing their utility can help extract more from information from upcoming and new experimental techniques being used which study multiple phenomena simultaneously. Additionally, creation of new metrics for a given system or adoption of metrics from other disciplines to deepen understanding of a system, have proven to be useful, for instance, the introduction of capacitive Damköhler number as mentioned in the state of the art.[93]

Chapter 6

Overview of Complexity

6.1. Perspectives on handling phenomenological complexity in SSRFBs

A classification of the input parameters used in the mechanistic model described in this work are color coded to provide an indication of the kind of information they can provide in Table 6.1. Here the grey color suggests which correlations can be incorporated more explicitly in the future.

Table 6.1. List of parameters used and how they can capture different phenomena. Colors blue, orange, green depict parameters included in the model for electrochemistry, particle dynamics, and rheology, respectively. Grey color indicates which parameters can be incorporated in future work.

	Electrochemistry	Particle Dynamics	Rheology
Electrode Composition			
Solid Volume Fraction			
Viscosity of Slurry			
Mesostructure			
Percolation Threshold			
Electrode Conductivity			
Particle Conductivity			
Li salt Conc.			
Solid Si Conc.			
Lithiated Solid Si Conc.			
Viscosity of Electrolyte			
C-rate			
Exchange Current Density			
Transfer Coefficient			
Margules Coefficient			
Temperature			
Nernst Potential			
Standard Potential of Si			
Overpotential			
Reaction Constant			
State of Charge			
Particle Surface area			
Particle Density			
Particle Diffusion			
Si volume changes			
Particle Radius			
Kinetic Rate			
Time Step			

In light of the emergent mesoscopic parameters identified in Chapter 5, which play an important role in providing generalized concepts, it is relevant to explore fundamental knowledge pertaining to the disciplines to which the SSRFB belongs. The following sub-sections briefly discuss all possible phenomena that arise within electrochemically active particles suspensions in the context of lithium ion batteries, in order to create a mind-map as an aid to handle complexity and eventually apply rigorous tools like graph theory in the future.

6.1.1. Relevant phenomena in particle suspensions

SSRFBs, wherein the electrode is *semi-solid*, consist of high concentrations of solid particles in suspension. These high solid concentrations exacerbate the consequences of many-body interactions and complexity in SSRFBs and simple electrostatic repulsion may not always be enough to maintain a stable colloidal suspension. Additionally, the particle size distribution of active material and conductive carbon generally lies within nanometric range for maximizing electrochemical performance. Thus, the combined effect of high solid fraction and small particle size, in the absence of steric hindrance, can encourage particles to aggregate.[13] Attractive colloidal forces can manifest at two levels; formation of clusters and mesoscopic particle networks.[14] While particle contact is necessary for electronic conduction in the multiphase electrode, too much aggregation can result in sedimentation or flocculation and can render SSRFBs inactive. Flocculation of particles is probable if the liquid medium consists of ionic species which are usually present in high concentrations in battery electrolytes. DLVO theory for colloidal stability is typically used to capture particle interactions and their tendency to aggregate by considering van der Waals forces of attraction and electrostatic repulsive forces of double layers.[13,15–17] The theory has shown to provide useful qualitative explanations of the effect of ionic strength on particle behavior of slurry electrodes.[18] However, to rigorously use DLVO for SSRFBs, one may need to consider on-the-fly coupling with undergoing electrochemical dynamics that are known to significantly impact particle surfaces.

Table 6.2. Dimensionless hydrodynamic numbers for colloidal suspensions[19]

Schmidt	$\frac{\text{collisional momentum transport}}{\text{kinetic momentum transport}}$	$\mathrm{Sc}=\frac{\nu}{D_f}$
Mach	$\frac{\text{flow velocity}}{\text{sound velocity}}$	$\mathrm{Ma}=\frac{v_s}{c_s}$
Reynolds	$\frac{\text{inertial forces}}{\text{viscous forces}}$	$\mathrm{Re}=\frac{v_s a}{\nu}$
Knudsen	$\frac{\text{mean free path}}{\text{particle size}}$	$\mathrm{Kn}=\frac{\lambda_{\text{free}}}{a}$
Peclet	$\frac{\text{convective transport}}{\text{diffusive transport}}$	$\mathrm{Pe}=\frac{v_s a}{D_{\text{col}}}$

Table 6.3. Time scales relevant for colloidal suspensions[19]

Solvent time scales	
Solvent collision time over which solvent molecules interact	$\tau_{\text{col}} \approx 10^{-15}$ s
Solvent relaxation time over which solvent velocity correlations decay	$\tau_f \approx 10^{-14}-10^{-13}$ s
Hydrodynamic time scales	
Sonic time over which sound propagates one colloidal radius	$t_{cs}=\frac{a}{c_s}$
Kinematic time over which momentum (velocity) diffuses one colloidal radius	$\tau_\nu=\frac{a^2}{\nu}$
Stokes time over which a colloid converts over its own radius	$t_S=\frac{a}{v_s}=\frac{\tau_D}{\mathrm{Pe}}$
Brownian time scales	
Fokker-Planck time over which force-force correlations decay	τ_{FP}
Enskog relaxation time over which short-time colloid velocity correlations decay	$\tau_E=\frac{M_c}{\xi_E}$
Brownian relaxation time over which colloid velocity correlations decay in the Langevin equation	$\tau_B=\frac{M_c}{\xi_S}$
Colloid diffusion time over which a colloid diffuses over its radius	$\tau_D=\frac{a^2}{D_{\text{col}}}$
Ordering of time scales for colloidal particles	
$\tau_{\text{col}} < t_f,\ \tau_{FP} < \tau_E,\ \tau_{cs} < \tau_B < \tau_\nu < \tau_D,\ t_S$	

An additional aspect to consider is Brownian motion, which can be significant because the size of particles relevant for battery applications would also satisfy the condition of a Brownian particle. In this case, parameters like solid concentration, slurry viscosity, temperature, diffusion coefficient of particle, Peclet number, or Reynolds number can impact the degree of Brownian motion of the particles.[19] Tables 6.2 and 6.3 provide a list of dimensionless numbers and time scales relevant for colloidal suspensions.

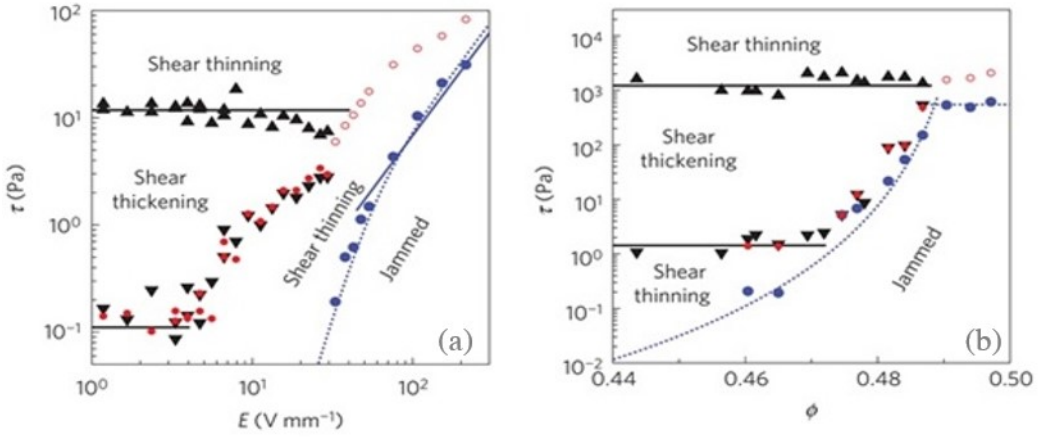

Figure 6.1. Non-equilibrium phase diagrams delineating observable shear-thickening regions in terms of the associated stress range. Stress range as a function of (a) applied electric field E and (b) packing fraction.[20]

However, even suspensions containing non-Brownian particles show a variety of highly complex phenomena due to non-Newtonian and viscoelastic behavior. For instance, shear thinning behavior is a result of disintegration of pre-existing particle networks, allowing the suspension to flow more easily. This, however, can mask a shear thickening regime, wherein the suspension starts forming new particle networks and inhibits flow, which would eventually impact operation of SSRFBs. The shear thickening regime can be briefly revealed under a certain range of shear rate based on parameters like particle size distribution, particle aspect ratio, inter-particle interactions, and even electric or magnetic fields for systems susceptible to these forces (Figure 6.1).[20,21] On increasing solid volume fraction, the suspension can also enter a jammed regime where the particle assembly leads to complete arrest; this would be highly disadvantageous for flowing electrodes.[20] Regimes of shear thickening and jammed clusters have only recently been unraveled in SSRFBs.[5,7] If the mesoscopic intricacies of such

electrochemically evolving suspensions are better understood, mechanical pumping losses associated with SSRFBs would be minimized and particle connectivity could be enhanced.

6.1.2. Relevant phenomena in lithium ion batteries

According to Aurbach *et al.,*[22] the short lifetime of post-LIB systems lies in: (i) instability of crystallographic phase transition of active materials and (ii) uncontrollable reactions at the interface of active material and electrolyte leading to unstable solid electrolyte interfaces (SEI). Additionally, material optimization is specific for commercialization of a given battery; this means that the same material would have a tendency to behave poorly when used in a new type of battery. The general term, *battery performance*, is known to be influenced by mass transport limitations, kinetic limitations arising from electrochemical charge transfer, and ohmic or resistive contributions within the battery. Here, overpotential, quasi-static hysteresis, and rate capability limitations also play a role.[23] Ageing of a battery is captured as the progressive capacity loss and an increase in internal resistance, eventually leading to voltage fade and power loss.[24,25] To construct an overarching understanding, all these phenomena can be generalized under one umbrella, *i.e.* important aspects frequently encountered when studying new battery materials or systems. From a phenomenological point of view, it becomes convoluted to assign specific mechanisms to every performance metric because of cascade effects that can impact the entire battery (Figure 6.2).[24] For instance, parasitic reactions on either electrode can manifest as increased thickness of SEI which leads to increased resistance, consumption of electrons and ions, impact on coulombic efficiency, loss of lithium or even host site, and consequently loss of capacity.[25–29] If the active material host lattice irreversibly transforms along cycling, lithium transport and lithium storage can be impacted, contributing to thermodynamic changes that may appear as hysteresis or voltage fade; furthermore, mechanical disintegration of particles can lead to capacity loss.[23,29–36] The existence of these specific pathways is nearly impossible to isolate and prove experimentally even in highly optimized and commercialized LIBs;[25,27] this inadvertently reveals the complexity of the battery system.

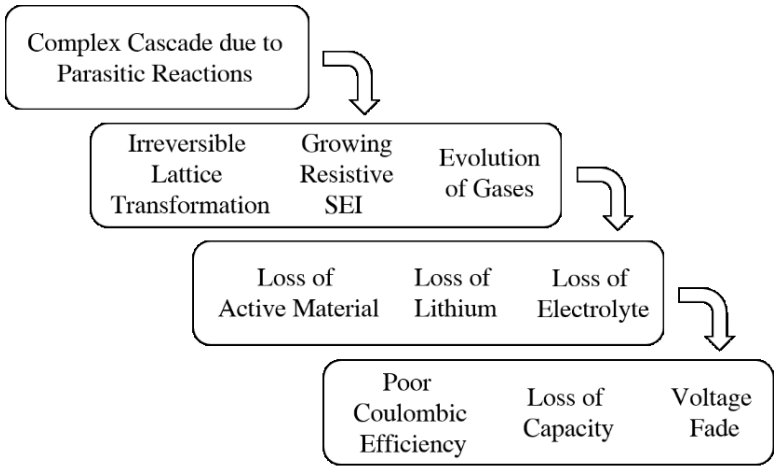

Figure 6.2. A simplified representation of cascading effects of side reactions in a battery across time and scale. Numerous feedback loops can exist between these phenomena.

While it may seem reasonable to reduce the scale of a problem by eliminating insignificant mechanisms, this may not be possible in such interdependent systems. For instance, the presence of anionic redox activity was never established in conventional layered cathode materials and remained a source of confusion because numerous explanations were provided for side reactions involving host anions.[31] However, when lithium rich cathodes showed a dominating presence of anionic redox activity, this phenomenon was systematically studied and controversies were put to rest across oxide based layered material families.[37] Another instance is the nucleation of a new phase which is said to be determined by the surface to volume ratio of a particle, however, literature of phase changes on ion insertion is also quite complex.[38] The model cathode material, $LiFePO_4$, was initially touted as a material with low rate capability because of kinetic barriers to lithium diffusion originating from phase boundaries.[39] It was soon demonstrated that decreasing the particle size had a more significant impact on the electrode resistance than introducing a carbon coating.[40] Interfacial energy, surface energy, coherency strains, free energy of mixing, solubility limits of lithium, lithium transport in bulk and on the surface, and lithium insertion kinetics were shown to impact the miscibility gap; determining whether solid solution or phase separation mechanism takes place, and induces complex multi-particle effects like the domino cascade effect.[39,41,42]

Given the importance of surface transport mechanisms in phase changes, SEI and its evolving nature along cycling could also play a role. Many physical aspects influence SEI formation, such as surface catalytic sites, nucleation and growth mechanisms, disintegration, and regeneration.[24,26,43–46] The nature of SEI and how particles interact with each other and with the solvent, is expected to have a direct impact on rheological properties of the suspension which will further be illustrated in the following schematic.

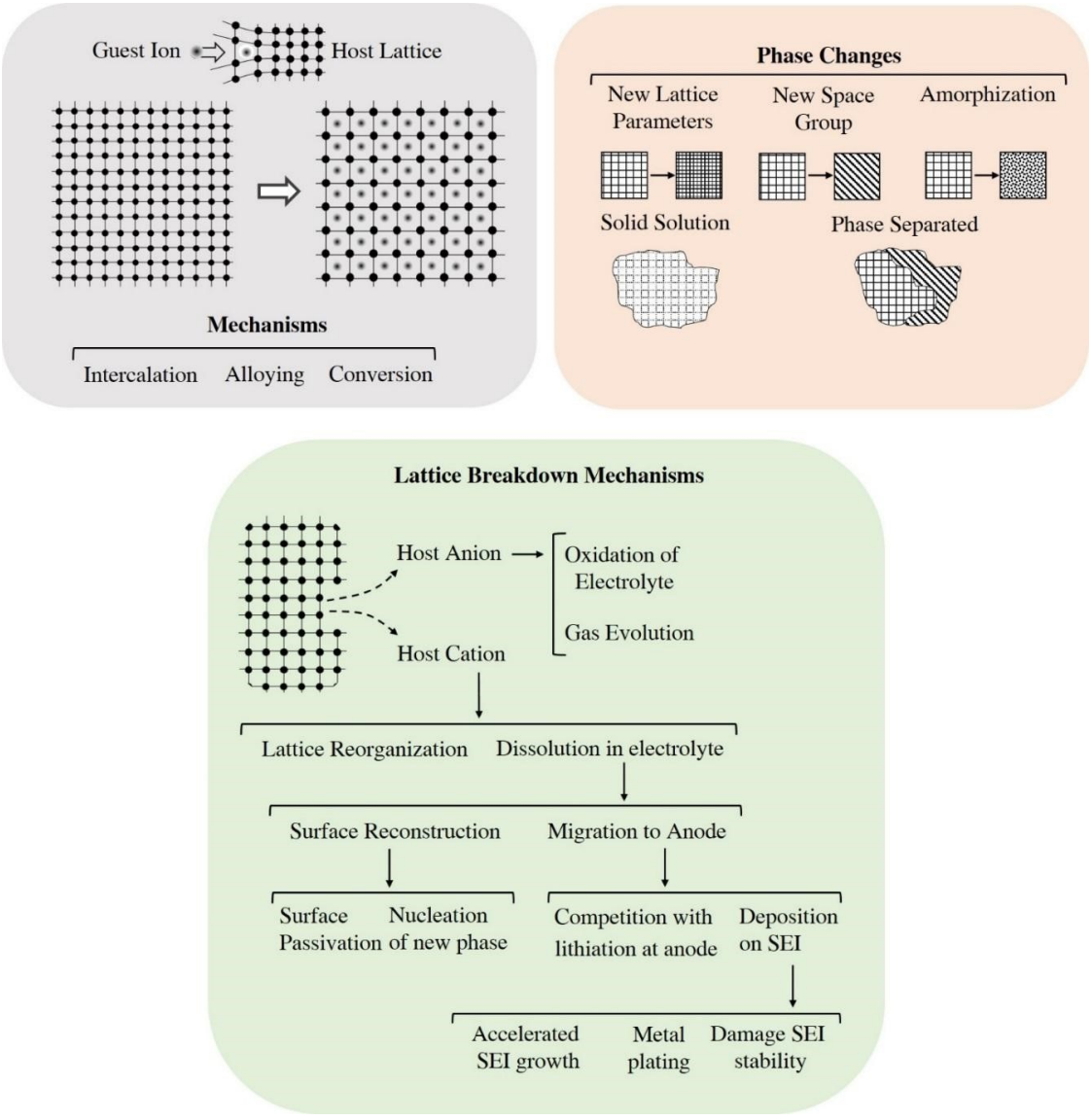

Figure 6.3. Schematic showing a selection of generalized aspects that introduce complexity in batteries[1,24–33,35–46,49–52,52,53,53–77] with reference to active material.

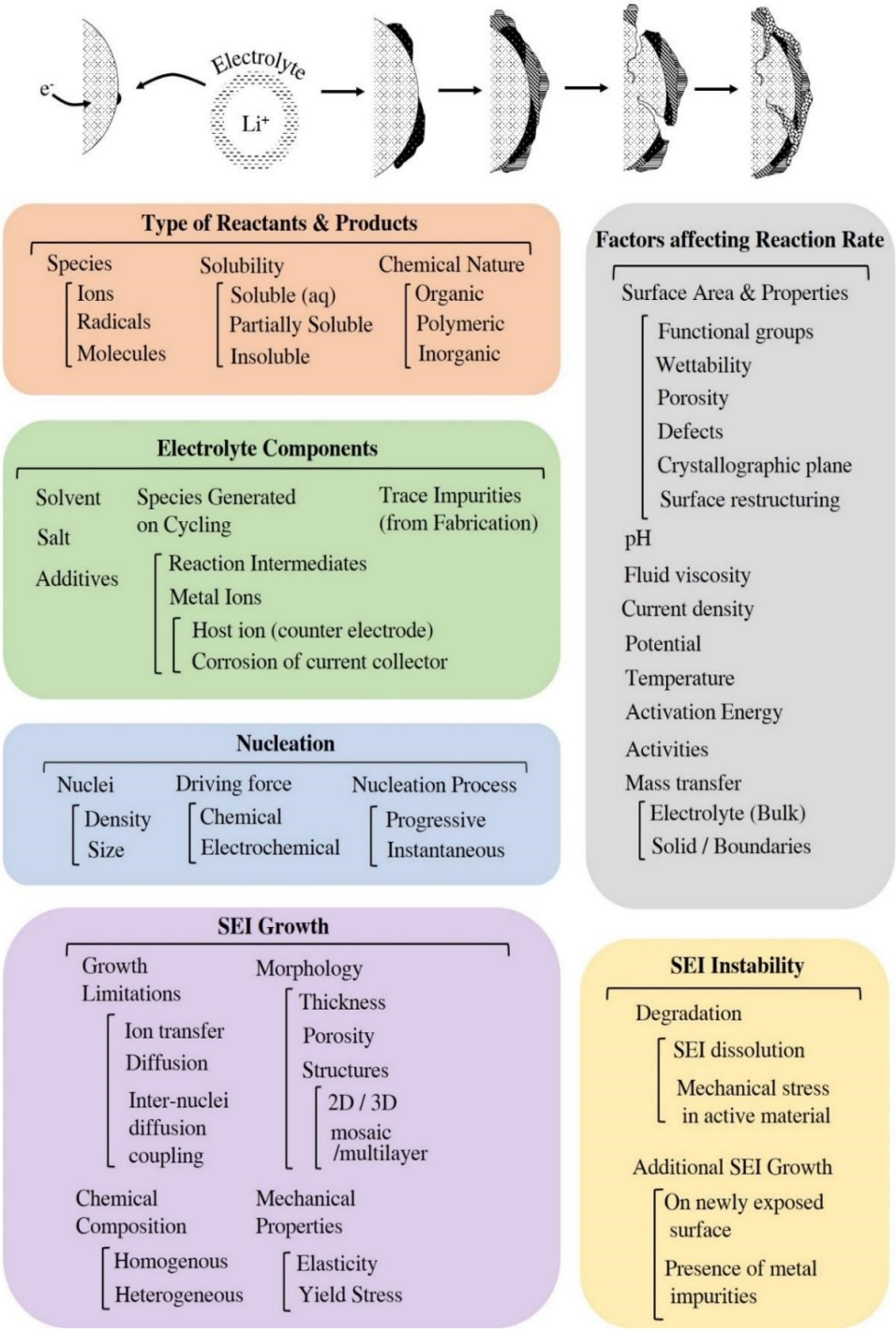

Figure 6.4. Schematic for phenomena linked to solid electrolyte interface (SEI) on the surface of active material. Feedback loops between categories shown here are difficult to visually demonstrate but are intended implicitly [1,24–33,35–46,49–52,52,53,53–77]

Grain boundaries are another subject of complexity; they are known to possess higher crystallographic disorder and their ion migration barrier can either be low[36] or high[47]. Even in the absence of grain boundaries, two-way diffusion processes on cycling have shown evidence of lithium trapping in alloying electrodes and current collectors.[48] Evidently, grain boundaries can significantly influence resistance regardless of whether they are present in polycrystalline active materials or within the SEI.[36,44]

A collection of some parameters and phenomena linked to phase transitions and SEI are presented in Figure 6.3 and Figure 6.4. Viewing the phenomenological landscape as a collection of all mechanisms can help identify conditions when otherwise masked mechanisms begin to dominate. Organizing and summarizing this vast number of phenomena in literature is especially challenging with regard to nomenclature and significant effort has gone into providing an exhaustive yet generalized picture.

6.2. Handling complexity in different stages of battery research

Before a new battery technology can be considered for commercialization, its development can be sub-divided into the following milestones (Figure 6.5): (i) An invention or discovery demonstrating proof of concept of new material or device, (ii) primary optimization to create a standardized prototype and gather empirical understanding, (iii) secondary optimization using models for fine tuning to create a bankable prototype. The investment and return at each step is significantly different and worth taking into account. Investment of time and resources is most undefined in step (i), followed by step (ii) and step (iii). While battery behavior is expected to become more and more predictable in successive steps, there is usually no guarantee that a device will be able to pass to the next level or survive the entire journey of innovation to be marketed. Additionally, unless novel techniques are developed for characterization and optimization at steps (i) and (ii), novelty tends to decrease along the steps.

Standardization is a significant bottleneck, because unless precedential state of the art is useful, it relies entirely on human intuition and trial-and-error. Only a few places in the world possess the man power and facilities to implement the high-throughput, brute force, trial-and-error approach, and such requirements hinder battery research globally. The perspective developed in this thesis is targeted towards getting the most out of failed experiments so as to reduce the trial-and-error iterations for the device in question and for all similar devices. Typically, standardization is accomplished by identifying which phenomena impact device performance and how they interact with each other. These relationships between parameters and phenomena allow scientists to fine tune device architecture and material composition. The aim is to create a symbiotic relationship between the phenomena, thus allowing the device to function for a reasonably long period of time, and to possess a quality of self-sustenance. If this state is achieved, it usually means that there are a handful of relationships or empirical equations available, making it elegant and easy to predict how the system will behave. The presence of empirical equations allows systematic optimization of device behavior in step (iii) and traditionally, models are used to assist experiments at this stage.

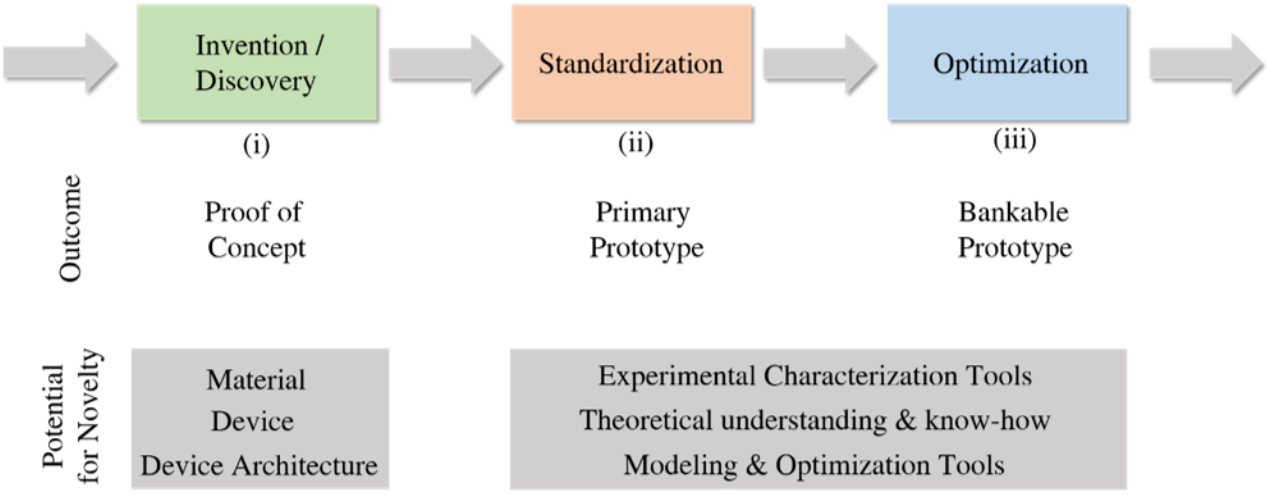

Figure 6.5. Important milestones for battery innovation (i) invention/discovery, (ii) standardization, and (iii) optimization and relevant outcome and novelty of each stage.

6.2.1. Evolution of theory in the face of complexity

Empirical equations are a powerful means to model and predict device behavior, but they may not always be applicable. One of the best examples of how empirical equations fall short, is the rheological behavior of particle suspensions. As seen from the state of the art of experiments for SSRFBs, the presence of shear thinning and shear thickening regimes implies that it is important to predict the equivalent dynamic viscosity for given flow and concertation conditions. Battery researchers are usually concerned with fabricating conventional solid electrode batteries with slurries that are made of active material, conductive carbon, polymeric binders and additives. However, none of these slurries experience electrochemical charging-discharging phenomena. There are, thus, hardly any rheological studies that would help understand SSRFBs better. The following discussion elaborates the manifestation of complexity in particle suspensions, the limitations of empirical equations to address complexity, and possible solutions.

Table 6.4. Formulae for calculating the viscosities of suspensions of solids in liquids.[3]

Equation: (η_m/η_l) =	***Range of Application***
$(1 + 2.5\,\varphi)$	$\varphi < 0.04$
$(1 + 0.5\,\varphi) / (1 - \varphi)^4$	$\varphi < 0.10$
$(1 + 0.5\,\varphi) / (1 - \varphi)^2$	$\varphi < \approx 0.20$
$(1 + 4.5\,\varphi)$	$\varphi < 0.40$
$[1 / \{1 - \varphi^{(1/3)}\}]$	$0.50 < \varphi < 0.90$
$(1 + 2.5\varphi + 7.17\,\varphi^2 + 16.2\,\varphi^3)$	$\varphi < 0.35$
$(1 + 2.5\,\varphi + 10.5\,\varphi^2)$	$\varphi < 0.30$
$[1 + \{2.5\,\varphi / 2(1 - 1.35\,\varphi)\}^2$	$\varphi < 0.50$
$\exp [2.5\,\varphi / (1 - 0.61)]$	$\varphi < \approx 0.40$

The Herschel Bulkley model is commonly used to study rheology; it consists of a few parameters, namely, yield stress, consistency coefficient, degree of non-Newtonian behavior, and experimentally measured shear strain.[2] While it provides a sufficiently rich description of rheology, it does not help identify specific phenomena or their mechanistic details. Previous research on viscosity or interaction potentials, that can explain colloidal stability, has been driven by the search for a unique equation. For instance, in line with Einstein's relation wherein

viscosity is a function of volume fraction of solid in suspension, several expressions with different coefficients were proposed for different ranges of solid fractions (Table 6.4).[3]

However, further studies showed the importance of considering additional aspects like maximum solid fraction within the fluidity limit, particle diameter, particle shape, particle size distribution, viscosity of medium, and shear rate.[4] Interactions between particles or electro-viscous effects, Brownian motion, energy dissipation in gaps between particles, and local fluid flow around anisotropic particles were also identified as relevant phenomena and there are numerous diverging theories, none of which are able to universally capture viscosity.[2] Theoretical approaches based on Kirkwood's molecular theory and molecular dynamics all show large deviations from measured viscosity data.[3] Soon afterwards, it became clear that such empirical relations are oversimplified and cannot provide a generalized equation with wide applicability.[4] This observation, however, is not to subdue the importance of empirical equations, insofar as the assumptions and conditions behind their validity are taken into consideration, such equations are very reliable.

The theory of viscosity or any theory that describes interaction forces in a colloidal suspension, like DLVO, are known to only implicitly capture the vast underlying material complexity. A brief historical account of interaction potentials demonstrates how scientific advancement required theory to be adapted to take into account more explicit details. By 1784, Newton's gravitational law and Coulomb's law of electrostatics had triggered a race to find a new fundamental force that governs material properties[5] and Laplace postulated the first inverse power law in 1806.[6] Decades later, in 1873, the van der Waals force was proposed and its two main assumptions were the presence of attractive forces between particles and that particle volume could not be neglected.[7] Many of the physical phenomena which had been studied in the preceding century, like capillarity, sublimation, and adsorption, could be explained with this theory. Research naturally turned towards predicting the attraction term theoretically along the lines of Laplace's inverse power law. Sutherland generalized attraction to r^{-n} in 1887 (Figure 6.5, Eq. 6.1, where $U(r)$ is the intermolecular pair potential, ε is the energy well depth, and m controls interaction range) and Gustave Mie, for the first time, included a repulsive term in addition to the

attractive van der Waals term; both of which were described generically as r^{-m} and r^{-n}, respectively.[5,8] In the following years, many scientists tried to find a unique exponent for the repulsive term. In 1925, Lennard Jones found that at shorter distances, ions sized like Ar and Ne repelled with inverse power laws of r^{-9} and r^{-11} respectively, while at a larger distance, a better approximation was given by r^{-15} (Figure 6.5, Eq.6.2, where ε is the energy well depth).[9] This line of research appeared to provide scope for endless claims, none of which were proven to be universally applicable. Today, the Lennard Jones potential is often used in simulations when the objective is to model a general class of effects and the only requirement is to have a physically reasonable potential; thereby it is no longer material specific.

Sutherland Potential [Eq. 6.1]

$$U(r) = \infty \qquad r < \sigma$$

$$= -\varepsilon\left(\frac{\sigma}{r}\right)^{m} \qquad r > \sigma\,.$$

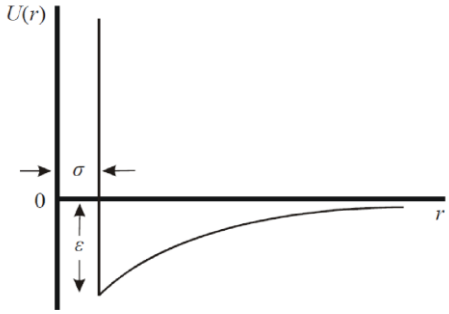

Lennard Jones Potential [Eq. 6.2]

$$V_{LJ} = 4\varepsilon\left[\left(\frac{\sigma}{r}\right)^{12} - \left(\frac{\sigma}{r}\right)^{6}\right]$$

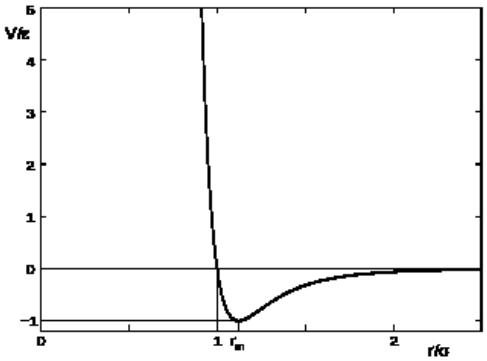

Figure 6.5. Brief descriptions of Sutherland and Lennard Jones (LJ) potentials, the force of repulsion is the main difference, it is infinite for Sutherland, and defined by a power law for LJ.[5]

Quantum mechanics, which was getting popularized in 1920s, offered a more rigorous treatment for the origin of the repulsive term. In 1921, Debye gave a very exact description of molecular forces and showed that the energy of a molecule resulted from the existence of two simultaneous forces, that of attraction and repulsion.[10] In 1925, Pauli stated that two electrons can only exist in the same volume element of space if they have sufficiently different velocity. Thus, repulsion between atoms depended on the electron spin. For cases like unsaturated molecules where electrons can easily change their spin to overlap electron clouds, repulsions exist only for short distances, while for atoms which require very high energy to change their electron spins, repulsions are much stronger.[11] Hence, repulsive forces depend on rather subtle details of the charge distribution of the molecules and it is consequently nearly impossible to connect them with simple constants of molecules, quite unlike attractive terms. Interaction potentials were hereafter expressed as a sum of a variety of attractive and repulsive terms of electrostatic origin, as described by London as follows (Eq. 6.3):[12]

$$U = be^{\frac{-R}{\rho}} - \frac{c}{R^6} - \frac{d}{R^8} + \frac{e_1 e_2}{R} \qquad \text{[Eq. 6.3]}$$

Evidently, the search for a unique force was abandoned and replaced by an approach that took into account as many phenomenological details as possible, and as explicitly as possible.

6.2.2. Exploring Modeling Tools

Historically, the origin of modeling for batteries lies with the development of engineering science in the 1960s, which allowed for mathematical frameworks to systematize the scattered knowledge obtained empirically.[13] A paper on 'engineering design of electrochemical systems' published by J. Newman in 1968 was one offshoot of the interdisciplinary union of chemical engineering and electrochemical science.[14] While continuum models can provide a general guiding framework, they can also be misleading since they are not specifically designed for causal discovery that is needed for standardization of a device. This thesis is strictly directed towards building

modeling tools for standardization, which is an unconventional and new application for modeling. As previously mentioned, complexity is said to arise from a combination of a many-body, many-phenomena and many-scale problem. Examples of modeling tools that can most appropriately handle these problems are shown in Figure 6.6.

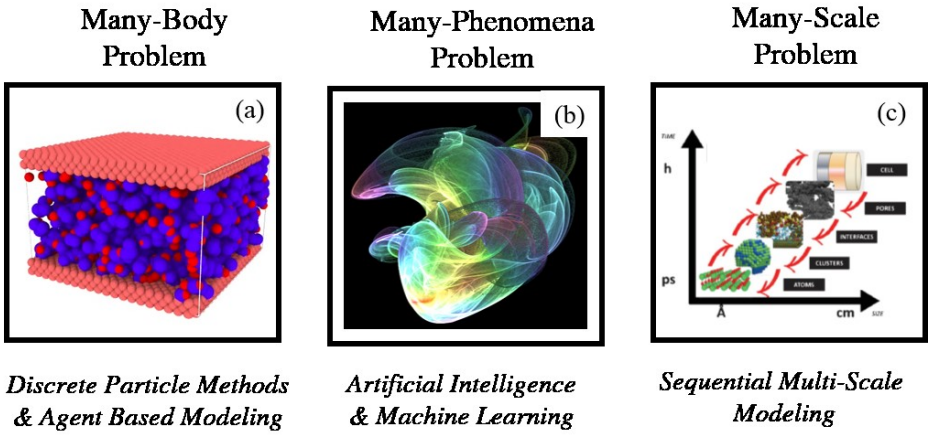

Figure 6.6. When simple empirical relationships cannot be obtained for a system, it is considered to be complex either due to a (a) many-body problem, (b) many-phenomena problem or (c) many-scale problem.[15] *Representative examples of modeling tools used for these respective challenges are mentioned.*

Challenges for the many-phenomena problem come with a combination of many-body and many-scale problem because bodies or entities such as electrons, ions, particles, aggregates, agglomerates, or clusters can interact with each other across scales, making it nearly impossible for a single model to capture and predict all the possible effects. The efforts presented in this thesis demonstrate that not only would a single scale model not suffice, neither would a traditional sequential model associated with multiscale modeling (Figure 6.6(c)). Instead, a variety of combinations of different scales can be incorporated into a collection of interdependent models, as schematically depicted in Figure 6.7. This approach is expected to facilitate the study of the many-phenomena problem. Furthermore, it would also make parameter estimation more reliable by providing a chain of parameter correlations, where some are verifiable explicitly, and others implicitly.

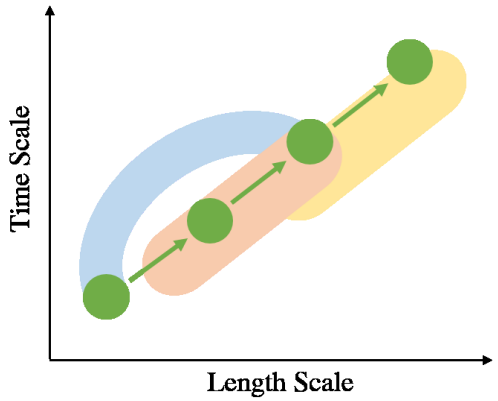

Figure 6.7. New paradigm with multiple, cross scale overlapping and tight multiscale feedback.

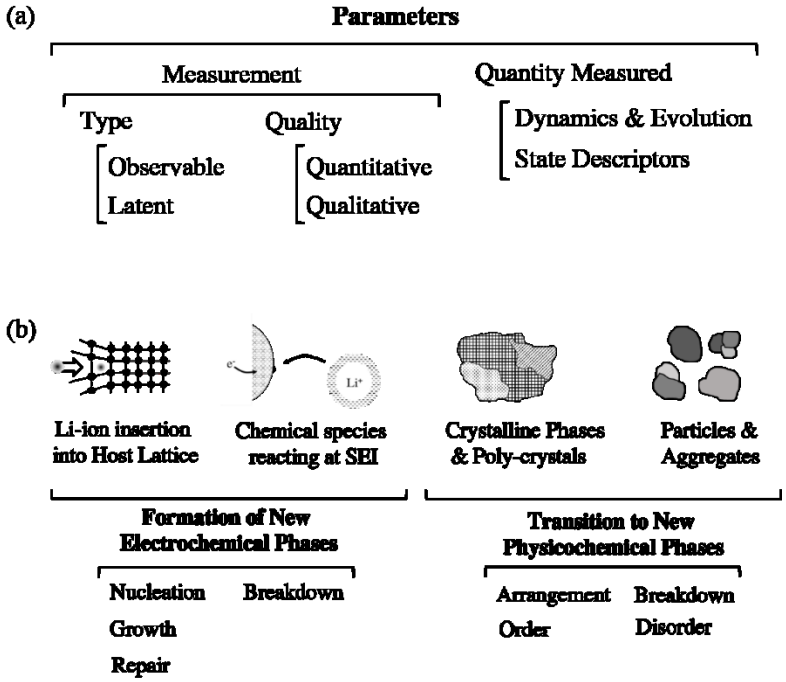

Figure 6.8. (a) A means to classify parameters and their nature in an attempt to incorporate them into a single platform to encourage interdisciplinary interactions (b) Classification of phenomena discussed in Chapter 4 and suggestions on how to categorize their dynamics.

An important premise of the proposed paradigm is that the behavior of a system is difficult to predict only when the understanding of its important parts is either poor or missing. Any system and the dynamics of its interacting parts can be described in terms of state descriptors. These descriptors can either be experimentally observable or latent (*i.e.* need to be inferred). Both these types of parameters can possess varying degrees of quantification (Figure 6.8(a)). Through the development of new experimental characterization tools, especially in-situ and in-operando measurements, more parameters can be experimentally measured. The rest of the latent parameters constitute the reason behind the complex nature of a system. This work demonstrates how the important but often ignored latent parameters lie at the interphases of matter or in the gaps between disciplines and scales. Additionally, Figure 6.8(b) summarizes some of the relevant physical phenomena that are important for SSRFBs.

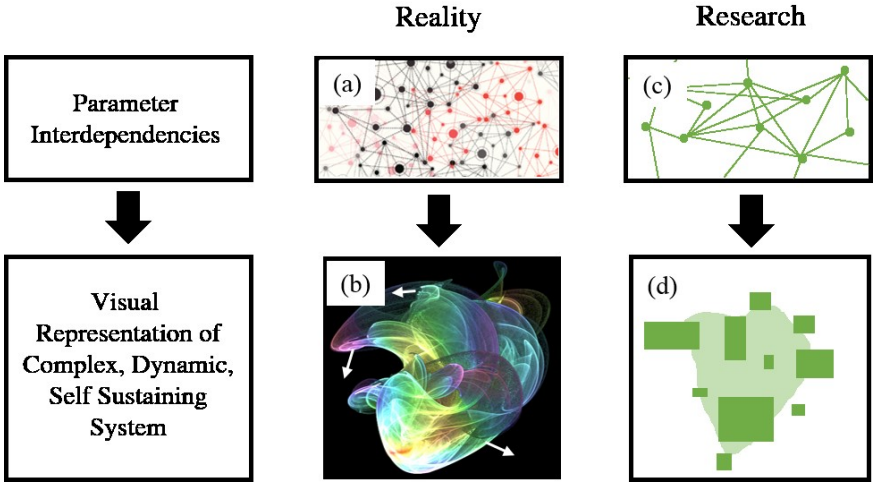

Figure 6.9. Schematics showing how relationships between parameters (a) can be used to visualize system complexity in the form of an attractor (b) and how various tools can be used to approximate reality when experimental characterization data is either unavailable, unreliable or incomplete; which is especially the case for new and upcoming battery technologies.

It is evident that the proposed paradigm, especially with reference to Bayesian networks, resembles artificial intelligence (AI). But while AI treats problems as a black box, the proposed paradigm brings a significantly more open quality. This makes it easy for human intervention since the validity of empirical

knowledge in the context of very new battery systems, like SSRFBs, is still questionable. Keeping some underlying AI principles in mind while developing this paradigm can prove very useful for navigating through the complexity. A recent patent showcases a fascinating unified approach, whereby through the use of non-equilibrium dynamics, it is possible to combine advantages of all five schools of artificial intelligence, namely, symbolist, collectionist, evolutionary, Bayesian, and analogizer.[62]

Non-equilibrium dynamics allows any system to be visually represented as an attractor (as seen in Figure 6.6(b) and Figure 6.9(b)) by considering numerous relationships between parameters (like Figure 6.9(a)). Simply put, an attractor is a complex shape defined by different state values the system can take. If the attractor collapses into a point, the device can be said to be no longer functioning, however if the attractor maintains its shape, the device is said to be functioning and self-sustaining. The limitation of non-equilibrium dynamics is that it is based on the assumption of determinism, *i.e.* all relationships can be accurately captured. However, since the totality of reality is far from mathematically predictable; the attractor must be dynamically evolving due to a mix of deterministic and random forces, as highlighted by small arrows in Figure 6.9(b)), much like a complex adaptive system.[63]

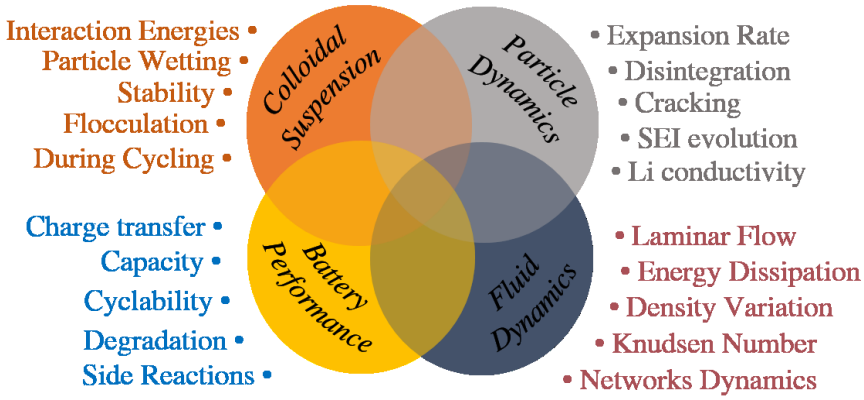

Figure 6.10. An example of how various disciplinary knowledge is needed to correctly model and understand the functioning of SSRFBs.

With the target description of complex reality in mind, this thesis focuses on uncovering relationships between parameters as shown in Figure 6.9(c), using the state of the art knowledge of empirical equations from various disciplines as highlighted in Figure 6.10.

6.3. Conclusions

As elaborated in Figure 6.11, a new paradigm is proposed as a result of this thesis work and it concerns itself with (i) model specification by establishing a basic causal network of a sample system with phenomena selected from a phenomenological master map (Figure 6.11(a)-(b)), (ii) running hypothetical experiments using an adaptive mechanistic model, based on ABM and a kMC engine, to study the behavior under conditions of reduced complexity (Figure 6.11(c)-(e)), and (iii) exploring evolution of standard and special metrics based on variations of simultaneous parameter values (Figure 6.11(f)). Through these steps, it is demonstrated how causal discovery, which is generally intuition based, can be made more rigorous. Furthermore, as established in Chapter 5, the paradigm will need to analyze multidimensional datasets to address complexity.

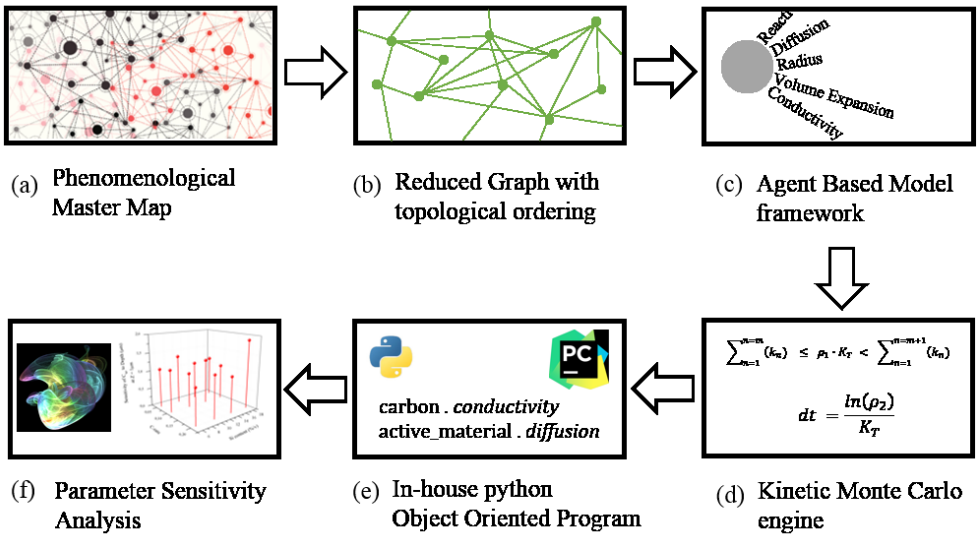

Figure 6.11. Schematic describing workflow proposed for the SSRFB.

Creating a mechanistic model to run a hypothetical experiment, can be referred to as *hypothesizing*, but this is not a new approach, for instance, between, 1905 and 1908, the theory of Brownian motion was treated theoretically by Einstein, Smoluchowski, and Langevin since experimentalists did not know what to measure.[64] However, the difference here is that instead of a hypothesizing the behavior of a single phenomenon or set of phenomena in absolute terms, the objective is to explore what happens when there are multiple poorly understood phenomena competing with each other.

Chapter 7

Summary and Conclusions

This thesis is targeted at providing a tool to aid the trial-and-error based experimental approach typically used for developing electrochemical systems for energy applications. As a device, the semi-solid redox flow battery (SSRFB) provides great potential for exploring how the coexistence of multiple phenomena from different disciplines like rheology, electrochemistry, particle dynamics, and fluid dynamics, manifest. State of the art demonstrates that SSRFBs are prone to showing non-intuitive and conflicting results, making it hard to achieve rapid progress needed for commercialization.

Since literature reports the benefits of discharging the SSRFB under intermittent flow conditions, this work focuses on studying a silicon and carbon based slurry in static mode. While only the coexistence of particle dynamics and electrochemistry at mesoscale are explored in this work, it provides a significantly rich study to demonstrate how the SSRFB is a good example of a complex system. Through the use of a mechanistic model and parameter sensitivity analysis (PSA), and with graph theory as a perspective tool, a new methodology is established. It is used to simulate particles on a discrete three-dimensional grid such that they experience a pseudo-Brownian motion as well as electrochemical discharge through the formation of conductive networks. The mechanistic model is based on kinetic Monte Carlo (kMC) using variable step size method and was developed in-house using object oriented programming in Python. The physics behind the model is based on a selection of the most relevant phenomena at mesoscale, such as particle diffusion calculated from viscosity and particle size, and electrochemistry calculated using Butler-Volmer kinetics which takes into consideration the volume expansion of silicon particles on discharge. This mechanistic model can also be viewed as an agent-based model wherein particles act as free agents that can move through the three dimensional grid and interact with one another.

Since such models are very challenging to standardize and validate, significant effort went into using PSA to explore the features, limitations, and strengths of the model. Implementing a stochastic modeling technique like

kMC and simulating the slurry on a discrete grid resulted in fluctuations in data which varied based on the input conditions. It was demonstrated that complex systems can be best studied by observing the response of the system to perturbations in many different input parameters. Obtaining physically relevant sensitivities through this method helped minimize artefacts coming from the nature of the model. Additionally, it was shown how in a complex system, sensitivity of a parameter p to perturbations in n_1, can be influenced not only by the value of n_1 considered, but also values of other parameters n_2, n_3, n_4 and so on. Therefore, understanding the underlying dynamics between parameters and phenomena was seen to be as important as precisely quantifying the value of a single parameter. This provides an explanation for why experimental studies of complex systems yield non-intuitive results and reductionist approaches to studying the behavior of such a system are very challenging.

To demonstrate the usefulness of this model, a simple assumption was tested, *i.e.* the comparison between a case where conductive networks are formed with carbon alone and a case where both silicon and carbon participate. Clear characteristics emerged from the two cases which were corroborated with experimental literature reporting conductivity versus carbon content behavior. Typically, a percolation threshold is followed by a linear percolation region and a saturation in conductivity. With the introduction of a new parameter, *total conducting solids*, that does not differentiate between silicon and carbon, it was possible to generate a global landscape of discharge behavior as a function of solid content. As a consequence, more metrics could be defined that can characterize a particle suspension based on factors like solid-liquid ratio and active-inactive solid ratio, where solid inactivity can be differentiated as either due to lack of electrical connectivity or due to its inability to conduct electrons. The trends of such metrics show an optimum value, thus providing other aspects that can help identify suitable conditions for obtaining good discharge capacities.

Viewing the field of electrochemical energy storage through the lens of complexity theory further allowed the creation of a mind-map that compiles various phenomena that occur within a lithium ion battery. This is expected to provide an aid to hypothesizing when confronted with conflicting experimental observations.

Appendices

Details of the Models & Experiments Attempted

A.1. Modeling Work

A.1.1. Details of the code written for the mechanistic model

The algorithm was coded in-house in the language `Python` and run on a `PyCharm`, an integrated development environment. The first generation (Gen I) of the code was based on functions which are treated as objects in Python and the package `NumPy` (Numerical Python) to implement the three-dimensional grid as an array object. This code was written by myself and optimized by Master student Diego del Olmo Diaz.

Along with being an efficient multi-dimensional container for data, data manipulation and more advanced mathematical functions like random number capabilities and algebra are possible with `NumPy`. Another Python function used for Gen I was `randint` from `random`, which is an essential engine for choosing a kMC event at random for the Brownian motion behavior of particles. It is to be noted however that the numbers generated herein are pseudo-random. The library `math` was used to carry out calculations using `log, asinh, sqrt, asin, exp` and so on, while `csv` (comma separated values) for writing output files.

The Python code Gen II was written in collaboration with Oscar Xavier Guerrero from Departamento de Química, CINVESTAV, Mexico, in a collaboration. This version of the code implemented more advanced functionalities like `argparse` (Parser for command-line options) to pass arguments and parameters to other functions more efficiently, `configparser` (configuration file parser) to manage reading data from the user input file, `itertools` (iteration tools) for efficient looping, `functools` (tools for higher order functions) to use a decorator like `lru_cache` for functions that are frequently called, `collections` to use `deque` for efficiently handling lists of data and `Counter` for convenient tallies, and `plot` from `matplotlib` with `genfromtxt` from `NumPy` for plotting purposes.

OOP is implemented in Python code Gen II, where a generic class called `Particle` is created, of which silicon and carbon are instances. The class `Particle` has properties (declared as `Particle.Property`) such as material and electrochemical properties like conductivity, standard electrode potential, surface area, surface

roughness, mass, density, volume, radius, and state of charge, and properties relevant for the simulation, such as location coordinates on the three dimensional grid, particles in neighborhood, and electroactive surface facets. This generalized description can allow the use of other active materials and to capture more nuances of particle behavior at meso-scale new properties can be introduced to the class, like the impact of crystallographic changes to conductivity for intercalation compounds, or even degradation and ageing mechanisms that reduce accessible capacity or add resistance. While Gen I uses an array for the 3D grid called `Board` to store particle details and coordinates, it was found that dictionaries listing particles proved to be much faster and is thus implement in Gen II. For speed, a class `Board` was created in Gen II which imports most of the material properties from `Particle` to use for calculations pertaining to kinetic rates for particle motion and electrochemical reactions and incorporates the dictionary called `grid` that lists silicon and carbon objects.

However, given that most experimental parameters are defined for systems studied at bulk scale, describing the same properties at the mesoscale within the confines of the model framework requires introduction of new parameters. For instance, the model includes, the number of facets of unit cells that compose an active material particle that are exposed to electrolyte, a means to track how particle density changes with state of charge and volume expansion, population of particles that participate in percolation networks or are electroactive, and a bank of charge accumulated by particles to implement volume expansion in discrete steps.

A.1.2. Other modeling attempts made

Introduction of fluid dynamics to algorithm was attempted by myself and by master student Kush Chadha, who also attempted to corroborate simulation results from computational fluid dynamics simulations of the slurries under flow conditions. However, due to the early stages of standardization of the model at the time, it was not possible to attain conclusive results. Master student Marouan Handa, attempted to build a Dissipative Particle Dynamics (DPD) model with LAMMPS.[111,165–167] However it became evident that the difference in resolution of

time and space would make it impossible to compare with kMC results, rather it was decided that DPD could act as input for kMC. DPD simulations were run with walls composed of frozen particles (Figure A.1.1), and it was expected that the velocity vectors of the particles would offer velocity profiles. It was not the case, however, and further adjustment of interaction potentials between the particles or larger channel width could yield required results.

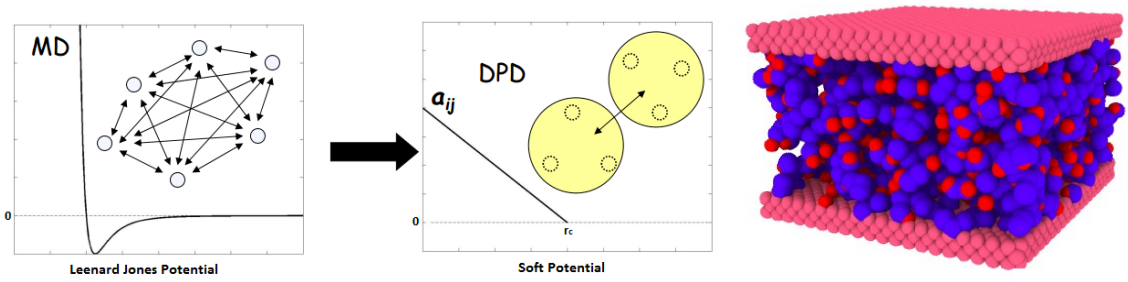

Figure A.1.1. Dissipative Particle Dynamics simulations on LAMMPS, visualized on Ovito, were conducted for simulating flow of the slurry. The interaction potentials used between particles was a soft potential, as opposed to the Lennard Jones potential used in MD.

Furthermore, it was challenging to simulate fluid flow of particles within the on-lattice limitations of kMC, due to development of artificial shockwaves arising from particles getting blocked. Fortunately, a study in literature indicated that artificial shockwaves were satisfactorily removed by an algorithm which passes the rates of the blocked particles to the one in the front of the blocked particle train to force it out of the way.[117]

However, an additional problem was how to incorporate a majority of deterministic phenomena into VSSM, and yet maintain the fundamental role of kMC. At first, fluid flow was implemented simultaneously and independently of the VSSM, but in such a case the pass forward algorithm (PFA) could not be implemented. The envisioned solution is to implement a variety of different deterministic forces on particles so that their motion can be approximated to stochastic behavior, allowing them to be used with PFA within VSSM. This study provided an interesting opportunity to see the challenges faced by cross-disciplinary models. However, as justified within

the text, simulating the slurry in static mode is reasonable since experimental conditions show that intermittent flow mode is more suitable for obtaining high discharge capacities.

A.2. Experimental Work

The following sections briefly describe some of the experimental studies attempted. Since conclusive results were not obtained during the duration of this PhD study, exhaustive details are not provided. The purpose herein is to demonstrate the challenges faced when specialized experimental techniques are not available and procedures have not been optimized through extensive trial-and-error.

Studies with silicon based slurries in organic electrolyte were first attempted by myself, and later, in collaboration with Dr. Emiliano Primo. The silicon particles used in the study were obtained from UMICORE some years prior to this study. Particle size analysis indicated mean particle size of 1.241 μm, specific surface area (BET) of 19.7 m^2/g, oxygen content measured with the Leco method as 2.5 wt%, while TGA analysis indicated 7 % SiO_2 content. Different types of carbons were tested, Ketjenblack EC300J and Ketjenblack EC600JD (Lion), and C45 and C65 (Timcal). Commercial LP30 electrolyte was used with 10 v% FEC (fluoroethylene carbonate).

Galvanostatic discharge of small amounts of slurries within modified Swagelok cells and a larger flow cell (as reported by Hamelet *et al.*[71,72]) was performed. Due to the missing cell parts and challenges with large volumes of slurry, it was planned that a new cell would have to be designed. While many existing designs were studied and a prototype in Teflon was made by Prof. Emmanuel Baudrin; it was challenging to implement a similar cell with compatible tubing for the organic electrolyte. Therefore it was decided that optimization should take place at a lower scale, *i.e.* with Swagelok cells. However, since we strongly suspect that the cell design was inadequate since the capacities obtained were generally below 40 mAh/g for various slurry compositions (in terms of silicon-carbon ratio as well as solid-liquid ratio), the results are not elaborated upon. Whatman fiberglass, Celgard or a combination of both was used in order to minimize the amount of electrolyte absorbed by the

separator. Few varieties of porous copper foams were tested to provide a volume to contain the slurry within the Swagelok cells, some were even compressed to further reduce porosity. Smaller pore size was deemed preferable, however the resulting electrode appeared to be more of a deposit of silicon and carbon on the copper foam, rather than a suspension. Swagelok cells with modified pistons, drilled with cylindrical holes to contain the slurry were also shown to be inadequate as well. It is evident that some breakthroughs could have been achieved with extensive experimental studies, however, due to the lack of standardized conditions available as a starting point, it was challenging to obtain results that could serve as direct support for the model being developed, which was the focus of the PhD grant.

Studies with aqueous based slurries were performed in collaboration with master student Yih-Chyng Wu, under the supervision of Prof. Dominique Larcher. $LiMn_2O_4$ was prepared by grinding Li_2CO_3 and $MnCO_3$ together, heating to 800°C in air for 24h followed by slow cooling to achieve particles as shown in Figure A.2.1.[168] Carbon C45 was used after surface functionalization at 230°C with $(NH_4)_2SO_4$ so as to achieve stable suspension with aqueous electrolyte consisting of $LiNO_3$ (5M, 0.5M).

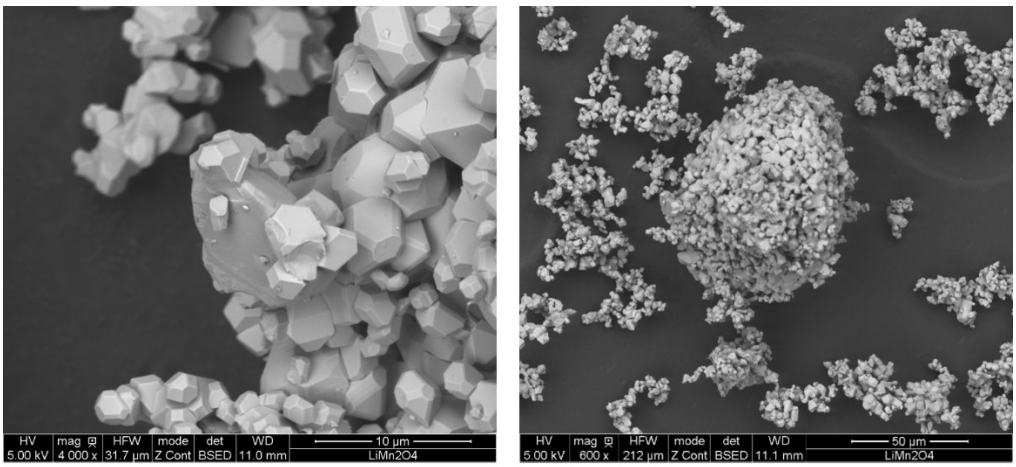

Figure A.2.1. SEM images of the $LiMn_2O_4$ synthesized.

The interest to study slurries in aqueous media was mainly driven by the fact that these experiments could be conducted in open air, unlike slurries in organic media which were prepared inside a glove box. Performing acoustic zeta potential measurements was also of interest, since the instrument available was based on large suspension volumes open to air. However, the lack of standard information available to calibrate the settings for the given suspension made it challenging to obtain useful results.

A.2.1. Slurry Preparation

Various procedures were attempted, including magnetic stirring of solid material in electrolyte after the solids were hand ground with mortar and pestle. Finally, the following procedure was found to be suitable. The slurries were prepared using the set-up shown in Figure A.2.2.

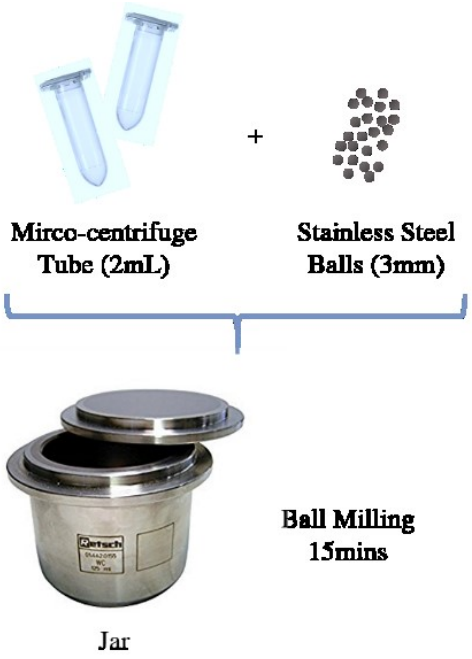

Figure A.2.2. Procedure for preparation of slurry in centrifuge tubes placed inside ball milling jars

Ball-milling was performed within micro-centrifuge tubes with stainless steel balls of 33 mm diameter. This method minimized of wastage of slurry since only small amounts were needed to run tests and ensured that impurities from the ball milling jars were not introduced to the slurry. The tubes containing powders or slurries were placed horizontally in a large ball milling jar and adjusted with packing foam to ensure the tube was held stationary. The jar was then placed in a planetary ball miller at 400 rpm for several minutes alternating direction ever few minutes. The solid content was first ball-milled, followed by the slurry, to ensure maximum homogeneity. Many ball-milling settings were tried and it was observed that 1h of milling produced the slurry that was stable for more than a week and showed smaller degree of aggregation, when visually examined. Ascertaining stability of the slurry for such black suspensions was particularly challenging, since visual stability was apparent but we could not ascertain whether or not both silicon and carbon were suspended uniformly.

A.2.2. In-situ TEM

With the objective to experimentally quantify the nature of the mesostructure of particles in the suspension, TEM studies were conducted by Dr. Arnaud Demortière. Some of the numerous open questions are as follows: How is Brownian motion and particle assembly impacted? How does the formation of SEI impact particle assembly? What conditions favour existence or particle aggregates? Are these particle aggregates homogenous or heterogeneous in composition? What is the size of the aggregates? Can we verify the existence of a percolation networks at certain carbon volume fraction based on experimental and modeling papers already published particles? Do individual particles form percolation networks or aggregates? Do shear stresses from fluid flow and collisions break down aggregates or percolation networks? When we apply current to the system, does that significantly change the interaction potential between particles and impact particle self-assembly? Are there any conditions that would induce flocculation or sedimentation of the solid in the electrode? Can we observe and quantify the nature of Brownian motion particles exhibit? Can we watch the evolution of the system as it discharges by conducting in-situ discharging?

The TEM sample holder as shown in Figure A.2.3 is equipped with a specialized e-chip that can handle liquid samples in static or flow mode. The slurry was prepared by the procedure mentioned in the previous sections, in the glovebox, and then loaded into an air-tight syringe. While preparing the sample, the slurry was briefly exposed to air since the e-chip is very difficult to handle inside a glovebox. It was particularly difficult to have a perfectly sealed e-chip due to its small size and the need to assemble it under the microscope.

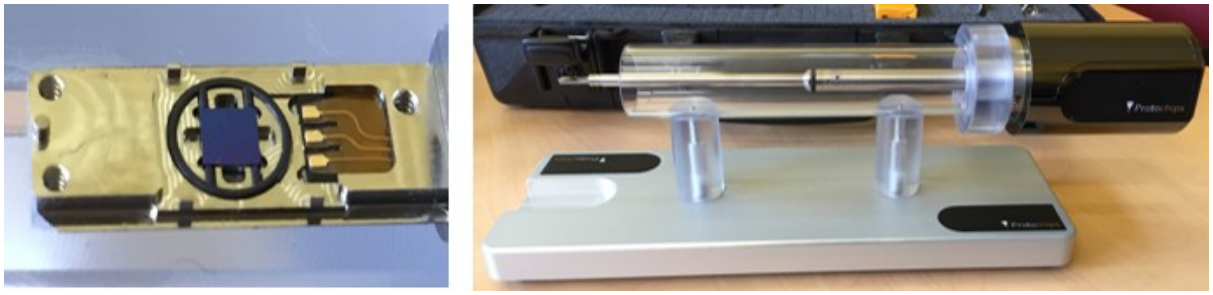

Figure A.2.3. The specialized e-chip and sample holder capable of performing in-situ TEM experiments under static and flow conditions

Attempts were made to study the slurry in static mode, in flow mode, and perform cyclic voltammetry. Figure A.2.4 (a) shows a standard TEM image of a sample slurry, where the larger spherical particles are silicon and the smaller particles are carbon C45. The composition of the slurry tested was 0.5:0.5:64 by mass for Si:C:electrolyte. Figure A.2.4. (b) – (d) show the quality of images obtained from the in-situ TEM mode. It is evident that the particles close to the cell window are clearer than those father away, in the bulk of the slurry. Plasma treatment of the cell window is expected to modify its hydrophobic nature thereby preventing particles from becoming immobile and sticking to the window. However the presence of liquid, in this case, inorganic liquid, hinders clarity of resolution deeper into the slurry, so the appropriate conditions need to be found. The blurred shadow of particles in the Figure A.2.4 (b) - (c) suggest presence of densely aggregated particle networks, however the poor resolution inhibits further assessment.

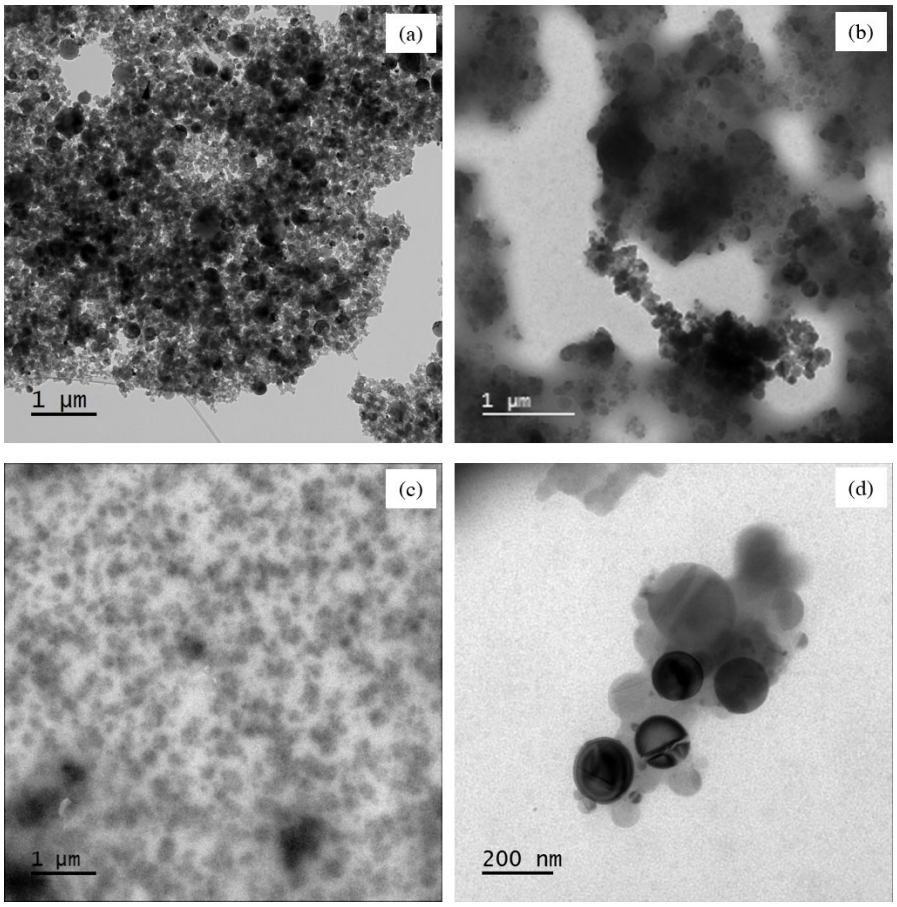

Figure A.2.4. In-situ TEM images of slurry

Dark spots as in Figure A.2.5 (a)-(b), drifting of liquid as in Figure A.2.5 (c)-(d) could be resulting from the impact of the beam on the slurry. Air bubbles in the cell window were another problem as shown in A.2.5 (e), these were observed when the cell was studied in flow mode, it was later found that the o-ring used to seal the cell was not resistant to organic solvents and the entire tubing was found to be blocked with the slurry. It is also possible that despite smaller particle size, aggregate size is large and blocks the piping system. Another phenomena observed was the *blinking* of particles, wherein they would become visible and then disappear in a span of new seconds, as shown in Figure A.2.6 (a)-(b). Extent of blinking was lower for particles associated with aggregates, while particles that appeared to be isolated showed optical effects and significant blinking. While lower density slurries could be studied, they could not mimic experimental conditions of slurry composition appropriate for

standard electrochemical studies. Furthermore, the particle blinking is expected to be a beam effect, affecting particles trapped within the energy well.[169] Beam effects on liquid samples is a new and very poorly understood field,[170–178] thus further studies are needed.

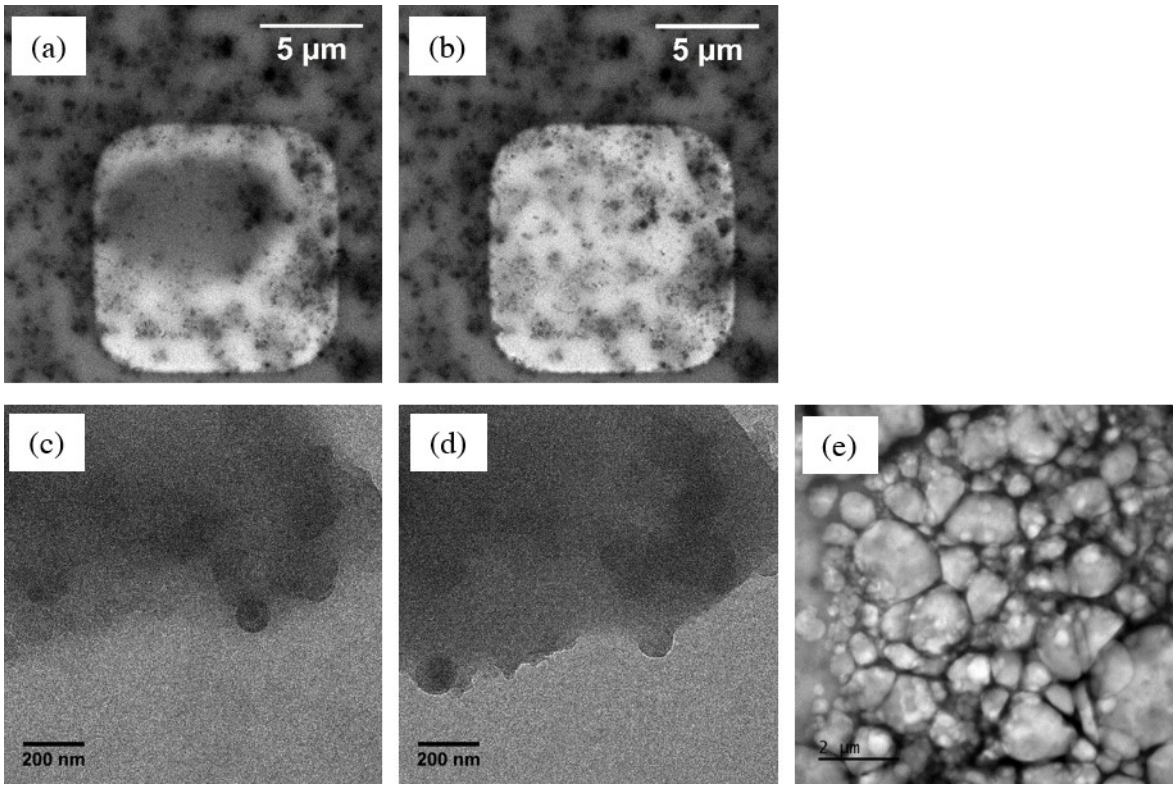

Figure A.2.5 In-situ TEM images of challenges faced

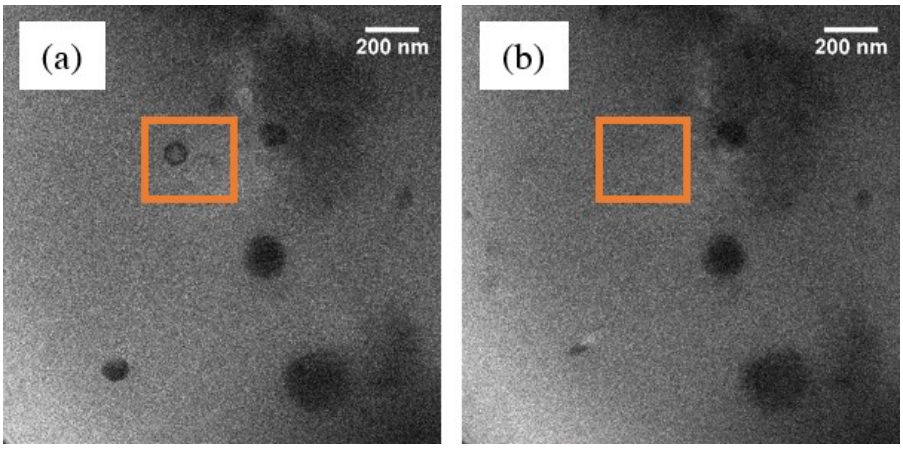

Figure A.2.6 In-situ TEM images showing particle appearing and disappearing, as though bouncing under the impact of the beam

Résumé de la Thèse

Ce travail identifie les défis auxquels sont confrontés les SSRFB. Ils sont attribués au problème des corps multiples où de nombreux phénomènes se font concurrence, à différentes échelles conduisant à un degré élevé de complexité, rendant ainsi les résultats expérimentaux non intuitifs. Ce travail explore l'applicabilité de modèles mécanistes pour gérer ce type de complexité. Le modèle est un modèle tridimensionnel à base d'agents sur réseau comportant un moteur Monte Carlo cinétique. Étant donné que ces modèles sont difficiles à valider, il est proposé d'utiliser une analyse de sensibilité globale des paramètres (PSA). Il a été démontré que l'utilisation de PSA sur de grandes quantités de résultats simulés peut fournir des tendances permettant d'identifier les métriques mésoscopiques émergentes afin de rationaliser la complexité des SSRFB, de telles idées ne ressortent ni des expériences ni des modèles traditionnels. Les perspectives et les outils développés ici peuvent fournir un cadre plus rigoureux pour d'autres types de systèmes électrochimiques situés à l'intersection de disciplines. Un résumé bibliographique des SSRFB du chapitre 2 constitue la base de la complexité du système. Le chapitre 3 décrit le cadre du modèle et une simple calibration pour obtenir des résultats physiquement pertinents. Les chapitres 4 et 5 utilisent une analyse de sensibilité des paramètres pour explorer les caractéristiques du modèle et étudient la sensibilité de la capacité de décharge à la participation d'un matériau actif à la formation d'un réseau conducteur, respectivement. Le chapitre 6 donne un aperçu de la complexité des SSRFB et de ses implications pour proposer des méthodes de travail en perspective. Ceci est suivi d'une conclusion résumant les conclusions de chaque chapitre.

En approfondissant l'état de la technique des SSRFB, il devient évident que plutôt que de brosser un tableau plus clair des mécanismes sous-jacents, les études semblent fournir des explications phénoménologiques basées sur des hypothèses contradictoires. Par exemple, les suspensions à base de silicium et de carbone

maintiennent à la fois un bon et un mauvais contact entre particules lors du cyclage.[72,73] La contribution de l'interface entre le collecteur de courant et la suspension vers la résistance électrique s'avère être à la fois significative et insignifiante.[25,85] Deux écoles de pensée expliquent le mécanisme de conductivité électrique dans les boues; l'un dans lequel on sait que les réseaux de particules dominent et l'autre dans lequel le tunneling d'électrons est dominant, de sorte que la distribution et la taille des grappes de particules sont plus importantes.[78,84,88,102]

Le potentiel zêta des suspensions de carbone conducteur dans l'électrolyte organique ne peut pas non plus être généralisé à toujours positif ou toujours négatif; en outre, il apparaît que la taille du cation utilisé dans l'électrolyte est significative.[78,103] L'impact de la profondeur du canal sur la conductivité électrique de la suspension varie avec plusieurs paramètres simultanés tels que le débit, la concentration en matériau actif et le taux de C.[25,79] Dans la littérature, il n'y a pas d'approches de modélisation montrant une concurrence suffisamment fiable avec les expériences, ce qui indique que leurs capacités de prédiction sont faibles. En outre, les études expérimentales et les études de modélisation ont tendance à incorporer de plus en plus de phénomènes qui n'étaient traditionnellement pas étudiés dans le contexte des LIB.

Il est donc clair que les expériences et les modèles standard développés pour étudier les LIB ou les RFB ne constituent pas un moyen suffisant pour parvenir à la commercialisation, et les indicateurs de performance standard ne semblent pas offrir beaucoup d'éclairages. En raison du manque de compréhension quantitative concrète et généralisée, on peut conclure avec certitude que les SSRFB sont des systèmes complexes. La non-linéarité et la non-intuitivité sont les marques de la complexité et tout comportement émergent n'est que l'apparition de phénomènes imprévus qui tendent à confondre et à polariser la communauté scientifique.

Le chapitre 3 commence par une discussion sur les sources de complexité dans les SSRFB, qui découleraient de nombreux phénomènes concurrents à différentes échelles et en particulier du fait des interactions multi-corps et du comportement collectif des particules à moyenne échelle. Les outils de modélisation populaires, tels que MD, ne permettent pas la liberté théorique nécessaire à la découverte causale, ce qui est vital pour les

SSRFB. Comme exemple pour construire ce modèle, une étude expérimentale basée sur une suspension contenant du silicium et du carbone dans un électrolyte organique est tirée de la littérature.

Le modèle mécaniste, décrit dans ce chapitre, est particulièrement conçu pour fournir un cadre flexible. Il s'agit d'un modèle basé sur les agents développé en interne en Python qui simule le temps physiquement pertinent et met en œuvre le mouvement de particules via un moteur kMC. Il prend en compte des paramètres tels que le coefficient de diffusion, la viscosité, le rayon de la particule, la fraction volumique du solide, pour générer des vitesses cinétiques de mouvement. La décharge électrochimique de silicium par rapport à une anode de lithium métallique est modélisée en utilisant la cinétique de Butler-Volmer dans laquelle la densité de courant d'échange est modifiée pour prendre en compte la dilatation en volume du silicium. Un schéma de l'algorithme est fourni pour donner une image globale de la manière dont la simulation se déroule sur la grille tridimensionnelle.

Certains résultats de base ont été produits dans l'objectif de calibrer l'algorithme et d'ajuster les paramètres d'entrée pour produire des résultats physiquement pertinents, dans le contexte de la littérature expérimentale. La stochasticité dans les courbes de décharge a été observée en tant que caractéristique de sortie inhérente au modèle. Il a été traité en exécutant plusieurs simulations pour les mêmes conditions et en prenant en compte la moyenne. L'expansion en volume des particules de silicium est évidente grâce à la visualisation tridimensionnelle des résultats à l'aide du logiciel OVITO. Le chapitre suivant est conçu pour donner un aperçu de la méthode elle-même, afin de pouvoir obtenir une idée de conditions de simulation. Le chapitre suivant fournit des résultats physiquement pertinents pouvant fournir des explications qualitatives pour diverses études expérimentales apparemment contradictoires.

Le chapitre 4 explore le modèle mécaniste à travers PSA pour découvrir ses caractéristiques, forces et faiblesses en tant que méthode. Un PSA local est d'abord effectué en respectant les conditions expérimentales publiées dans la littérature. La sensibilité de la capacité de décharge est étudiée en termes de (i) taille de la boîte de simulation avec la profondeur, Z = 6, 8, 10, 12, 14, 16 unités, (ii) taux C, 2C, C, C / 5, C / 10 et C / 20, et (iii) une teneur en carbone de 3, 5, 7, 9, 11, 13, 15, 17 v%. On constate que la capacité diminue avec l'augmentation

des taux de C et de Z. L'augmentation de la teneur en carbone se traduit par une augmentation de la capacité suivie par une saturation, qui ressemble à peu près à la courbe sigmoïdale obtenue expérimentalement. Une distinction plus précise entre les régions de percolation et de saturation peut être obtenue en explorant l'évolution de la taille du réseau conducteur et du nombre de particules de silicium en contact avec le réseau conducteur.

Un PSA à plus grande échelle est réalisé sur 288 cas où la profondeur, le taux de C et la composition varient simultanément, avec Z = 6, 10, 14 unités, les taux de C C/5, C/10, C/20, une teneur en silicium de 6, 10, 14, 18 v%, teneur en carbone de 3, 5, 7, 9, 11, 13, 15, 17 v%. Chaque cas a été simulé 5 fois et une moyenne de reproductibilité a été établie. L'évolution de la barre d'erreur ainsi que l'efficacité du calcul du modèle ont été étudiés en fonction de la composition et de la taille de la boîte de simulation. Ceci fournit un outil utile pour quantifier le compromis entre précision et efficacité pour un algorithme donné. En outre, cette grande quantité de données fournit un moyen d'explorer la sensibilité de la transition entre la région de percolation et de saturation, appelée seuil de conductivité par commodité. La sensibilité de ce seuil dépend non seulement du paramètre, mais également de la valeur du paramètre. Par exemple, le seuil est plus sensible au contenu en silicium à 14 v% au lieu de 10 v%. Il a été observé que la profondeur était le paramètre le plus sensible, ce qui suggère que les effets de taille finie pourraient éclipser les détails mécanistiques pertinents sur le plan physique. Après avoir modifié un détail algorithmique réduisant le degré de discrétion du modèle et faisant varier le rayon de la particule de manière plus continue, les barres de résultats ont été considérablement réduites. En outre, une plus grande gamme de tailles de boîtes de simulation ont été simulées, Z = 6, 10, 14, 18, 22, 26 unités et il a été observé qu'au-dessus de Z = 18 unités, une convergence du comportement était observée.

L'origine complexe des effets de taille finie dans ce modèle discret dévoile les interactions de paramètres complexes qui ont lieu dans le modèle. La théorie des graphes a été introduite en tant qu'outil de perspective pour caractériser et quantifier l'interdépendance des paramètres et fournir un organigramme de causalité clair. Il a été observé que la complexité provient d'une classe spécifique de nœuds, ou paramètres, qui ont un grand nombre d'entrées. Il en résulte une compétition entre de nombreux effets, ce qui entraîne une sortie potentiellement non

intuitive du nœud donné, ce qui confirme les affirmations selon lesquelles la complexité découle du problème des phénomènes multiples. Ce type de comportement ne peut pas être décrit par de simples relations empiriques, montrant ainsi l'importance de créer des modèles avec des cadres théoriques flexibles avec des graphes de flux causaux.

Le chapitre 5 propose une étude de cas pour une hypothèse simple, à savoir comment la participation de particules de silicium à la formation d'un réseau conducteur peut avoir une incidence sur le comportement de décharge du SSRFB. À cette fin, un interrupteur pour la conductivité du silicium a été introduit dans l'algorithme. En plus d'avoir un impact sur les phénomènes de formation de réseau, il a été considéré que supposer que la conductivité électronique du silicium augmente lors de la lithiation aurait également une incidence sur le taux de lithiation lui-même. La section 5.1.1 montre comment ajouter systématiquement une nouvelle fonctionnalité au modèle en étudiant sa réponse pour quatre compositions de suspension différentes (teneur en silicium de 6 v%, 14% combinée à une teneur en carbone de 5% et 13%). Bien que l'impact d'un taux de lithiation en évolution reste à étudier, il a été observé que l'impact de la participation du silicium dans les réseaux conducteurs était plus évident lorsque le contenu en carbone était insuffisant pour former des réseaux par lui-même. Bien que ce résultat soit intuitif, l'évolution des réseaux conducteurs et la distribution granulométrique montrent quatre comportements morphologiques distincts dans le slurry. Ceux-ci peuvent être utilisés comme outils pour caractériser et expliquer d'autres résultats, ainsi que pour fournir une image qualitative de certains résultats expérimentaux dans la littérature. La section 5.1.2 explore plus en détail l'impact du commutateur de conductivité dans le contexte des perturbations de la taille de la boîte de simulation et du taux de carbone pour différentes compositions. Les paramètres modifiés ici sont la teneur en carbone (5%, 13%), la teneur en silicium (6%, 14%), le taux C (1C, C/20), la profondeur de la boîte de simulation (20, 25, 30, 40, 45 unités). Il a été constaté que quel que soit le taux de C, l'augmentation de la profondeur entraînait une diminution de la capacité de décharge. Cependant, le rôle du contenu en silicium, quel que soit le commutateur de conductivité, était moins intuitif, car les résultats suggéraient qu'il pouvait jouer un rôle à la fois constructif et perturbateur pour les réseaux conducteurs. Les études de

sensibilité multiparamètres à partir d'expériences ont été discutées dans ce contexte et il a été démontré comment la complexité et la non-intuitivité dans les expériences découlent de la compétition entre plusieurs phénomènes.

La section 5.1.3 présente une vaste étude sur l'impact du commutateur de conductivité sur la composition du lisier. Les 121 compositions constituées de combinaisons entre la teneur en silicium (3, 4, 5, 6, 7, 8, 9, 10, 11, 14, 15 v%) et la teneur en carbone (0, 2, 4, 6, 8, 10, 12, 14, 16, 18, 20 v%). La nature de la tendance de la capacité par rapport au contenu en carbone est sigmoïdale lorsque le commutateur de conductivité est désactivé et de second ordre exponentielle lorsque le commutateur de conductivité est activé. Cette étude fournit un moyen d'accéder à plusieurs états du système et constitue essentiellement une étude de sensibilité globale aux paramètres. Cela offre en outre la possibilité de créer une image globale, à l'image d'une surface d'énergie potentielle, afin d'explorer comment la capacité est influencée par le contenu solide d'un lisier, quelle que soit l'étendue de la participation à la formation d'un réseau. Les résultats de cette analyse montrent qu'il est possible de créer un paysage prenant en compte de multiples aspects, tels que la composition et les conditions de fonctionnement, pour créer un ensemble complet d'outils permettant de choisir un système optimal. Cela a été rendu possible par l'introduction de plusieurs nouvelles quantités mésoscopiques qui permettent de regrouper des paramètres d'échelle inférieure en métriques utilisables, par exemple, le total des solides conducteurs, le réseau conducteur réel, l'espace conducteur réel et les solides conducteurs réels. Ces paramètres permettent de classer la phase de suspension en grappes sur la base des rapports entre solide, liquide et électroniquement actif et actif, simultanément. Bien qu'il puisse être difficile d'obtenir une validation directe pour de tels métriques, reconnaître leur utilité peut aider à extraire davantage d'informations des techniques expérimentales à venir et nouvelles utilisées pour étudier simultanément plusieurs phénomènes.

Comme le montre la figure R.1, un nouveau paradigme est proposé à la suite de ce travail de thèse. Il concerne la spécification de modèle en établissant un réseau causal de base d'un système d'échantillon avec des phénomènes choisis dans une carte maîtresse phénoménologique (Figure R.1 (a) - (b)), (ii) mener des expériences hypothétiques utilisant un ABM avec un moteur kMC pour étudier le comportement dans des conditions de

complexité réduite (Figure R.1 (c) - (e)), et (iii) explorer l'évolution des métriques standard et spéciales en fonction des variations de valeurs de paramètres simultanées (Figure R.1 (f)). À travers ces étapes, il est démontré comment la découverte causale, généralement basée sur l'intuition, peut être rendue plus rigoureuse. En outre, comme indiqué au chapitre 5, le paradigme devra analyser des ensembles de données multidimensionnels pour traiter la complexité.

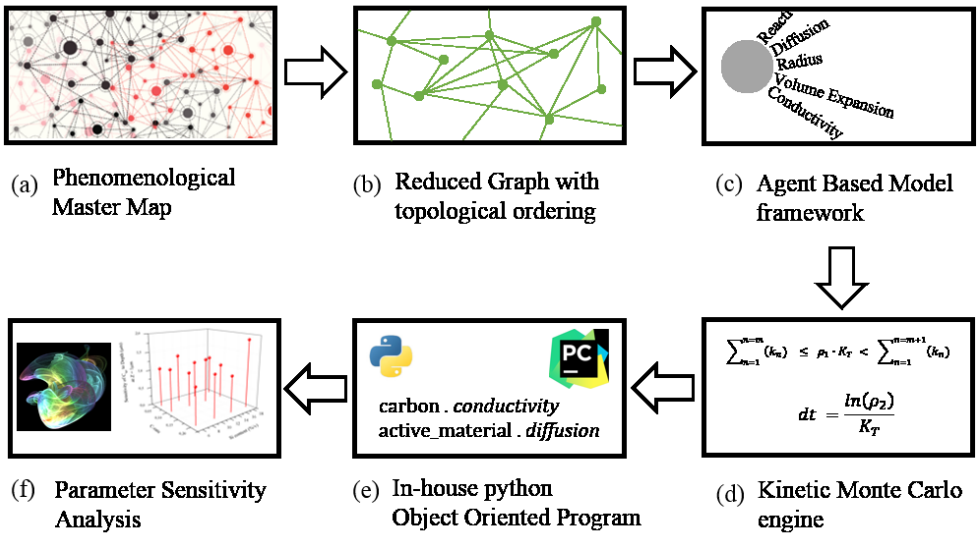

Figure R.1. Schéma décrivant le flux de travail proposé pour le SSRFB.

Créer un modèle mécaniste pour exécuter une expérience hypothétique peut être appelé «hypothèse», mais il ne s'agit pas d'une approche nouvelle. Par exemple, entre 1905 et 1908, la théorie du mouvement brownien a été traitée de manière théorique par Einstein, Smoluchowski et Langevin étant donné que les expérimentateurs ne savaient pas quoi mesurer.[64] Cependant, la différence est qu'au lieu d'imaginer le comportement d'un seul phénomène ou d'un ensemble de phénomènes en termes absolus, l'objectif est d'explorer ce qui se passe lorsqu'il y a de multiples phénomènes mal compris en concurrence les uns avec les autres.

En conclusion, cette thèse vise à fournir un outil d'aide à l'approche expérimentale basée sur les essais et erreurs, généralement utilisée pour développer des systèmes électrochimiques destinés aux applications énergétiques. En tant que dispositif, la batterie à flux redox semi-solide (SSRFB) offre un grand potentiel pour

explorer la manifestation de la coexistence de multiples phénomènes de disciplines différentes telles que la rhéologie, l'électrochimie, la dynamique des particules et la dynamique des fluides. L'état de la technique démontre que les SSRFB ont tendance à montrer des résultats contradictoires et non intuitifs, ce qui rend difficile l'obtention des progrès rapides nécessaires à la commercialisation.

Puisque la littérature rapporte les avantages de décharger le SSRFB dans des conditions d'écoulement intermittent, ce travail se concentre sur l'étude d'une suspension à base de silicium et de carbone en mode statique. Bien que seules la coexistence de la dynamique des particules et de l'électrochimie à l'échelle moyenne soient explorées dans ce travail, il s'agit d'une étude très riche qui montre en quoi le SSRFB est un bon exemple de système complexe. En utilisant un modèle mécaniste et une analyse de sensibilité des paramètres (PSA), et avec la théorie des graphes comme outil de perspective, une nouvelle méthodologie est établie. Il est utilisé pour simuler des particules sur une grille tridimensionnelle discrète, de sorte qu'elles subissent un mouvement pseudo-brownien ainsi qu'une décharge électrochimique par la formation de réseaux conducteurs. Le modèle mécanistique est basé sur la méthode cinétique Monte Carlo utilisant la méthode de la taille de pas variable et a été développé en interne à l'aide de la programmation orientée objet en Python. La physique sous-jacente au modèle repose sur une sélection des phénomènes les plus pertinents à l'échelle moyenne, tels que la diffusion de particules calculée à partir de la viscosité et de la taille des particules, et l'électrochimie calculée à l'aide de la cinétique de Butler Volmer qui prend en compte la dilatation en volume des particules de silicium à la décharge. Ce modèle mécaniste peut également être considéré comme un modèle à base d'agents dans lequel les particules agissent comme des agents libres pouvant se déplacer à travers la grille tridimensionnelle et interagir les unes avec les autres.

Comme ces modèles sont très difficiles à normaliser et à valider, PSA a déployé des efforts considérables pour explorer ses caractéristiques, ses limites et ses atouts. La mise en œuvre d'une technique de modélisation stochastique telle que kMC et la simulation de la suspension sur une grille discrète ont entraîné des fluctuations dans les données qui variaient en fonction des conditions d'entrée. Il a été démontré que les systèmes complexes peuvent être mieux étudiés en observant la réponse du système à des perturbations dans de nombreux paramètres

d'entrée différents. L'obtention de sensibilités physiquement pertinentes grâce à cette méthode a permis de minimiser les artefacts provenant de la nature du modèle. De plus, il a été montré comment, dans un système complexe, la sensibilité d'un paramètre p à des perturbations dans n1 peut être influencée non seulement par la valeur de n1 considérée, mais également par celle d'autres paramètres n2, n3, n4, etc. Par conséquent, la compréhension de la dynamique sous-jacente entre les paramètres et les phénomènes a été jugée aussi importante que la quantification précise de la valeur d'un paramètre unique. Cela explique pourquoi les études expérimentales sur des systèmes complexes donnent des résultats non intuitifs et que les approches réductionnistes visant à étudier le comportement d'un tel système sont très difficiles.

Pour démontrer l'utilité de ce modèle, une hypothèse simple a été testée, à savoir la comparaison entre un cas où des réseaux conducteurs sont formés avec du carbone seul et un cas où le silicium et le carbone participent à la fois. Des caractéristiques claires sont ressorties des deux cas, corroborées par la littérature expérimentale rapportant un comportement de la conductivité par rapport à la teneur en carbone. Typiquement, un seuil de percolation est suivi d'une région de percolation linéaire et d'une saturation en conductivité. Avec l'introduction d'un nouveau paramètre, le total des solides conducteurs, qui ne différencie pas le silicium du carbone, il a été possible de générer un paysage global du comportement de décharge en fonction du contenu solide. Par conséquent, il est possible de définir davantage de paramètres permettant de caractériser une suspension de particules sur la base de facteurs tels que le ratio solide / liquide et le ratio solide inactif actif, où l'inactivité solide peut être différenciée soit en raison d'un manque de connectivité électrique, soit en raison de son incapacité à fonctionner conduire des électrons. Les tendances de ces mesures montrent une valeur optimale, fournissant ainsi d'autres aspects pouvant aider à identifier les conditions appropriées pour obtenir de bonnes capacités de décharge.

Examiner le domaine du stockage d'énergie électrochimique à travers l'objectif de la théorie de la complexité a également permis la création d'une carte mentale compilant divers phénomènes se produisant au sein d'une batterie lithium-ion. Cela devrait aider à formuler des hypothèses lorsque confronté à des observations expérimentales contradictoires.

References

(1) Weltwirtschaftsforum; Zurich Insurance Group. *Global Risks 2019: Insight Report*; 2019.

(2) Aichele, R.; Felbermayr, G. Kyoto and the Carbon Footprint of Nations. *J. Environ. Econ. Manag.* **2012**, *63* (3), 336–354. https://doi.org/10.1016/j.jeem.2011.10.005.

(3) *Political Mistakes and Policy Failures in International Relations*; Kruck, A., Oppermann, K., Spencer, A., Eds.; Springer International Publishing: Cham, 2018. https://doi.org/10.1007/978-3-319-68173-3.

(4) Davis, S. J.; Cao, L.; Caldeira, K.; Hoffert, M. I. Rethinking Wedges. *Environ. Res. Lett.* **2013**, *8* (1), 011001. https://doi.org/10.1088/1748-9326/8/1/011001.

(5) Cole, D. H. Advantages of a Polycentric Approach to Climate Change Policy. *Nat. Clim. Change* **2015**, *5* (2), 114–118. https://doi.org/10.1038/nclimate2490.

(6) Valverde, S.; Solé, R. V.; Bedau, M. A.; Packard, N. Topology and Evolution of Technology Innovation Networks. *Phys. Rev. E* **2007**, *76* (5), 056118. https://doi.org/10.1103/PhysRevE.76.056118.

(7) Quintana-García, C.; Benavides-Velasco, C. A. Innovative Competence, Exploration and Exploitation: The Influence of Technological Diversification. *Res. Policy* **2008**, *37* (3), 492–507. https://doi.org/10.1016/j.respol.2007.12.002.

(8) Garcia-Vega, M. Does Technological Diversification Promote Innovation? *Res. Policy* **2006**, *35* (2), 230–246. https://doi.org/10.1016/j.respol.2005.09.006.

(9) Deligianni, I.; Voudouris, I.; Lioukas, S. The Relationship Between Innovation and Diversification in the Case of New Ventures: Unidirectional or Bidirectional? *IEEE Trans. Eng. Manag.* **2014**, *61* (3), 462–475. https://doi.org/10.1109/TEM.2014.2312732.

(10) The Concept of Economic Diversification in the Context of Response Measures. *UNFCC* **2016**.

(11) Chatterjee, P. Interfirm Alliances in Online Retailing. *J. Bus. Res.* **2004**, *57* (7), 714–723. https://doi.org/10.1016/S0148-2963(02)00362-4.

(12) Yun, S.; Lee, J.; Lee, S. Technology Development Strategies and Policy Support for the Solar Energy Industry under Technological Turbulence. *Energy Policy* **2019**, *124*, 206–214. https://doi.org/10.1016/j.enpol.2018.09.003.

(13) Tijssen, R. J. W. Global and Domestic Utilization of Industrial Relevant Science: Patent Citation Analysis of Science–Technology Interactions and Knowledge Flows. *Res. Policy* **2001**, *30* (1), 35–54. https://doi.org/10.1016/S0048-7333(99)00080-3.

(14) Lungeanu, A.; Contractor, N. S. The Effects of Diversity and Network Ties on Innovations: The Emergence of a New Scientific Field. *Am. Behav. Sci.* **2015**, *59* (5), 548–564. https://doi.org/10.1177/0002764214556804.

(15) Winter, M.; Barnett, B.; Xu, K. Before Li Ion Batteries. *Chem. Rev.* **2018**, *118* (23), 11433–11456. https://doi.org/10.1021/acs.chemrev.8b00422.

(16) Jain, A.; Ong, S. P.; Hautier, G.; Chen, W.; Richards, W. D.; Dacek, S.; Cholia, S.; Gunter, D.; Skinner, D.; Ceder, G.; et al. Commentary: The Materials Project: A Materials Genome Approach to Accelerating Materials Innovation. *APL Mater.* **2013**, *1* (1), 011002. https://doi.org/10.1063/1.4812323.

(17) Wang, W.; Luo, Q.; Li, B.; Wei, X.; Li, L.; Yang, Z. Recent Progress in Redox Flow Battery Research and Development. *Adv. Funct. Mater.* **2013**, *23* (8), 970–986.

(18) Electric Energy Storage Technology Options: A White Paper Primer on Applications, Costs, and Benefits. 170.

(19) Noack, J.; Roznyatovskaya, N.; Herr, T.; Fischer, P. The Chemistry of Redox-Flow Batteries. *Angew. Chem. Int. Ed.* **2015**, *54* (34), 9776–9809. https://doi.org/10.1002/anie.201410823.

(20) Duduta, M.; Ho, B.; Wood, V. C.; Limthongkul, P.; Brunini, V. E.; Carter, W. C.; Chiang, Y.-M. Semi-Solid Lithium Rechargeable Flow Battery. *Adv. Energy Mater.* **2011**, *1* (4), 511–516. https://doi.org/10.1002/aenm.201100152.

(21) Gandomi, Y. A.; Aaron, D. S.; Houser, J. R.; Daugherty, M. C.; Clement, J. T.; Pezeshki, A. M.; Ertugrul, T. Y.; Moseley, D. P.; Mench, M. M. Critical Review—Experimental Diagnostics and Material Characterization Techniques Used on Redox Flow Batteries. *J. Electrochem. Soc.* **2018**, *165* (5), A970–A1010. https://doi.org/10.1149/2.0601805jes.

(22) Qi, Z.; Koenig, G. M. Review Article: Flow Battery Systems with Solid Electroactive Materials. *J. Vac. Sci. Technol. B Nanotechnol. Microelectron. Mater. Process. Meas. Phenom.* **2017**, *35* (4), 040801. https://doi.org/10.1116/1.4983210.

(23) Soloveichik, G. L. Flow Batteries: Current Status and Trends. *Chem. Rev.* **2015**, 150921152840008. https://doi.org/10.1021/cr500720t.

(24) Hatzell, K. B.; Boota, M.; Gogotsi, Y. Materials for Suspension (Semi-Solid) Electrodes for Energy and Water Technologies. *Chem Soc Rev* **2015**, *44* (23), 8664–8687. https://doi.org/10.1039/C5CS00279F.

(25) Dennison, C. R.; Beidaghi, M.; Hatzell, K. B.; Campos, J. W.; Gogotsi, Y.; Kumbur, E. C. Effects of Flow Cell Design on Charge Percolation and Storage in the Carbon Slurry Electrodes of Electrochemical Flow Capacitors. *J. Power Sources* **2014**, *247*, 489–496. https://doi.org/10.1016/j.jpowsour.2013.08.101.

(26) Presser, V.; Dennison, C. R.; Campos, J.; Knehr, K. W.; Kumbur, E. C.; Gogotsi, Y. The Electrochemical Flow Capacitor: A New Concept for Rapid Energy Storage and Recovery. *Adv. Energy Mater.* **2012**, *2* (7), 895–902. https://doi.org/10.1002/aenm.201100768.

(27) Campos, J. W.; Beidaghi, M.; Hatzell, K. B.; Dennison, C. R.; Musci, B.; Presser, V.; Kumbur, E. C.; Gogotsi, Y. Investigation of Carbon Materials for Use as a Flowable Electrode in Electrochemical Flow Capacitors. *Electrochimica Acta* **2013**, *98*, 123–130. https://doi.org/10.1016/j.electacta.2013.03.037.

(28) Hatzell, K. B.; Fan, L.; Beidaghi, M.; Boota, M.; Pomerantseva, E.; Kumbur, E. C.; Gogotsi, Y. Composite Manganese Oxide Percolating Networks As a Suspension Electrode for an Asymmetric Flow Capacitor. *ACS Appl. Mater. Interfaces* **2014**, *6* (11), 8886–8893. https://doi.org/10.1021/am501650q.

(29) Boota, M.; Hatzell, K. B.; Alhabeb, M.; Kumbur, E. C.; Gogotsi, Y. Graphene-Containing Flowable Electrodes for Capacitive Energy Storage. *Carbon* **2015**, *92*, 142–149. https://doi.org/10.1016/j.carbon.2015.04.020.

(30) Hatzell, K. B.; Boota, M.; Kumbur, E. C.; Gogotsi, Y. Flowable Conducting Particle Networks in Redox-Active Electrolytes for Grid Energy Storage. *J. Electrochem. Soc.* **2015**, *162* (5), A5007–A5012.

(31) Akuzum, B.; Hudson, D. D.; Eichfeld, D. A.; Dennison, C. R.; Agartan, L.; Gogotsi, Y.; Kumbur, E. C. Reticulated Carbon Electrodes for Improved Charge Transport in Electrochemical Flow Capacitors. *J. Electrochem. Soc.* **2018**, *165* (11), A2519–A2527. https://doi.org/10.1149/2.0361811jes.

(32) Tian, M.; Sun, Y.; Zhang, C. (John); Wang, J.; Qiao, W.; Ling, L.; Long, D. Enabling High-Rate Electrochemical Flow Capacitors Based on Mesoporous Carbon Microspheres Suspension Electrodes. *J. Power Sources* **2017**, *364*, 182–190. https://doi.org/10.1016/j.jpowsour.2017.08.001.

(33) Tian, C.; Lin, F.; Doeff, M. M. Electrochemical Characteristics of Layered Transition Metal Oxide Cathode Materials for Lithium Ion Batteries: Surface, Bulk Behavior, and Thermal Properties. *Acc. Chem. Res.* **2018**, *51* (1), 89–96. https://doi.org/10.1021/acs.accounts.7b00520.

(34) Rommerskirchen, A.; Kalde, A.; Linnartz, C. J.; Bongers, L.; Linz, G.; Wessling, M. Unraveling Charge Transport in Carbon Flow-Electrodes: Performance Prediction for Desalination Applications. *Carbon* **2019**, *145*, 507–520. https://doi.org/10.1016/j.carbon.2019.01.053.

(35) Jeon, S.; Park, H.; Yeo, J.; Yang, S.; Cho, C. H.; Han, M. H.; Kim, D. K. Desalination via a New Membrane Capacitive Deionization Process Utilizing Flow-Electrodes. *Energy Environ. Sci.* **2013**, *6* (5), 1471. https://doi.org/10.1039/c3ee24443a.

(36) Suss, M. E.; Porada, S.; Sun, X.; Biesheuvel, P. M.; Yoon, J.; Presser, V. Water Desalination via Capacitive Deionization: What Is It and What Can We Expect from It? *Energy Environ. Sci.* **2015**, *8* (8), 2296–2319. https://doi.org/10.1039/C5EE00519A.

(37) Fan, L.; Jia, C.; Zhu, Y. G.; Wang, Q. Redox Targeting of Prussian Blue: Toward Low-Cost and High Energy Density Redox Flow Battery and Solar Rechargeable Battery. *ACS Energy Lett.* **2017**, *2* (3), 615–621. https://doi.org/10.1021/acsenergylett.6b00667.

(38) Huang, Q.; Li, H.; Grätzel, M.; Wang, Q. Reversible Chemical Delithiation/Lithiation of $LiFePO_4$: Towards a Redox Flow Lithium-Ion Battery. *Phys Chem Chem Phys* **2013**, *15* (6), 1793–1797. https://doi.org/10.1039/C2CP44466F.

(39) Pan, F.; Yang, J.; Huang, Q.; Wang, X.; Huang, H.; Wang, Q. Redox Targeting of Anatase TiO_2 for Redox Flow Lithium-Ion Batteries. *Adv. Energy Mater.* **2014**, *4* (15), 1400567. https://doi.org/10.1002/aenm.201400567.

(40) Jia, C.; Pan, F.; Zhu, Y. G.; Huang, Q.; Lu, L.; Wang, Q. High-Energy Density Nonaqueous All Redox Flow Lithium Battery Enabled with a Polymeric Membrane. *Sci. Adv.* **2015**, *1* (10), e1500886–e1500886. https://doi.org/10.1126/sciadv.1500886.

(41) Pan, F.; Huang, Q.; Huang, H.; Wang, Q. High-Energy Density Redox Flow Lithium Battery with Unprecedented Voltage Efficiency. *Chem. Mater.* **2016**, *28* (7), 2052–2057. https://doi.org/10.1021/acs.chemmater.5b04558.

(42) Zanzola, E.; Dennison, C. R.; Battistel, A.; Peljo, P.; Vrubel, H.; Amstutz, V.; Girault, H. H. Redox Solid Energy Boosters for Flow Batteries: Polyaniline as a Case Study. *Electrochimica Acta* **2017**, *235*, 664–671. https://doi.org/10.1016/j.electacta.2017.03.084.

(43) Zhu, Y. G.; Du, Y.; Jia, C.; Zhou, M.; Fan, L.; Wang, X.; Wang, Q. Unleashing the Power and Energy of $LiFePO_4$-Based Redox Flow Lithium Battery with a Bifunctional Redox Mediator. *J. Am. Chem. Soc.* **2017**, *139* (18), 6286–6289. https://doi.org/10.1021/jacs.7b01146.

(44) Yan, R.; Ghilane, J.; Phuah, K. C.; Pham Truong, T. N.; Adams, S.; Randriamahazaka, H.; Wang, Q. Determining Li^+-Coupled Redox Targeting Reaction Kinetics of Battery Materials with Scanning Electrochemical Microscopy. *J. Phys. Chem. Lett.* **2018**, *9* (3), 491–496. https://doi.org/10.1021/acs.jpclett.7b03136.

(45) Zhou, M.; Huang, Q.; Pham Truong, T. N.; Ghilane, J.; Zhu, Y. G.; Jia, C.; Yan, R.; Fan, L.; Randriamahazaka, H.; Wang, Q. Nernstian-Potential-Driven Redox-Targeting Reactions of Battery Materials. *Chem* **2017**, *3* (6), 1036–1049. https://doi.org/10.1016/j.chempr.2017.10.003.

(46) Qi, Z.; Liu, A. L.; Koenig, G. M. Carbon-Free Solid Dispersion LiCoO2 Redox Couple Characterization and Electrochemical Evaluation for All Solid Dispersion Redox Flow Batteries. *Electrochimica Acta* **2017**, *228*, 91–99. https://doi.org/10.1016/j.electacta.2017.01.061.

(47) Qi, Z.; Dong, H.; Koenig, G. M. Electrochemical Characterization of Lithium-Ion Battery Cathode Materials with Aqueous Flowing Dispersions. *Electrochimica Acta* **2017**, *253*, 163–170. https://doi.org/10.1016/j.electacta.2017.09.031.

(48) Li, W.; Liang, Z.; Lu, Z.; Tao, X.; Liu, K.; Yao, H.; Cui, Y. Magnetic Field-Controlled Lithium Polysulfide Semiliquid Battery with Ferrofluidic Properties. *Nano Lett.* **2015**, *15* (11), 7394–7399. https://doi.org/10.1021/acs.nanolett.5b02818.

(49) Chen, H.; Zou, Q.; Liang, Z.; Liu, H.; Li, Q.; Lu, Y.-C. Sulphur-Impregnated Flow Cathode to Enable High-Energy-Density Lithium Flow Batteries. *Nat. Commun.* **2015**, *6*, 5877.

(50) Yang, F.; Mousavie, S. M. A.; Oh, T. K.; Yang, T.; Lu, Y.; Farley, C.; Bodnar, R. J.; Niu, L.; Qiao, R.; Li, Z. Sodium-Sulfur Flow Battery for Low-Cost Electrical Storage. *Adv. Energy Mater.* **2018**, *8* (11), 1701991. https://doi.org/10.1002/aenm.201701991.

(51) Fan, F. Y.; Woodford, W. H.; Li, Z.; Baram, N.; Smith, K. C.; Helal, A.; McKinley, G. H.; Carter, W. C.; Chiang, Y.-M. Polysulfide Flow Batteries Enabled by Percolating Nanoscale Conductor Networks. *Nano Lett.* **2014**, *14* (4), 2210–2218. https://doi.org/10.1021/nl500740t.

(52) Xu, S.; Zhang, L.; Zhang, X.; Cai, Y.; Zhang, S. A Self-Stabilized Suspension Catholyte to Enable Long-Term Stable Li–S Flow Batteries. *J. Mater. Chem. A* **2017**, *5* (25), 12904–12913. https://doi.org/10.1039/C7TA02110K.

(53) Chen, X.; Hopkins, B. J.; Helal, A.; Fan, F. Y.; Smith, K. C.; Li, Z.; Slocum, A. H.; McKinley, G. H.; Carter, W. C.; Chiang, Y.-M. A Low-Dissipation, Pumpless, Gravity-Induced Flow Battery. *Energy Environ. Sci.* **2016**, *9* (5), 1760–1770. https://doi.org/10.1039/C6EE00874G.

(54) Li, J.; Yang, L.; Yang, S.; Lee, J. Y. The Application of Redox Targeting Principles to the Design of Rechargeable Li-S Flow Batteries. *Adv. Energy Mater.* **2015**, *5* (24), 1501808. https://doi.org/10.1002/aenm.201501808.

(55) Li, C.; Ward, A. L.; Doris, S. E.; Pascal, T. A.; Prendergast, D.; Helms, B. A. Polysulfide-Blocking Microporous Polymer Membrane Tailored for Hybrid Li-Sulfur Flow Batteries. *Nano Lett.* **2015**, *15* (9), 5724–5729. https://doi.org/10.1021/acs.nanolett.5b02078.

(56) Mubeen, S.; Jun, Y.; Lee, J.; McFarland, E. W. Solid Suspension Flow Batteries Using Earth Abundant Materials. *ACS Appl. Mater. Interfaces* **2016**, *8* (3), 1759–1765. https://doi.org/10.1021/acsami.5b09515.

(57) Li, Y.; He, C.; Timofeeva, E. V.; Ding, Y.; Parrondo, J.; Segre, C.; Ramani, V. β-Nickel Hydroxide Cathode Material for Nano-Suspension Redox Flow Batteries. *Front. Energy* **2017**. https://doi.org/10.1007/s11708-017-0496-0.

(58) Sen, S.; Chow, C.-M.; Moazzen, E.; Segre, C. U.; Timofeeva, E. V. Electroactive Nanofluids with High Solid Loading and Low Viscosity for Rechargeable Redox Flow Batteries. *J. Appl. Electrochem.* **2017**, *47* (5), 593–605. https://doi.org/10.1007/s10800-017-1063-4.

(59) Ruggeri, I.; Arbizzani, C.; Soavi, F. A Novel Concept of Semi-Solid, Li Redox Flow Air (O2) Battery: A Breakthrough towards High Energy and Power Batteries. *Electrochimica Acta* **2016**, *206*, 291–300. https://doi.org/10.1016/j.electacta.2016.04.139.

(60) Ruggeri, I.; Arbizzani, C.; Soavi, F. Carbonaceous Catholyte for High Energy Density Semi-Solid Li/O2 Flow Battery. *Carbon* **2018**, *130*, 749–757. https://doi.org/10.1016/j.carbon.2018.01.056.

(61) C. Kupsch; D. Weik; L. Feierabend; R. Nauber; L. Büttner; J. Czarske. Vector Flow Imaging of a Highly-Laden Suspension in a Zinc-Air Flow Battery Model. *IEEE Trans. Ultrason. Ferroelectr. Freq. Control* **2019**, 1–1. https://doi.org/10.1109/TUFFC.2019.2891514.

(62) Wendt, H.; Kreysa, G. *Electrochemical Engineering: Science and Technology in Chemical and Other Industries*, Softcover version of original hardcover ed. 1999.; Springer: Berlin, 2010.

(63) Scrosati, B. History of Lithium Batteries. *J. Solid State Electrochem.* **2011**, *15* (7–8), 1623–1630. https://doi.org/10.1007/s10008-011-1386-8.

(64) Furukawa, N. Development and Commercialization of Nickel-Metal Hydride Secondary Batteries. *J. Power Sources* **1994**, *51* (1–2), 45–59. https://doi.org/10.1016/0378-7753(94)01928-2.

(65) Laszczynski, S. v; Gorski, S. v. Leitfähigkeit von Lösungen Eniger Saltze in Pyridin. *Z Elektrochem* **1897**, *4*, 290–293.

(66) Harris, W. S. Electrochemical Studies in Cyclic Esters. **1958**.

(67) Weintraub, E. Suspension of Carbon in Alkali Metals and Process of Making Same. **1909**.

(68) Fong, R.; Von Sacken, U.; Dahn, J. R. Studies of Lithium Intercalation into Carbons Using Nonaqueous Electrochemical Cells. *J. Electrochem. Soc.* **1990**, *137* (7), 2009–2013.

(69) Chiang, Y.-M.; Carter, W. C.; Ho, B. H.; Duduta, M. *High Energy Density Redox Flow Device*; Google Patents, 2009.

(70) Li, Z.; Smith, K. C.; Dong, Y.; Baram, N.; Fan, F. Y.; Xie, J.; Limthongkul, P.; Carter, W. C.; Chiang, Y.-M. Aqueous Semi-Solid Flow Cell: Demonstration and Analysis. *Phys. Chem. Chem. Phys.* **2013**, *15* (38), 15833. https://doi.org/10.1039/c3cp53428f.

(71) Hamelet, S.; Tzedakis, T.; Leriche, J.-B.; Sailler, S.; Larcher, D.; Taberna, P.-L.; Simon, P.; Tarascon, J.-M. Non-Aqueous Li-Based Redox Flow Batteries. *J. Electrochem. Soc.* **2012**, *159* (8), A1360–A1367.

(72) Hamelet, S.; Larcher, D.; Dupont, L.; Tarascon, J.-M. Silicon-Based Non Aqueous Anolyte for Li Redox-Flow Batteries. *J. Electrochem. Soc.* **2013**, *160* (3), A516–A520.

(73) Chen, H.; Lai, N.-C.; Lu, Y.-C. Silicon–Carbon Nanocomposite Semi-Solid Negolyte and Its Application in Redox Flow Batteries. *Chem. Mater.* **2017**, *29* (17), 7533–7542. https://doi.org/10.1021/acs.chemmater.7b02561.

(74) Ventosa, E.; Buchholz, D.; Klink, S.; Flox, C.; Chagas, L. G.; Vaalma, C.; Schuhmann, W.; Passerini, S.; Morante, J. R. Non-Aqueous Semi-Solid Flow Battery Based on Na-Ion Chemistry. P2-Type $Na_x Ni_{0.22} Co_{0.11} Mn_{0.66} O_2$ –$NaTi_2(PO_4)_3$. *Chem. Commun.* **2015**, *51* (34), 7298–7301. https://doi.org/10.1039/C4CC09597A.

(75) Lacroix, R.; Biendicho, J. J.; Mulder, G.; Sanz, L.; Flox, C.; Morante, J. R.; Da Silva, S. Modelling the Rheology and Electrochemical Performance of Li4Ti5O12 and LiNi1/3Co1/3Mn1/3O2 Based Suspensions for Semi-Solid Flow Batteries. *Electrochimica Acta* **2019**, *304*, 146–157. https://doi.org/10.1016/j.electacta.2019.02.107.

(76) Halfon, E. B.; Suss, M. E. Measurements of the Electric Conductivity of an Electrode as It Transitions between Static and Flowable Modes. *Electrochem. Commun.* **2019**. https://doi.org/10.1016/j.elecom.2018.12.016.

(77) Ventosa, E.; Zampardi, G.; Flox, C.; La Mantia, F.; Schuhmann, W.; Morante, J. R. Solid Electrolyte Interphase in Semi-Solid Flow Batteries: A Wolf in Sheep's Clothing. *Chem Commun* **2015**, *51* (81), 14973–14976. https://doi.org/10.1039/C5CC04767F.

(78) Youssry, M.; Madec, L.; Soudan, P.; Cerbelaud, M.; Guyomard, D.; Lestriez, B. Non-Aqueous Carbon Black Suspensions for Lithium-Based Redox Flow Batteries: Rheology and Simultaneous Rheo-Electrical Behavior. *Phys. Chem. Chem. Phys.* **2013**, *15* (34), 14476. https://doi.org/10.1039/c3cp51371h.

(79) Madec, L.; Youssry, M.; Cerbelaud, M.; Soudan, P.; Guyomard, D.; Lestriez, B. Electronic vs Ionic Limitations to Electrochemical Performance in Li4Ti5O12-Based Organic Suspensions for Lithium-Redox Flow Batteries. *J. Electrochem. Soc.* **2014**, *161* (5), A693–A699.

(80) Youssry, M.; Kamand, F. Z.; Magzoub, M. I.; Nasser, M. S. Aqueous Dispersions of Carbon Black and Its Hybrid with Carbon Nanofibers. *RSC Adv.* **2018**, *8* (56), 32119–32131. https://doi.org/10.1039/C8RA05446K.

(81) Madec, L.; Youssry, M.; Cerbelaud, M.; Soudan, P.; Guyomard, D.; Lestriez, B. Surfactant for Enhanced Rheological, Electrical, and Electrochemical Performance of Suspensions for Semisolid Redox Flow Batteries and Supercapacitors. *ChemPlusChem* **2015**, *80* (2), 396–401. https://doi.org/10.1002/cplu.201402042.

(82) Youssry, M.; Guyomard, D.; Lestriez, B. Suspensions of Carbon Nanofibers in Organic Medium: Rheo-Electrical Properties. *Phys Chem Chem Phys* **2015**, *17* (48), 32316–32327. https://doi.org/10.1039/C5CP06303E.

(83) Wei, T.-S.; Fan, F. Y.; Helal, A.; Smith, K. C.; McKinley, G. H.; Chiang, Y.-M.; Lewis, J. A. Biphasic Electrode Suspensions for Li-Ion Semi-Solid Flow Cells with High Energy Density, Fast Charge Transport, and Low-Dissipation Flow. *Adv. Energy Mater.* **2015**, *5* (15), 1500535. https://doi.org/10.1002/aenm.201500535.

(84) Parant, H.; Muller, G.; Le Mercier, T.; Tarascon, J. M.; Poulin, P.; Colin, A. Flowing Suspensions of Carbon Black with High Electronic Conductivity for Flow Applications: Comparison between Carbons Black and Exhibition of Specific Aggregation of Carbon Particles. *Carbon* **2017**, *119*, 10–20. https://doi.org/10.1016/j.carbon.2017.04.014.

(85) Narayanan, A.; Wijnperlé, D.; Mugele, F.; Buchholz, D.; Vaalma, C.; Dou, X.; Passerini, S.; Duits, M. H. G. Influence of Electrochemical Cycling on the Rheo-Impedance of Anolytes for Li-Based Semi Solid Flow Batteries. *Electrochimica Acta* **2017**, *251*, 388–395. https://doi.org/10.1016/j.electacta.2017.08.022.

(86) Narayanan, A.; Mugele, F.; Duits, M. H. G. Mechanical History Dependence in Carbon Black Suspensions for Flow Batteries: A Rheo-Impedance Study. *Langmuir* **2017**, *33* (7), 1629–1638. https://doi.org/10.1021/acs.langmuir.6b04322.

(87) Narayanan, A.; Mugele, F.; Duits, M. H. G. Device for Rheometry, Impedance Spectroscopy, and Electrochemistry on Fluid Electrodes. *Rev. Sci. Instrum.* **2019**, *90* (2), 025112. https://doi.org/10.1063/1.5031126.

(88) Richards, J. J.; Hipp, J. B.; Riley, J. K.; Wagner, N. J.; Butler, P. D. Clustering and Percolation in Suspensions of Carbon Black. *Langmuir* **2017**, *33* (43), 12260–12266. https://doi.org/10.1021/acs.langmuir.7b02538.

(89) Hipp, J. B.; Richards, J. J.; Wagner, N. J. Structure-Property Relationships of Sheared Carbon Black Suspensions Determined by Simultaneous Rheological and Neutron Scattering Measurements. *J. Rheol.* **2019**, *63* (3), 423–436. https://doi.org/10.1122/1.5071470.

(90) Brunini, V. E.; Chiang, Y.-M.; Carter, W. C. Modeling the Hydrodynamic and Electrochemical Efficiency of Semi-Solid Flow Batteries. *Electrochimica Acta* **2012**, *69*, 301–307. https://doi.org/10.1016/j.electacta.2012.03.006.

(91) Smith, K. C.; Chiang, Y.-M.; Carter, W. C. Maximizing Energetic Efficiency in Flow Batteries Utilizing Non-Newtonian Fluids. *J. Electrochem. Soc.* **2014**, *161* (4), A486–A496.

(92) Smith, K. C.; Brunini, V. E.; Dong, Y.; Chiang, Y.-M.; Carter, W. C. Electroactive-Zone Extension in Flow-Battery Stacks. *Electrochimica Acta* **2014**, *147*, 460–469. https://doi.org/10.1016/j.electacta.2014.09.108.

(93) Hoyt, N. C.; Savinell, R. F.; Wainright, J. S. Modeling of Flowable Slurry Electrodes with Combined Faradaic and Nonfaradaic Currents. *Chem. Eng. Sci.* **2016**, *144*, 288–297. https://doi.org/10.1016/j.ces.2016.01.048.

(94) Hoyt, N. C.; Agar, E.; Nagelli, E. A.; Savinell, R.; Wainright, J. Editors' Choice—Electrochemical Impedance Spectroscopy of Flowing Electrosorptive Slurry Electrodes. *J. Electrochem. Soc.* **2018**, *165* (10), E439–E444. https://doi.org/10.1149/2.0051810jes.

(95) Weitkamp, J. Zeolites and Catalysis. *Solid State Ion.* **2000**, *131* (1–2), 175–188. https://doi.org/10.1016/S0167-2738(00)00632-9.

(96) Jain, R. K.; Stylianopoulos, T. Delivering Nanomedicine to Solid Tumors. *Nat. Rev. Clin. Oncol.* **2010**, *7*, 653.

(97) Eloul, S.; Compton, R. G. General Model of Hindered Diffusion. *J. Phys. Chem. Lett.* **2016**, *7* (21), 4317–4321. https://doi.org/10.1021/acs.jpclett.6b02275.

(98) Chan, C.; Kätelhön, E.; Compton, R. G. Theoretical Prediction of a Transient Accumulation of Nanoparticles at a Well-Defined Distance from an Electrified Liquid–Solid Interface. *Nanoscale* **2018**, *10* (41), 19459–19468. https://doi.org/10.1039/C8NR05055D.

(99) Bevan, M. A.; Prieve, D. C. Hindered Diffusion of Colloidal Particles Very near to a Wall: Revisited. *J. Chem. Phys.* **2000**, *113* (3), 1228–1236. https://doi.org/10.1063/1.481900.

(100) Lohaus, J.; Rall, D.; Kruse, M.; Steinberger, V.; Wessling, M. On Charge Percolation in Slurry Electrodes Used in Vanadium Redox Flow Batteries. *Electrochem. Commun.* **2019**, *101*, 104–108. https://doi.org/10.1016/j.elecom.2019.02.013.

(101) Golovnev, A.; Suss, M. E. Percolation Probability in a System of Cylindrical Particles. *J. Chem. Phys.* **2018**, *149* (14), 144904. https://doi.org/10.1063/1.5041326.

(102) Hatzell, K. B.; Eller, J.; Morelly, S. L.; Tang, M. H.; Alvarez, N. J.; Gogotsi, Y. Direct Observation of Active Material Interactions in Flowable Electrodes Using X-Ray Tomography. *Faraday Discuss* **2017**. https://doi.org/10.1039/C6FD00243A.

(103) Zhang, Y.; Narayanan, A.; Mugele, F.; Cohen Stuart, M. A.; Duits, M. H. G. Charge Inversion and Colloidal Stability of Carbon Black in Battery Electrolyte Solutions. *Colloids Surf. Physicochem. Eng. Asp.* **2016**, *489*, 461–468. https://doi.org/10.1016/j.colsurfa.2015.08.041.

(104) Gros, C. *Complex and Adaptive Dynamical Systems*; Springer complexity; Springer: Berlin, 2008.

(105) Harris, S. J.; Lu, P. Effects of Inhomogeneities—Nanoscale to Mesoscale—on the Durability of Li-Ion Batteries. *J. Phys. Chem. C* **2013**, *117* (13), 6481–6492. https://doi.org/10.1021/jp311431z.

(106) Dreyer, W.; Jamnik, J.; Guhlke, C.; Huth, R.; Moškon, J.; Gaberšček, M. The Thermodynamic Origin of Hysteresis in Insertion Batteries. *Nat. Mater.* **2010**, *9* (5), 448–453. https://doi.org/10.1038/nmat2730.

(107) Delmas, C.; Maccario, M.; Croguennec, L.; Le Cras, F.; Weill, F. Lithium Deintercalation in LiFePO4 Nanoparticles via a Domino-Cascade Model. *Nat. Mater.* **2008**, *7* (8), 665–671. https://doi.org/10.1038/nmat2230.

(108) Chouchane, M.; Rucci, A.; Lombardo, T.; Ngandjong, A. C.; Franco, A. A. Lithium Ion Battery Electrodes Predicted from Manufacturing Simulations: Assessing the Impact of the Carbon-Binder Spatial Location

on the Electrochemical Performance. *J. Power Sources* **2019**, *444*, 227285. https://doi.org/10.1016/j.jpowsour.2019.227285.

(109) Padding, J. T.; Louis, A. A. Hydrodynamic Interactions and Brownian Forces in Colloidal Suspensions: Coarse-Graining over Time and Length Scales. *Phys. Rev. E* **2006**, *74* (3). https://doi.org/10.1103/PhysRevE.74.031402.

(110) Groot, R. D.; Warren, P. B. Dissipative Particle Dynamics: Bridging the Gap between Atomistic and Mesoscopic Simulation. *J. Chem. Phys.* **1997**, *107* (11), 4423–4435. https://doi.org/10.1063/1.474784.

(111) Espanol, P.; Warren, P. Statistical Mechanics of Dissipative Particle Dynamics. *EPL Europhys. Lett.* **1995**, *30* (4), 191.

(112) Brady, J. F.; Bossis, G. Stokesian Dynamics. *Annu. Rev. Fluid Mech.* **1988**, *20* (1), 111–157. https://doi.org/10.1146/annurev.fl.20.010188.000551.

(113) Ermak, D. L. A Computer Simulation of Charged Particles in Solution. I. Technique and Equilibrium Properties. *J. Chem. Phys.* **1975**, *62* (10), 4189–4196. https://doi.org/10.1063/1.430300.

(114) Malevanets, A.; Kapral, R. Solute Molecular Dynamics in a Mesoscale Solvent. *J. Chem. Phys.* **2000**, *112* (16), 7260–7269. https://doi.org/10.1063/1.481289.

(115) McDowell, M. T.; Lee, S. W.; Nix, W. D.; Cui, Y. 25th Anniversary Article: Understanding the Lithiation of Silicon and Other Alloying Anodes for Lithium-Ion Batteries. *Adv. Mater.* **2013**, *25* (36), 4966–4985. https://doi.org/10.1002/adma.201301795.

(116) Kim, H.; Chou, C.-Y.; Ekerdt, J. G.; Hwang, G. S. Structure and Properties of Li−Si Alloys: A First-Principles Study. *J. Phys. Chem. C* **2011**, *115* (5), 2514–2521. https://doi.org/10.1021/jp1083899.

(117) Flamm, M. H.; Diamond, S. L.; Sinno, T. Lattice Kinetic Monte Carlo Simulations of Convective-Diffusive Systems. *J. Chem. Phys.* **2009**, *130* (9), 094904. https://doi.org/10.1063/1.3078518.

(118) Flamm, M. H.; Sinno, T.; Diamond, S. L. Simulation of Aggregating Particles in Complex Flows by the Lattice Kinetic Monte Carlo Method. *J. Chem. Phys.* **2011**, *134* (3), 034905. https://doi.org/10.1063/1.3521395.

(119) Edward, J. T. Molecular Volumes and the Stokes-Einstein Equation. *J. Chem. Educ.* **1970**, *47* (4), 261.

(120) Dahbi, M.; Ghamouss, F.; Tran-Van, F.; Lemordant, D.; Anouti, M. Comparative Study of EC/DMC LiTFSI and LiPF6 Electrolytes for Electrochemical Storage. *J. Power Sources* **2011**, *196* (22), 9743–9750. https://doi.org/10.1016/j.jpowsour.2011.07.071.

(121) Thomas, D. G. Transport Characteristics of Suspension: VIII. A Note on the Viscosity of Newtonian Suspensions of Uniform Spherical Particles. *J. Colloid Sci.* **1965**, *20* (3), 267–277.

(122) Ulusoy, U.; Yekeler, M.; Hicyilmaz, C. Characterization of Surface Roughness of Calcite by BET and Surtronic 3+ Techniques; 2003.

(123) Pharr, M.; Zhao, K.; Wang, X.; Suo, Z.; Vlassak, J. J. Kinetics of Initial Lithiation of Crystalline Silicon Electrodes of Lithium-Ion Batteries. *Nano Lett.* **2012**, *12* (9), 5039–5047. https://doi.org/10.1021/nl302841y.

(124) Gong, C.; Milberg, O.; Wang, B.; Vicini, P.; Narwal, R.; Roskos, L.; Popel, A. S. A Computational Multiscale Agent-Based Model for Simulating Spatio-Temporal Tumour Immune Response to PD1 and PDL1 Inhibition. *J. R. Soc. Interface* **2017**, *14* (134), 20170320. https://doi.org/10.1098/rsif.2017.0320.

(125) Hinkelmann, F.; Murrugarra, D.; Jarrah, A. S.; Laubenbacher, R. A Mathematical Framework for Agent Based Models of Complex Biological Networks. *Bull. Math. Biol.* **2011**, *73* (7), 1583–1602. https://doi.org/10.1007/s11538-010-9582-8.

(126) Fagiolo, G.; Moneta, A.; Windrum, P. A Critical Guide to Empirical Validation of Agent-Based Models in Economics: Methodologies, Procedures, and Open Problems. *Comput. Econ.* **2007**, *30* (3), 195–226. https://doi.org/10.1007/s10614-007-9104-4.

(127) Laubenbacher, R.; Jarrah, A.; Mortveit, H.; Ravi, S. A Mathematical Formalism for Agent-Based Modeling. Encyclopedia of Complexity and System Science. **2008**.

(128) Allen, M. DJ Tildesley Computer Simulation of Liquids Oxford University Press. *N. Y.* **1987**.

(129) Frenkel, D.; Smit, B. Understanding Molecular Simulation: From Algorithms to Applications. *Comput. Sci. Ser.* **2002**, *1*, 1–638.

(130) Auerbach, S. M. Theory and Simulation of Jump Dynamics, Diffusion and Phase Equilibrium in Nanopores. *Int. Rev. Phys. Chem.* **2000**, *19* (2), 155–198.

(131) Binder, K.; Ceperley, D. M.; Hansen, J.-P.; Kalos, M.; Landau, D.; Levesque, D.; Mueller-Krumbhaar, H.; Stauffer, D.; Weis, J.-J. *Monte Carlo Methods in Statistical Physics*; Springer Science & Business Media, 2012; Vol. 7.

(132) Binder, K. Atomistic Modeling of Materials Properties by Monte Carlo Simulation. *Adv. Mater.* **1992**, *4* (9), 540–547.

(133) Landau, D. P.; Binder, K. *A Guide to Monte Carlo Simulations in Statistical Physics*; Cambridge university press, 2014.

(134) Dooling, D. J.; Broadbelt, L. J. Generic Monte Carlo Tool for Kinetic Modeling. *Ind. Eng. Chem. Res.* **2001**, *40* (2), 522–529.

(135) Gilmer, G. H.; Huang, H.; de la Rubia, T. D.; Dalla Torre, J.; Baumann, F. Lattice Monte Carlo Models of Thin Film Deposition. *Thin Solid Films* **2000**, *365* (2), 189–200.

(136) Nieminen, R.; Jansen, A. Monte Carlo Simulations of Surface Reactions. *Appl. Catal. Gen.* **1997**, *160* (1), 99–123.

(137) Chatterjee, A.; Vlachos, D. G. An Overview of Spatial Microscopic and Accelerated Kinetic Monte Carlo Methods. *J. Comput.-Aided Mater. Des.* **2007**, *14* (2), 253–308. https://doi.org/10.1007/s10820-006-9042-9.

(138) Duke, T.; Le Novere, N.; Bray, D. Conformational Spread in a Ring of Proteins: A Stochastic Approach to Allostery. *J. Mol. Biol.* **2001**, *308* (3), 541–553.

(139) McAdams, H. H.; Arkin, A. Stochastic Mechanisms in Gene Expression. *Proc. Natl. Acad. Sci.* **1997**, *94* (3), 814–819.

(140) McAdams, H. H.; Arkin, A. It'sa Noisy Business! Genetic Regulation at the Nanomolar Scale. *Trends Genet.* **1999**, *15* (2), 65–69.

(141) Woolf, P. J.; Linderman, J. J. Self Organization of Membrane Proteins via Dimerization. *Biophys. Chem.* **2003**, *104* (1), 217–227.

(142) Mayawala, K.; Vlachos, D. G.; Edwards, J. S. Spatial Modeling of Dimerization Reaction Dynamics in the Plasma Membrane: Monte Carlo vs. Continuum Differential Equations. *Biophys. Chem.* **2006**, *121* (3), 194–208.

(143) *Physical Multiscale Modeling and Numerical Simulation of Electrochemical Devices for Energy Conversion and Storage*; Franco, A. A., Doublet, M. L., Bessler, W. G., Eds.; Green Energy and Technology; Springer London: London, 2016. https://doi.org/10.1007/978-1-4471-5677-2.

(144) Blanquer, G.; Yin, Y.; Quiroga, M. A.; Franco, A. A. Modeling Investigation of the Local Electrochemistry in Lithium-O2 Batteries: A Kinetic Monte Carlo Approach. *J. Electrochem. Soc.* **2016**, *163* (3), A329–A337.

(145) Yin, Y.; Zhao, R.; Deng, Y.; Franco, A. A. Compactness of the Lithium Peroxide Thin Film Formed in Li–O 2 Batteries and Its Link to the Charge Transport Mechanism: Insights from Stochastic Simulations. *J. Phys. Chem. Lett.* **2017**, 599–604. https://doi.org/10.1021/acs.jpclett.6b02732.

(146) Yin, Y.; Gaya, C.; Torayev, A.; Thangavel, V.; Franco, A. A. Impact of Li 2 O 2 Particle Size on Li–O 2 Battery Charge Process: Insights from a Multiscale Modeling Perspective. *J. Phys. Chem. Lett.* **2016**, *7* (19), 3897–3902. https://doi.org/10.1021/acs.jpclett.6b01823.

(147) Yin, Y.; Torayev, A.; Gaya, C.; Mammeri, Y.; Franco, A. A. Linking the Performances of Li–O 2 Batteries to Discharge Rate and Electrode and Electrolyte Properties through the Nucleation Mechanism of Li 2 O 2. *J. Phys. Chem. C* **2017**, *121* (36), 19577–19585. https://doi.org/10.1021/acs.jpcc.7b05224.

(148) Liu, Z.; Battaglia, V.; Mukherjee, P. P. Mesoscale Elucidation of the Influence of Mixing Sequence in Electrode Processing. *Langmuir* **2014**, *30* (50), 15102–15113. https://doi.org/10.1021/la5038469.

(149) Thangavel, V.; Xue, K.-H.; Mammeri, Y.; Quiroga, M.; Mastouri, A.; Guéry, C.; Johansson, P.; Morcrette, M.; Franco, A. A. A Microstructurally Resolved Model for Li-S Batteries Assessing the Impact of the Cathode Design on the Discharge Performance. *J. Electrochem. Soc.* **2016**, *163* (13), A2817–A2829. https://doi.org/10.1149/2.0051614jes.

(150) Liu, Z.; Mukherjee, P. P. Microstructure Evolution in Lithium-Ion Battery Electrode Processing. *J. Electrochem. Soc.* **2014**, *161* (8), E3248–E3258. https://doi.org/10.1149/2.026408jes.

(151) Quiroga, M. A.; Malek, K.; Franco, A. A. A Multiparadigm Modeling Investigation of Membrane Chemical Degradation in PEM Fuel Cells. *J. Electrochem. Soc.* **2016**, *163* (2), F59–F70.

(152) Quiroga, M. A.; Franco, A. A. A Multi-Paradigm Computational Model of Materials Electrochemical Reactivity for Energy Conversion and Storage. *J. Electrochem. Soc.* **2015**, *162* (7), E73–E83.

(153) Stukowski, A. Visualization and Analysis of Atomistic Simulation Data with OVITO–the Open Visualization Tool. *Model. Simul. Mater. Sci. Eng.* **2010**, *18* (1), 015012. https://doi.org/10.1088/0965-0393/18/1/015012.

(154) Drews, T. O.; Braatz, R. D.; Alkire, R. C. Parameter Sensitivity Analysis of Monte Carlo Simulations of Copper Electrodeposition with Multiple Additives. *J. Electrochem. Soc.* **2003**, *150* (11), C807. https://doi.org/10.1149/1.1617305.

(155) Medalia, A. I. Electrical Conduction in Carbon Black Composites. *Rubber Chem. Technol.* **1986**, *59* (3), 432–454.

(156) Francos, A.; Elorza, F. J.; Bouraoui, F.; Bidoglio, G.; Galbiati, L. Sensitivity Analysis of Distributed Environmental Simulation Models: Understanding the Model Behaviour in Hydrological Studies at the Catchment Scale. *Reliab. Eng. Syst. Saf.* **2003**, *79* (2), 205–218.

(157) Cooley, W. W. Explanatory Observational Studies. *Educ. Res.* **1978**, *7* (9), 9–15.

(158) Schumacker, R. E.; Lomax, R. G. *A Beginner's Guide to Structural Equation Modeling*, 3rd ed.; Routledge: New York, 2010.

(159) Morris, M. D. Factorial Sampling Plans for Preliminary Computational Experiments. *Technometrics* **1991**, *33* (2), 161. https://doi.org/10.2307/1269043.

(160) Yoo, C.; Oh, S. Combining Structure Equation Model with Bayesian Networks for Predicting with High Accuracy of Recommending Surgery for Better Survival in Benign Prostatic Hyperplasia Patients. 5.

(161) Ariffin, W. N. M.; Salleh, S. The Partitioning Technique of Directed Cyclic Graph for Task Assignment Problem; 2016; p 020010. https://doi.org/10.1063/1.4954523.

(162) Richardson, T. A Discovery Algorithm for Directed Cyclic Graphs. 8.

(163) Li, Z.; Smith, K. C.; Dong, Y.; Baram, N.; Fan, F. Y.; Xie, J.; Limthongkul, P.; Carter, W. C.; Chiang, Y.-M. Aqueous Semi-Solid Flow Cell: Demonstration and Analysis. *Phys. Chem. Chem. Phys.* **2013**, *15* (38), 15833. https://doi.org/10.1039/c3cp53428f.

(164) Hatzell, K. B.; Eller, J.; Morelly, S. L.; Tang, M. H.; Alvarez, N. J.; Gogotsi, Y. Direct Observation of Active Material Interactions in Flowable Electrodes Using X-Ray Tomography. *Faraday Discuss.* **2017**, *199*, 511–524.

(165) Bian, X.; Litvinov, S.; Qian, R.; Ellero, M.; Adams, N. A. Multiscale Modeling of Particle in Suspension with Smoothed Dissipative Particle Dynamics. *Phys. Fluids* **2012**, *24* (1), 012002. https://doi.org/10.1063/1.3676244.

(166) Boek, E. S.; Coveney, P. V.; Lekkerkerker, H. N. W.; van der Schoot, P. Simulating the Rheology of Dense Colloidal Suspensions Using Dissipative Particle Dynamics. *Phys. Rev. E* **1997**, *55* (3), 3124.

(167) Boek, E. S.; Coveney, P. V.; Lekkerkerker, H. N. W. Computer Simulation of Rheological Phenomena in Dense Colloidal Suspensions with Dissipative Particle Dynamics. *J. Phys. Condens. Matter* **1996**, *8* (47), 9509.

(168) Larcher, D.; Courjal, P.; Urbina, R. H.; Gerand, B.; Blyr, A.; Du Pasquier, A.; Tarascon, J. Synthesis of MnO2 Phases from LiMn2 O 4 in Aqueous Acidic Media Mechanisms of Phase Transformations, Reactivity, and Effect of Bi Species. *J. Electrochem. Soc.* **1998**, *145* (10), 3392–3400.

(169) Zheng, H.; Mirsaidov, U. M.; Wang, L.-W.; Matsudaira, P. Electron Beam Manipulation of Nanoparticles. *Nano Lett.* **2012**, *12* (11), 5644–5648. https://doi.org/10.1021/nl302788g.

(170) Zheng, H.; Claridge, S. A.; Minor, A. M.; Alivisatos, A. P.; Dahmen, U. Nanocrystal Diffusion in a Liquid Thin Film Observed by in Situ Transmission Electron Microscopy. *Nano Lett.* **2009**, *9* (6), 2460–2465. https://doi.org/10.1021/nl9012369.

(171) Lu, J.; Aabdin, Z.; Loh, N. D.; Bhattacharya, D.; Mirsaidov, U. Nanoparticle Dynamics in a Nanodroplet. *Nano Lett.* **2014**, *14* (4), 2111–2115. https://doi.org/10.1021/nl500766j.

(172) Chen, Q.; Cho, H.; Manthiram, K.; Yoshida, M.; Ye, X.; Alivisatos, A. P. Interaction Potentials of Anisotropic Nanocrystals from the Trajectory Sampling of Particle Motion Using *in Situ* Liquid Phase Transmission Electron Microscopy. *ACS Cent. Sci.* **2015**, *1* (1), 33–39. https://doi.org/10.1021/acscentsci.5b00001.

(173) Chen, X.; Wen, J. In Situ Wet-Cell TEM Observation of Gold Nanoparticle Motion in an Aqueous Solution. *Nanoscale Res. Lett.* **2012**, *7* (1), 598. https://doi.org/10.1186/1556-276X-7-598.

(174) Lutz, L.; Dachraoui, W.; Demortière, A.; Johnson, L. R.; Bruce, P. G.; Grimaud, A.; Tarascon, J.-M. Operando Monitoring of the Solution-Mediated Discharge and Charge Processes in a Na–O 2 Battery Using Liquid-Electrochemical Transmission Electron Microscopy. *Nano Lett.* **2018**, *18* (2), 1280–1289. https://doi.org/10.1021/acs.nanolett.7b04937.

(175) Grogan, J. M.; Rotkina, L.; Bau, H. H. *In Situ* Liquid-Cell Electron Microscopy of Colloid Aggregation and Growth Dynamics. *Phys. Rev. E* **2011**, *83* (6). https://doi.org/10.1103/PhysRevE.83.061405.

(176) Chen, Q.; Smith, J. M.; Park, J.; Kim, K.; Ho, D.; Rasool, H. I.; Zettl, A.; Alivisatos, A. P. 3D Motion of DNA-Au Nanoconjugates in Graphene Liquid Cell Electron Microscopy. *Nano Lett.* **2013**, *13* (9), 4556–4561. https://doi.org/10.1021/nl402694n.

(177) de Jonge, N.; Ross, F. M. Electron Microscopy of Specimens in Liquid. *Nat. Nanotechnol.* **2011**, *6* (11), 695–704. https://doi.org/10.1038/nnano.2011.161.

(178) Proetto, M. T.; Rush, A. M.; Chien, M.-P.; Abellan Baeza, P.; Patterson, J. P.; Thompson, M. P.; Olson, N. H.; Moore, C. E.; Rheingold, A. L.; Andolina, C.; et al. Dynamics of Soft Nanomaterials Captured by Transmission Electron Microscopy in Liquid Water. *J. Am. Chem. Soc.* **2014**, *136* (4), 1162–1165. https://doi.org/10.1021/ja408513m.

Résumé

Cette thèse est basée sur un dispositif de stockage d'énergie développé récemment, appelé la batterie à circulation de type semi-solide (BCSS), qui représente un croisement technologique entre deux systèmes déjà commercialisés, la batterie lithium-ion et la batterie à circulation. La BCSS possède des particules en suspension comme électrodes qui peuvent être stockées à l'extérieur de la batterie à décharge, dans des réservoirs pour des applications énergétiques à grande échelle. Les défis auxquels sont confrontés les BCSS sont identifiés dans cette thèse. Ils sont attribués au système multi-corps dans lequel se produisent de nombreux phénomènes à différentes échelles, ce qui rend les résultats expérimentaux non intuitifs. Ce travail explore l'applicabilité d'un modèle mécaniste pour gérer ce type de complexité. Un modèle tridimensionnel à base d'agent est développé autour d'un moteur Monte Carlo cinétique. Comme il est difficile de valider ce type de modèle, il est proposé d'utiliser une analyse de sensibilité globale. Il a été démontré que l'utilisation sur de grandes quantités de résultats simulés peut fournir des tendances qui permettent d'identifier les métriques mésoscopiques et émergentes afin de rationaliser la complexité des BCSS. De telles idées ne ressortent ni des expériences ni des modèles traditionnels. Les perspectives et les outils développés ici peuvent fournir un cadre plus rigoureux pour d'autres types de systèmes électrochimiques situés à l'intersection de disciplines.

Mots-clés : Batterie à circulation de type semi-solide, modèle mécaniste, système complexe, modèle à base d'agents, Monte Carlo cinétique, suspension de particules, anode en silicium, modèle discret, analyse de sensibilité des paramètres, python

Abstract

This thesis is based on a recently developed energy storage device called the semi-solid redox flow battery (SSRFB) which represents a technological crossover between two already commercialized systems, namely, lithium ion batteries (LIBs) and redox flow batteries (RFBs). The SSRFB has particle suspensions as electrodes which can be stored outside the discharging battery unit, in tanks, for large scale energy applications. The challenges that plague the SSRFBs are identified in this work. They are assigned to the many-body problem where many phenomena, across scales, compete with one another, leading to a high degree of complexity, which makes experimental results non-intuitive. This work explores the applicability of mechanistic models to handle this type of complexity. The model is an on-lattice, three-dimensional, agent-based model with a kinetic Monte Carlo engine. Since such models are challenging to validate, the use of a global parameter sensitivity analysis (PSA) is proposed. It is demonstrated that using PSA over large amounts of simulated results can provide trends that help identify emergent mesoscopic metrics to rationalize the complexity of SSRFBs; such insights are not apparent from either experiments or traditional models. The perspectives and tools developed herein can provide a more rigorous framework for other types of electrochemical systems that lie at intersections of disciplines.

Key-Words : Semi-solid redox flow battery, mechanistic model, complex system, agent-based model, kinetic Monte Carlo, particle suspension, silicon anode, discrete model, parameter sensitivity analysis, python